UNIVERSITÀ DEGLI STUDI DI MODENA E REGGIO EMILIA

PhD THESIS IN EARTH SYSTEM SCIENCES ENVIROMENT, RESOURCES AND CULTURAL HERITAGE

Department of Chemistry and Geological sciences-GEO-06

-CYCLE XXVI-

CONFINEMENT OF GUEST MOLECULES IN MICROPOROUS MATERIALS

Tutor
Prof. Maria Giovanna Vezzalini
Co-tutor
Dott.ssa Rossella Arletti

PhD student
LARA GIGLI

Director of the school
Prof. Maria Giovanna Vezzalini

Years 2011-2014

Our discoveries come from the chaos.

C. Palahniuk

ABSTRACT

Fascinating dye-zeolite L composites have great relevance in developing technological and biotechnological devices such as light emitting devices (LED) or hybrid solar cells for luminescent solar concentrator and can be used also in molecular imaging. The present doctoral thesis aims to contribute to the advances in structural characterization of dye molecules into zeolite L (ZL). Actually, a detailed structural characterization is necessary to explain the functionality of these materials and their stability and to understand the host-guest interactions involved in their efficiency.

Zeolite L -characterized by a one-dimensional channel system, surrounded by a ring of 12 tetrahedra (12MR), running along the *c* axis - is an ideal host because its structure imposes geometrical constraints to the guest molecules. These structural characteristics lead to a highly ordered and well defined arrangement of the guests inside the channels. In particular, the incorporation of neutral species requires a previous dehydration of the zeolite. For this reason, a detailed structural study of the dehydration process of the zeolite L was carried out through in situ XRPD experiment and Rietveld refinement. It revealed that zeolite L has a very high thermal stability and is essentially inflexible.

Successively, three different dyes were encapsulated into the zeolite L: the neutral dyes Fluorenone and tB-DXP via gas phase adsorption (ZL/FL, ZL/tB-DXP composites) and the cationic thionine via cationic exchange (ZL/Th composites). The characterization of these samples was carried out, at ambient conditions, combining experimental techniques (XRPD and Rietveld refinement, TGA, Infrared spectroscopy, UV/vis and fluorescence spectroscopy) and Molecular Dynamics simulations.

The main results can be summarized as follows: 1) ZL/FL composites. It has been determined that the maximum possible dye loading is 1.5 molecules per unit cell. The distribution of fluorenone molecules within the ZL channel was obtained combining the diffraction data and the Molecular Dynamic simulations results. The stability of the ZL/FL materials was confirmed and attributed to the strong interactions between the oxygen of FL carbonyl group and the ZL extraframework potassium atom. The fluorescence spectroscopy indicated that the optical properties of the composites are not influenced by the amount and organization of FL molecules and by the presence of water molecules in ZL channels. 2) ZL/tB-DXP composites. The comparison between the cell parameters of the zeolite L as synthetized and the composite showed that the encapsulation of a so large dye was successful. Notwithstanding the tB-DXP

molecule length is three times the *c* parameter of ZL, no superstructure evidence was observed in the XRPD pattern. The TGA analysis showed a maximum loading of 0.23 molecule per unit cell and the structural refinement located the dye parallel to the 12MR channel axis. 3) ZL/Th composites. Also in this case the incorporation of thionine entails a slight increase of the unit cell parameters respect to ZL. The XRPD patterns did not show superstructure evidence even if the dye molecule length is two times the *c* parameter of the zeolite. The maximum Th loading is 0.27 molecules per unit cell and the structure refinement allowed the localization of only the thiazine ring.

ZL/tB-DXP and ZL/Th composites showed interesting optical properties and high stability. The work presented here could be helpfully for the development of functional devices with stimulating perspectives in the optical and electronic related fields.

Riassunto

I compositi colorante-zeolite L hanno grande rilevanza nello sviluppo di dispositivi tecnologici e biotecnologici come: light emitting diode (LED), celle solari ibride per concentratori solari luminescenti e anche nell'imaging molecolare. Scopo di questa tesi di dottorato è la caratterizzazione strutturale di materiali ibridi ottenuti dall'incapsulamento di molecole di colorante nella zeolite L (ZL). Un dettagliato studio strutturale è necessario per spiegare la funzionalità e la stabilità di questi compositi, al fine di comprendere a quali interazioni host-guest è dovuta la loro efficienza in quanto il loro utilizzo è di grande rilevanza. ZL, caratterizzata da un sistema di canali monodimensionali delimitati da anelli a 12 tetraedri (12MR) che corrono lungo l'asse c, è un host ideale perché la sua struttura impone forti vincoli alle molecole ospiti che tendono ad organizzarsi in maniera ordinata e ben definita all'interno dei canali. In particolare, il confinamento di molecole neutre richiede una precedente disidratazione della zeolite. Per questo motivo è stato effettuato uno studio strutturale sul processo di disidratazione della zeolite L mediante in situ-XRPD e raffinamento Rietveld. Da questo è emerso che la zeolite L ha un'elevata stabilità termica ed è essenzialmente inflessibile.

Nella ZL sono stati incapsulati tre diversi coloranti: le specie neutre fluorenone e tB-DXP tramite adsorbimento in fase gassosa (ZL/FL, ZL/tB-DXP compositi) e la thionina cationica, mediante scambio cationico (ZL/Th composito). La caratterizzazione di questi campioni è stata effettuata in condizioni ambiente combinando tecniche sperimentali (XRPD e raffinamento Rietveld, TGA, spettroscopia infrarossa, UV/Vis e spettroscopia di fluorescenza) e simulazioni di dinamica molecolare.

I principali risultati possono essere riassunti come segue: 1) ZL/FL. È stato determinato che il massimo caricamento possibile di FL è di 1,5 molecole per cella unitaria. La determinazione della posizione delle molecole di fluorenone all'interno dei canali della ZL è stata ottenuta combinando i dati di diffrazione e i risultati delle simulazioni di dinamica molecolare. La stabilità dei compositi ZL/FL è stata confermata e attribuita alla forte interazione tra l'ossigeno del gruppo carbonilico del FL e il potassio extraframework della ZL. La spettroscopia di fluorescenza ha mostrato inoltre, che le proprietà ottiche dei compositi non sono influenzate né dalla quantità e l'organizzazione delle molecole di FL, né dalla presenza di molecole d'acqua nei canali della ZL. 2) ZL/tB-DXP. Il confronto tra i parametri di cella

della zeolite L e quelli del materiale composito ha mostrato che l'incapsulamento è avvenuto con successo. Nonostante la lunghezza della molecola di tB-DXP sia tre volte il parametro *c* della ZL, nel pattern di diffrazione non è stata osservata la presenza di una superstruttura. L'analisi TGA ha mostrato un carico massimo pari a 0,23 molecole per cella e il raffinamento strutturale ha localizzato il colorante disposto parallelamente all'asse del canale a 12.

3) ZL/Th. Anche in questo caso l'incorporazione di thionina comporta un leggero aumento dei parametri di cella rispetto a quelli della ZL tal quale. Il pattern XRPD non ha evidenziato la presenza di una superstruttura, anche se la lunghezza di Th è due volte il parametro *c* della zeolite. Il massimo di Th caricato è pari a 0,27 molecole per cella unitaria e il raffinamento strutturale ha permesso di localizzare solo l'anello thiazinico.

I campioni ZL/tB-DXP e ZL/Th hanno mostrato interessanti proprietà ottiche ed elevata stabilità. Si ritiene che il presente lavoro possa essere utile per lo sviluppo di nuovi devices con ambiziose prospettive nel campo della fotochimica e dell'elettronica.

INDEX pages

CHAPTER 1 - GENERALITES OF ZEOLITES

1.1. Introduction 1
1.2. Crystal-chemistry of zeolites 4
1.3. Genesis of zeolites 6
1.4. Synthesis of zeolites 6
1.5. Properties of zeolites 7
1.6. Applications of natural and synthetic zeolites 10
References 13

CHAPTER 2 - NEW APPLICATION FIELDS OF ZEOLITES

2.1. Use of zeolites in advanced technological and biological fields 14
2.2. Mimicking the green plants- artificial antenna systems 18
2.3. Supramolecular organization of organic dyes inside the zeolite l channels 20
2.4. Insertion of the dye into zeolite L 25
References 28

CHAPTER 3 – ZEOLITE THERMAL BEHAVIOUR

3.1. Thermal behavior of zeolites 31
3.2. Classification of zeolites based on their thermal behavior 31
3.3. Structural changes induced by thermal treatment 33
3.4. Factors governing the thermal behavior of zeolites 33
References 34

AIMS OF THE THESIS 35

CHAPTER 4 – MATERIALS AND METHODS

4.1. Materials 38

4.1.1. Zeolite L structural and chemical features 38

4.1.2. Guest species-dyes 46

4.2. Methods 57

4.2.1. X-Ray powder diffraction 57

4.2.2. Thermal analysis/TGA-MS EGA 58

4.2.3. ATR-IR Spectroscopy 58

4.2.4. Transmission FT-IR 58

4.2.5. Computational methods 59

4.2.6. Optical spectroscopy: UV/Vis and fluorescence 60

References 62

CHAPTER 5 - THERMAL BEHAVIOUR OF ZEOLITE L

5.1. Structural refinement 63

5.2. Results 65

5.2.1. Framework 66

5.2.2. Extraframework sites 69

5.2.3. Re-hydration process 72

5.3. Discussion and conclusions 73

APPENDIX A 76

References 80

CHAPTER 6 – HYBRID MATERIALS

6.1. ZL/FL composites 81

6.1.1. Synthesis of ZL/FL composites 81

6.1.2. TGA- MSEGA 81

6.1.3. ATR-IR analysis 84

6.1.4. Transmission FT-IR 85

6.1.5. Structure refinement 86
6.1.6. Models and calculations 92
6.1.7. Optical spectroscopy 98
6.1.8. Conclusions 100
APPENDIX B 101

6.2. ZL/tB-DXP composites 106
6.2.1. Synthesis of ZL/tB-DXP composites 106
6.2.2. TGA-MSEGA 106
6.2.3. Transmission FT-IR 108
6.2.4. ATR-IR analysis 109
6.2.5. Structure refinement 111
6.2.6. Optical spectroscopy 116
6.2.7. Conclusions 118
APPENDIX C 119

6.3. ZL/Th composites 123
6.3.1. Synthesis of ZL/Th composites 123
6.3.2. TGA-MSEGA 123
6.3.3. ATR-IR analysis 125
6.3.4. Structure refinement 126
6.3.5. Optical properties 131
6.3.6. Conclusions 132
APPENDIX D 133
References 137

CONCLUSIONS 139

APPENDIX I I

APPENDIX II VI

APPENDIX III XIII

APPENDIX IV XVII

APPENDIX V XIX

APPENDIX VI XXII

1. GENERALITIES OF ZEOLITES

1.1. Introduction

The discovery of natural zeolites dates back to 1756. Their discovery is attributed to A.F. Cronsted [1], who observed that these minerals, when heated, release vapour, and coined the term “zeolite” (from the Greek words zeo= to boil and lithos= rock; that is, boiling stones). Zeolite species are more than 170: a third are natural compounds, while the others are obtained in laboratories by synthesis processes. Many articles, reviews and books describe the structure of these fascinating mineral [2-6]. A wider definition, which does not put constrains on the framework chemical composition and includes interrupted frameworks was given by IMA CNMMN (International Mineralogical Association, Commission on New Minerals and Mineral Names [7]. According to this definition “*Zeolite mineral is a crystalline substance with a structure characterized by a framework of linked tetrahedra, each consisting of four O atoms surrounding a cation. This framework contains open cavities in the form of channels and cages. These are usually occupied by H_2O molecules and extra-framework cations that are commonly exchangeable. The channels are large enough to allow the passage of guest species. In the hydrated phases, dehydration occurs at temperatures mostly below about 400°C and is largely reversible.The framework may be interrupted by (OH,F) groups; these occupy a tetrahedron apex that is not shared with adjacent tetrahedra* ". This definition allows, therefore, to consider zeolites as compounds both natural and synthetic characterized by anionic three-dimensional scaffold, called framework, which has as primary building unit the tetrahedron TO_4 (Primary Building Unit, PBU). The PBUs are connected to each other by sharing the vertices (oxygen atoms (O)). Anyway, as foreseen by the definition of CNMMN, O atoms can also not be shared. These oxygen atoms can be saturated by H^+ ions, thus forming OH^- groups, or are replaced by F^-, as occurs for example in roggianite, maricopaite and partheite.

Depending on how the tetrahedra are organized in the space to form the framework, they give rise to different structural types, called framework type. A code of three capital letters (e.g., MOR, LTL, FAU, MFI, etc ...) is assigned to each structure type. The framework type does not take into account the chemical composition or the presence of structural defects, but describes simply the way in which the tetrahedra TO_4 are connected to each other in the highest possible symmetry (topological symmetry). All

framework type currently recognized are listed in "'ATLAS OF ZEOLITE STRUCTURE TYPES " [8] available at the website: www.iza-structure.org/databases. Each framework type can be described through the SBU (Secondary Building Units), consisting of a variable number of PBU, periodically repeated in the space from which the framework in question is obtained (Fig. 1.1.1).

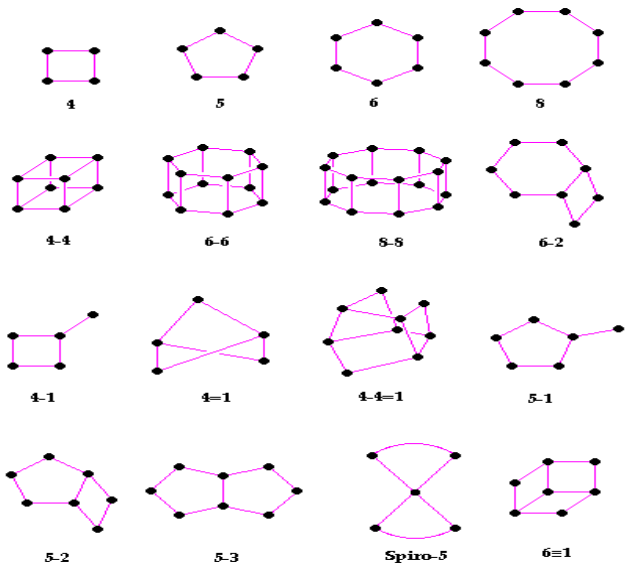

Figure 1.1.1. Secondary Building Unit, [9]

Zeolite framework is characterized by the presence of large cavities interconnected, that can be ideally infinite (channel) (Fig. 1.1.2 a) or closed (cage) (Fig. 1.1.2 b) with openings of less than 2 nm. For this reason zeolites are defined microporous materials.

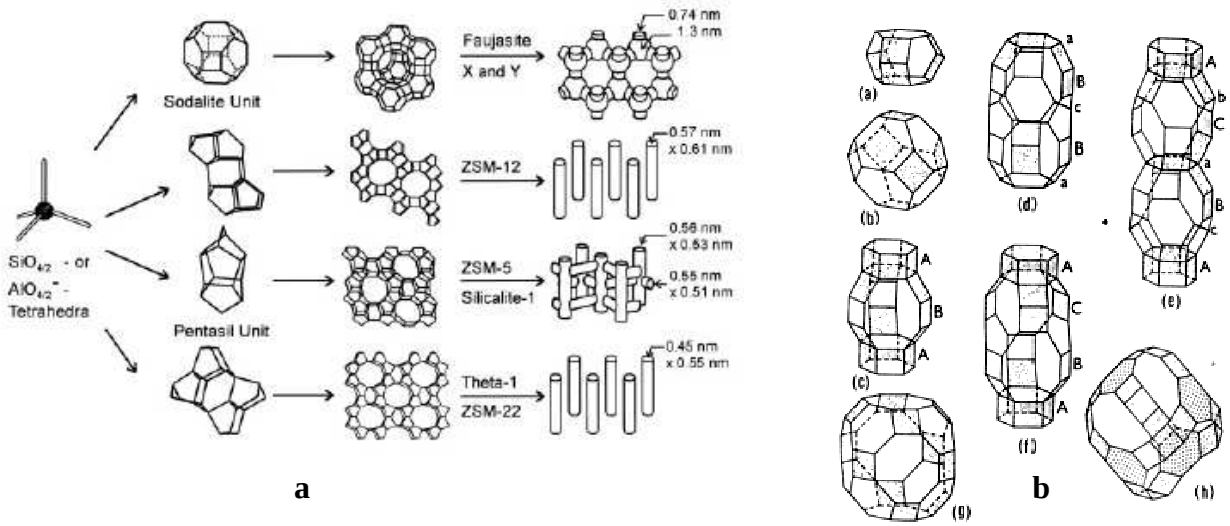

Figure 1.1.2. a) Dimensions of micropore system of four selected zeolites: faujasite or zeolite X and Y, ZSM-12, ZSM-5 or silicalite-1; theta-1 or ZSM-22[10]; b) Examples of zeolite cages.

The zeolite structures can be classified on the basis of their channel systems: 1-dimensional (1D), 2-dimensional (2D) or 3-dimensional (3D), depending if they develop in one direction, on a plane or in the three spatial directions. In a 3D system the adsorbed species can diffuse in all directions, in the 2D-dimensional one the diffusion is limited on a plane, while in the 1D-dimensional systems in only one direction.

The dimensions of the channels are defined by the *free internal diameter*, that is the diameter of the rings of TO_4 tetrahedra forming the 'walls' of the channels. Depending on the size of the channels, zeolites can be distinguished in small, medium, large and extra-large pores (Table 1.1.1):

Table 1.1.1. Zeolite classification based on the size of the channels and defined by the number of tetrahedra [6].

Zeolites	Tetrahedra number	Free diameter (nm)	examples
Small pores	8	0,35 - 0,45	A, natrolite, phillipsite
Medium pores	10	0,45 - 0,60	ZSM-5, ferrierite,
Large pores	12	0,6 - 0,8	X, Y, mordenite, faujasite, zeolite L
Extra-large pores	14	0, 7 - 1,0	UTD-1

Cations, as Ca, Mg, Sr, Ba, Fe^{2+}, Mn, Li, Na, K, etc. - consistent with their charge and radius- water molecules and more complex molecular species as organic molecules can be sited inside the structural voids. These species (extraframework species) can be easily removed through exchange processes or dehydration. We can define the framework as host and extraframework species as guests.

1.2. CRYSTAL-CHEMISTRY OF ZEOLITES

Zeolite general formula, based on Smith's definition [11], can be written as:

$$M_x D_y [T_{(x+2y)}Si_{(z-(x+2y))}O_{2z}] nH_2O$$

With:

framework composition inside the parenthesis

M= monovalent cations (Na, K, Li)

D= divalent cations such as Mg, Ca, Sr, Ba (Fe, Mn)

T= tetracoordinated cations

and

$$0 \leq x \leq 0.5\ z$$

$$0 \leq y \leq 0.25\ z$$

$$0 \leq x+2y \leq 0.5\ z$$

$$0.3\ z \leq n \leq 1.2\ z$$

According to the CNMMN (natural or synthetic) definition, the general formula for zeolites can be written as follow:

$$M_x N_y [T'_p T''_q \ldots O_{2(p+q+\ldots)-\varepsilon} (OH)_{2\varepsilon}] \cdot nQ$$

With:

M= alkali cations more or less exchangeable (Na, K, Li)

N= non-metallic ions or organic molecules

T= tetrahedric coordinated cations

Q= adsorbed molecules (not only water)

Many authors, however, tend to prefer the other, more restrictive definition.

The variations in chemical composition of zeolites depend on the type, charge and dimension of extraframework cations and on the Si/Al ratio.

The Si/Al ratio is a very important factor among those determining the physical properties of zeolites, because influences the charge localization and, therefore, the localization of extraframework cations or of possible acid sites. On the basis of the Lowenstein rule, this ratio has a lower limit of 1 since it is unlikely that an AlO_4 tetrahedron could be bonded to another AlO_4 tetrahedron by sharing their oxygen atoms. The Si/Al ratio can vary from 1 (eg. gismondina) to 7.6 (mutinaite) in natural zeolites and from 1 to infinitive in the synthetic phases.The extraframework cations balance the negative charge due to Si/Al substitutions. They can be bonded to framework oxygens or to water molecules. In the latter case, water molecules build up a “moisturizing sphere” around the extraframework cations, pointing their negative dipole towards the cation. It is important to note that the number of water molecules inside the channels depends on the crystallization conditions and by the nature of bonded cations, for example divalent cations tend to have a bigger moisturizing sphere than monovalent ones.

1.3. GENESIS OF ZEOLITES

Natural zeolites may have hydrothermal or sedimentary genesis.

a) Hydrothermal. Crystals are formed in cavities and fractures of igneous rocks (mostly basalts, but also plutonic and metamorphic rocks), which are deposited by the precipitation of hot aqueous solutions of magmatic origin. The interaction between the magmatic fluid and the rocks in decreasing pressure allows the crystals nucleation inside the cavities. This results in macroscopic size crystals in the hosting rock. The Si/Al ratio is affected by the chemical composition of the percolating fluid.

b) Sedimentary. The zeolites are formed from sedimentary piroclastites coming in contact with aqueous solutions (meteoric water or ground water, in conditions of low pressure and low temperature) and dissolving the glassy component. This leads to the precipitation of a large quantities of submicroscopic zeolite crystals [12]. When the content of zeolites exceed 50% these rocks are called zeolitites.

1.4. SYNTHESIS OF ZEOLITES

Barrer was the first to synthetize zeolites in 1938. Initially the interest for this study was quite scarce, because of the difficulties in obtaining pure crystalline phases. Then, during the 50s, when easier synthesis conditions were discovered, the interest increased and a great number of zeolites was synthesized.

Further progress occurred when the possibility of using organic molecules, called templates, was discovered: thanks to this method the synthesis of Si-rich zeolites was made possible.

In a typical synthesis a source of silica, alumina, organic templating agent and a base are mixed with distilled water. The synthesis experiments are conducted at alkaline pH in autoclaves at a suitable temperature (generally in mild hydrothermal condition) in a oven and for a period of time necessary to obtain the desired product. Then the autoclaves are removed from the oven and cooled rapidly below 50 ° C to prevent the recrystallization of more stable phases.

Two mechanisms can lead to the formation of crystalline germs:

1) the solution transport, the reagents are in solution and the diffusion of ions in the liquid is therefore favored especially if the solution is brought up to temperature. The crystalline germs appear within the liquid phase, by condensation reactions, growing for steps or in spiral form. A solid phase (amorphous gel) can also be

present which, dissolving itself continuously, provides the reagents to the solution. The dissolved species then reach the crystallization nuclei in the solution.

2) transformation into the solid phase mechanism, where the crystallization occurs directly from amorphous gel without the addition of a liquid phase. The reaction starts from the reactants in the solid state (oxides) which, placed in contact between them and increasing the temperature, give rise to an amorphous phase (amorphous gel) from which the first crystalline germs are formed.

   Therefore the system proceeds from an initial disordered state (mixing step reagents used in the synthesis), with a very high entropy through a state with a microscopic order (nuclei formation), reaching the final state, with a macroscopic order (crystal formation).

The formation of zeolites takes place following one of these two mechanisms, or both of them. Depending on which zeolite is desired other post-synthesis treatments can be applied. For example, in order to obtain catalytically active zeolites, cations must be removed from channel and exchanged with ammonium ion (NH_4). Then, after the calcination and the consequent release of NH_3, a H^+-zeolite is obtained

1.5. PROPERTIES OF ZEOLITES

The characteristic properties of zeolitic materials are related to the presence of cavities (cages and channels) and negative charges on the framework due to the substitution of Si^{4+} by Al^{3+} in tetrahedral sites. These charges are localized in specific sites that may be inside the cages or on the walls of the channels [13]. The most exploited zeolites properties are:

1. High adsorption capacity;
2. Molecular sieving;
3. High cation exchange;
4. Reversible dehydration;
5. Catalytic properties.

1) High adsorption capacity. The word “to adsorb” means the ability of a material to accommodate gas or liquid molecules on its surface. In the case of zeolites, even the walls of cavities act as the external surfaces. Adsorbed molecules are captured by superficial charges not bonded. The adsorption ability of a zeolite depends by its Si/Al ratio, in fact, a higher Si/Al value implies a lower surface charge density and leads to

lower adsorption capacity and, in general, to more hydrophobic behavior of the zeolite. On the contrary a low Si/Al ratio, leads to a high residual charge density, to an excellent adsorption ability and to a hydrophilic character of the zeolite.

2) Molecular sieving. Dehydrated zeolites have in general empty channels, so can adsorb various molecules (not only water). In this way zeolites can be used to purify or segregate molecules from a solution or from a gas. The selective capacity of zeolites is not only affected by their Si/Al ratio, but also by the dimension of pores and channels. In this way zeolites can act as “molecular sieves” for a mixture of two components, different in shape and dimension, which are in transit through zeolite channels. According to [14] the minimum diameter required to allow the transit of molecules is that of a ring of six tetrahedra.

3) High cation exchange. Cation exchange is the reversible interchange of two cations between two compounds. The exchanger should be not soluble in the material in which this exchange takes place. Schematically the reaction can be represented as follow:

$$\mathbf{M^- A^+ + B^+ = M^- B^+ + A^+}$$

If the exchanged zeolite is monocationic, in a brief time it will be completely exchanged. If the solution instead is polycationic, the zeolite will exchange only those cations with low solvation energies such as K, NH_4, Cs, Pb e Sr. The exchange property is affected also by the Si/Al ratio.

4) Reversible dehydration. At ambient conditions (T, P and humidity), the zeolites (framework, exchangeable cations and water molecules) are in equilibrium with the external environment. If the environmental conditions change (increase of temperature or decompression), the zeolites will tend to release the water molecules and to achieve new equilibrium conditions. A dehydrated zeolite, reported in environmental conditions, will therefore be "metastable", tending to reversibly absorb water from ambient humidity.

5) Catalytic properties. Zeolites are also used as catalysts for the presence of catalytic sites (acid sites), active within their channels to which molecules reagents with determined shape and size can easily access.

These sites are:

- *Brönsted acid sites* (Fig. 1.5.1), due to the presence of a structural hydroxyl: a proton H^+ binds an oxygen of the framework to balance the charge after replacing Si with Al;
- *Lewis acid site* (Fig. 1.5.1*)*, due to the presence of tricoordinate Al atom that carries an excess of charge.

In the first case, a structural hydroxyl, placed in correspondence of a bridge Si - O - Al would transfer its proton during reactions involving organic molecules; in the second case, the excess of charge is able to polarize (and deform) the molecules and their bonds, allowing the adsorption also of electrically neutral or non-polarizing species.

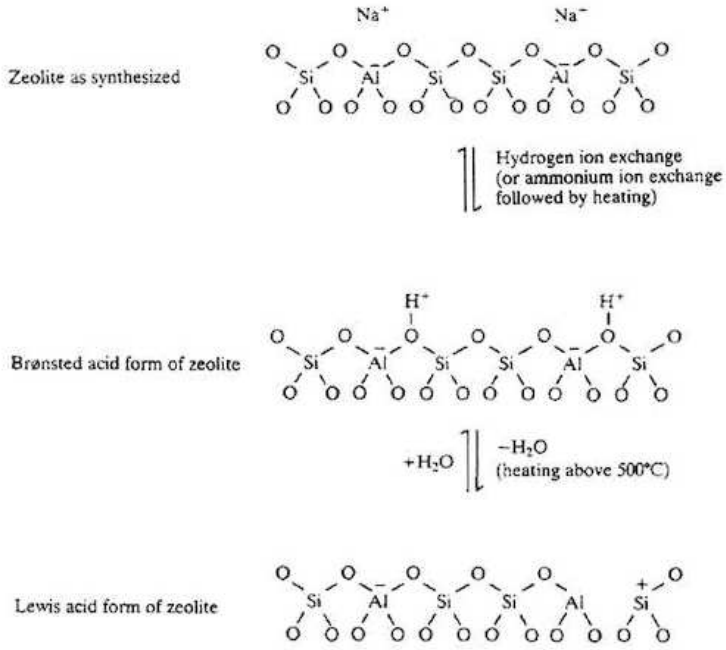

Figure 1.5.1. Schemes for generation of Brønsted and Lewis acid sites in zeolites

To obtain catalytically active zeolites it is necessary to exchange the zeolite with ammonium ion NH_4^+ and then to calcine it at about 550°C for some hours. In this way it is possible to remove NH_3 and leave only protons inside the structure.

The catalytic active zeolites are mostly used in the process of cracking of hydrocarbons [15], which consists in converting high molecular weight hydrocarbons in lighter alkanes and alkenes.

1.6. APPLICATIONS OF NATURAL AND SYNTHETIC ZEOLITES

Zeolites, as a consequence of their properties, can be used for a great number of industrial processes and many new applications have been discovered thanks to continuous studies in this field (Table 1.6.1).

It is possible make an initial distinction between the applications of the natural [16] and the synthetic zeolites. The first have a massive use, related to their ion exchange capacity, which make them suitable, such as those containing Na^+, as additives to sweeten the waters since Na^+ ions can be released and replaced by Ca^{2+} ions from hard water. Zeolites can be regenerated by passing it in a very pure saline solution of NaCl. Currently, the Na^+ zeolites are added to washing machine detergents instead of polyphosphates.

Some zeolites have affinity for a cation in particular. It is the case of clinoptilolite, a natural zeolite that is easily exchanged with Cs ions. It can then be used to separate the ^{137}Cs, from radioactive waste, exchanging Na^+ ions with Cs^+ ions.

Natural zeolites are also used as dehydrating agents, since, once dehydrated, they can host in their cavities water molecules coordinated to the cations. For this type of application the zeolites have to be previously dehydrated by heating under vacuum, becoming good drying agents and are used in packing of a multitude of items (tennis shoes, electronic devices, etc.). Moreover, dehydrated zeolites, are also able to adsorb large quantities of various substances and can be used as molecular sieves to purify or separate different molecules. For example, the chabazite zeolite is well known to adsorb small molecules such as formic acid, methanol and SO_2 from polluted emissions in industrial furnaces.

Natural zeolites are mainly used as purifiers for polluting solutions and as amendants for soils. The latter case foresees the temporary capture of NH_4 and K ions that will be slowly released after an exchange with the Na and Ca present in the soil. This process allows a more extensive use and a lesser extent of loosening and leaching and a P transfer and solubilisation of insoluble phosphate phases.

Moreover it is possible capture polluting (Cu, Pb, Zn) and radiogenic (Cs, Sr) metals and therefore a decrease of their assimilation by the soil.

Table 1.6.1. Application fields of natural and synthetic zeolites

	Characteristics	**Application fields**
Natural Zeolites (sedimentary)	· Limited availability · Limited number of structural types · Limited level of purity · Less expensive	Zootechnical, air and water treatment and purification, agriculture, construction
Synthetic Zeolites	· Unlimited availability · Large number of structural types · High level of purity · More expensive	Petrochemical industry and Detergent, removal of CO_2 from natural gas and hydrocarbons from the air.

The high absorption capacity of zeolites makes them unique materials to be used as catalyst, due to their high surface area and the simultaneous presence of acid sites. The amount of absorbed molecules depends from:

- the total surface and the residual charge density of the zeolite;
- the volume, configuration and polarity of the guest molecules;
- state of unsaturation if the adsorbed molecules are organic

Using synthetic zeolites as catalysts it is possible to treat 100 times the amount of molecules which would be treatable with other catalysts. Furthermore, thanks to their ability to act as molecular sieves and their good thermal stability and purity, synthetic zeolites are mostly used in the process of "cracking" of hydrocarbons. Table 1.6.2 provides a brief review of how and where synthetic zeolites are actually used in industry.

Table 1.6.2. Industrial applications of synthetic zeolites (http://www.eltrex.pl)[17]

Application	Role of zeolite molecular sieves
Air dryers	• Dehydration of plastic pellets before they are molded • Dehydration for instrument air • Dehydration of room air with molecular sieve impregnated dessicant wheels
Oxygen concentrators for respiratory patients	• Adsorption of nitrogen from compressed air using a pressure or vacuum swing system to obtain oxygen purity up to 95%
Air brakes	• Dehydration of compressed air on brake systems of heavy- and medium-duty trucks, buses and trains • Pressure swing dryers are used to reduce the dew point of air in the brake reservoir below ambient temperature to prevent freeze-up and corrosion
Insulated glass (dual-pane windows)	• Removal of initial trapped moisture inside the dual-pane window and the moisture that will permeate during the life of the unit to prevent fogging • Removal of vapors from organic sealing materials, paint and cleaning solvents introduced during window manufacture
Polymer formulations	• Dehydration of moisture-sensitive formulations — added to poly coatings, epoxies and urethanes to control the curing process and coatings, adhesives, sealants, elastomers, metal-rich paints and vinyl foams to eliminate unwanted water reactions
Radioactive cleanup	• Removal of radioactive nucleotides by ion exchange — cesium and strontium are exchanged preferentially into the zeolite molecular sieves to greatly reduce the volume of liquid waste
Refrigeration and air-conditioning (A/C) systems	• Dehydration of automotive A/C, transport refrigeration, home refrigerators, freezers, residential A/C, heat pumps and commercial refrigerants to prevent freeze-up and corrosion • Dehydration to protect system materials from adverse chemical reactions
Deodorization	• Removal of odor or taste from personal-care products and plastics with high silica (hydrophobic) zeolite molecular sieves. Odors are adsorbed, not masked
Package dehydration	• Dehydration with zeolite molecular sieves when very low humidity conditions are required. Small desiccant packets or tablets protect products such as pharmaceuticals, medical diagnostic reagent kits, vitamins, food, candy, batteries, dry fuel propellants, machine parts, film and instruments
Air separation	• Removal of water and carbon dioxide from air before liquefaction and cryogenic separation of nitrogen, oxygen and other atmospheric gases • Separation of oxygen and nitrogen with pressure swing or vacuum swing adsorption systems
Natural gas	• Dehydration before cryogenic recovery of hydrocarbon products and helium • Dehydration of high acid gas content (CO_2 and H_2S) natural gas and natural gas condensate streams • Removal of sulfur compounds from ethane, propane and butane • Removal of water and CO_2 before methane liquefaction • Removal of water and sulfur compounds to protect gas transmission pipelines • Dehydration of natural gas liquids • Desulfurization of feed streams for ammonia and other chemical plants • Removal of mercury, preventing damage to aluminum heat exchangers
Petroleum refining	• Dehydration of alkylation feed, refinery gas streams prior to cryogenic separation, naphtha and diesel oil • Purification of feedstocks to protect isomerization catalysts • Removal of water, HCl and H_2S from reformer streams • Removal of oxygenates from etherification raffinate streams and alkylation feed • Removal of nitriles from etherification feed • Dehydration of ethanol • Dehydration and desulfurization of LPG streams • Separation of normal paraffins from branched chain and cyclic compounds • Purification by pressure swing adsorption for upgrading hydrocarbon streams
Petrochemicals	• Dehydration and purification of NGL/ethane/propane feed • Dehydration of cracked gas, C_2 and C_3 splitter feed and hydrogen • Dehydration and purification of salt-dome-stored ethylene, propylene and various other feedstocks • Removal of water, carbon dioxide, methyl alchohol and other oxygenates, hydrogen sulfide and sulfur compounds, ammonia and mercury from ethylene, propylene, butylenes, amylenes and various solvents and co-monomers
Volatile organic compound removal	• Removal of trace volatile organic compounds from air streams • Removal of volatile organic compounds from moisture-laden process streams

References

[1] Cronsted A.F. Akad. Handl. (Stockolm) (1756) 18, 120

[2] Wright P.A and Pearce G.M. (2010), Zeolites and Catalysis: Synthesis, Reactions and Applications, Cejka J., Corma A. Zones S.(Editors) Wiley VGH, 171-204

[3] McCusker L. B. and Baerlocher Ch. (2007) Introduction to Zeolite sciences and Practice 3rd edn Studies in Surface and Catalysis, Vol 168 Cejka,J., H. van Bekkum, A. Corma, F. Schueth (Editors) Elsevier, 13-37

[4] Lobo. R.F. (2004) Handbook of Zeolite Science and Technology, S. Auerbach, K. Carrado, P. Dutta (Editors) Marcel Dekker, New York

[5] Wright P.A. (2007) Microporous Framework Solids, RSC Publishing, Cambirdge
(2001) Zeolites and Molecular Sieves: an Historical Perspective Studies in Surface and Catalysis 137 H. van Bekkum, E.M. Flanigen, P.A. Jacobs and J.C. Jansen (Editors) Elservier sciences

[6] Coombs D.S., Alberti A., Armbruster T., Artioli G., Colella C., Galli E., Grice J.D., Liebau F., Mandarino J.A., Minato H., Nickel E.H., Passaglia E., Peacor D.R., Quartieri S., Rinaldi R., Ross M., Sheppard R.A., Tillmanns E., Vezzalini G., Canadian Mineralogist, 35 (1997) 1571

[7] Baerlocher Ch., Meier W. M ., Olson D. H. (2007), Atlas of zeolite structure types, 6th revised edition, Elsevier, London

[8] Meier W.M., Olson D.H., Baerlocher Ch. (1996) “Atlas of zeolite structure types Zeolites” Volume17 1-2 1-229

[9] J. Weitkamp, (2000) *Solid State Ionics* 131 175-188

[10] J.V. Smith, (1984), *Zeolites* Vol 4, 309

[11] Hay, R.L. (1978), Sand L.B., Mumpton F.A. (Editors.), Pergamon Press, Elmsford, New York, p. 135

[12] Sherman J.D., (1999) Proc. Natl. Acad. Sci. USA vol.96, 3471-3478

[13] R.M. Barrer, (1958) *Jour. Chem. Soc*. London, 99

[14] Maxwell, I.E., Stork, W.H.J. (2001), Studies in Surface Science and Catalysis, 137, H. van Bekkum, E.M. Flanigen, P.A. Jacobs and J.C. Jansen (Editors) Elservier sciences, 747

[15] Armbruster T. and Gunter M. E. (2001) Crystal structure of natural zeolites reviews in mineralogy and geochemistry, 45, 1-67.

[16] http://www.eltrex.pl

2. NEW APPLICATION FIELDS OF ZEOLITES

2.1. Use of zeolites in advanced technological and biological fields

A new possible application of zeolites which has attracted increasing attention in recent, years, is that in photochemistry. In fact, the property of zeolites to host a great variety of organic molecules in their voids, especially dye molecules, has considerable interest in the preparation for optical and biological application. In particular, organization of dye molecules in zeolite channels has been successfully carried out using one dimensional channel systems zeolite (examples are $ALPO_4$-5, zeolite L). In such systems, called artificial antenna systems, electronic excitation energy is efficiently transported along the channels by Forster resonance energy transfer (FRET) (Figure. 2.1.1 A).

The theory at the base of FRET process is reported in Appendix I.

The interplay of confinement and stability of the guest (protected by the zeolite framework) designs a potential use of the dye-zeolite composites in quantum solar energy conversion devices i.e. dye sensitized solar cells, luminescent solar concentrators or color changing media. The employment of the stopcock molecules (see next chapter) located at the interface between the interior of a zeolite crystal and the surrounding environment, allows the communication between dye molecules inside the nanochannels and objects outside the crystals. Fluorescent stopcocks can be used to extract or inject electronic excitation energy into or from the zeolite crystals. In Fig. 2.1.1 two strategies that can be followed are shown: B refers to thin layer silicon cells and C to organic solar cells where the design must match the short free path lengths of the charge carriers in such devices [1-3].

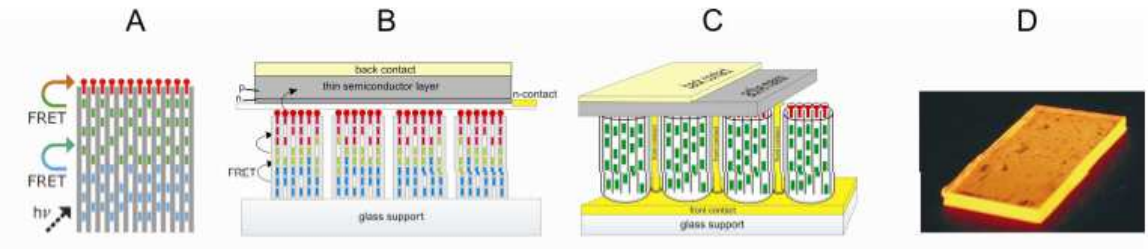

Figure 2.1.1. New building blocks for solar energy conversion devices. A: principle of these new building blocks, consisting of nanochannels containing two types of dye molecules (blue and green) and stopcocks (red). Light absorbed by the blue and green molecules travels to the stopcock heads radiationless by near field interaction (FRET). B and C: principle of dye sensitized solar cells. Arranging crystals, of a length of 50 nm up to a few hundred nm, with their c axes perpendicular to the surface of a semiconductor allows the transport of the excitation energy towards the zeolite-semiconductor interface by FRET. Stopcock molecules are placed only at one channel end. The semiconductor layer can be very thin, because the electron-hole pairs form near the surface. The transfer of electrons from the antenna to the semiconductor is prevented by introducing a thin insulating layer, preferably directly into the stopcock. Scheme B shows a principle related e.g. to thin layer silicon devices. Scheme C is related to organic or plastic solar cells. The white area on top of the head is an insulating level directly integrated into the stopcock. The zeolite material is enlarged with respect to the rest of the device. D: Small fluorescent concentrator (2cm x 1cm) with the dye DXP as donor and the dye ATTO 565 as acceptor which acts as emitter dye [4].

Energy can also be transferred from an appropriately chosen semiconductor to the antenna composites by reversing the current and putting a voltage over the semiconductor. The dye-zeolite composites on the semiconductor surface subsequently lose their energy by emitting light. The color of the emission can be tuned by adapting the ratio of blue, yellow, and red fluorescent dyes, which means that white light emission is possible. High energy efficiency and easily adaptable emission spectra are expected for (O)LEDs made by using this principle. [1,5].

A luminescent solar concentrator (LSC) (Figure. 2.1.2.) is a transparent plate containing luminescent chromophores [6]. Light enters the face of the plate and is absorbed and reemitted by these centers.

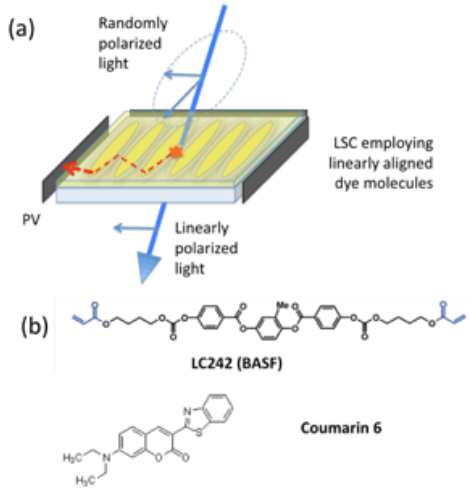

Figure 2.1.2. (a) Schematic representation of linearly polarized luminescent solar concentrators (LSC) for energy-harvesting. (b) Chemical structures of the materials used for the linearly polarized LSC studies (http://mtlsites.mit.edu/energy/agenda/poster-mulder) [7].

A fraction of the luminescent light is trapped by total internal reflection and guided to the edges of the plate where it can be converted to electricity by a photovoltaic device. As the edge area of the plate is much smaller than the face area, the LSC operates as a concentrator of light. Many disadvantages kept the LCS from being widely used: limited stability of the luminescent organic species, high self-absorption and poor understanding of the parameters governing device efficiency [8].

A solution for this problem is the use of antenna material as explained in Figure 2.1.1. Absorption and emission spectra are separated by employing an absorbing dye present in large amount and a monolayer of an emitting dye [9-11]. Figure 2.1.1 D shows an experiment where the dyes DXP and ATTO 565 were used as absorbing dye and as emitter respectively.

Thanks to their properties and biocompatibility these dye-zeolite composites can also be used in biological field as therapeutic, sensing, and imaging agents to target, label and photo inactivate pathogenic and antibiotic resistant bacteria [12]. Phototherapeutic agents constitute a powerful armory for treating cancers and infectious diseases [13-15].

Recent challenges of modern pharmacology include resistance of bacteria to multiple antibiotics and of neoplastic cells to chemotherapeutics, which on the other hand cause undesired side effects. Photodynamic therapy (PDT) is an established cancer and macular degeneration treatment [14-15] and constitutes an alternative against antibiotic-resistant bacteria [15] In PDT (see Figure. 2.1.3.) a photosensitizer generates cytotoxic $^1O_2$ upon

irradiation with light. The ultimate goal is to develop one single structure possessing targeted therapeutic agents, efficient $^1O_2$ photoproduction, and imaging capacities [13-15]. Recently it has been also reported, that pyronine-dye amino-modified zeolite L microcrystals are able to bind to the surface of Escherichia coli cells, allowing its tracking [16].

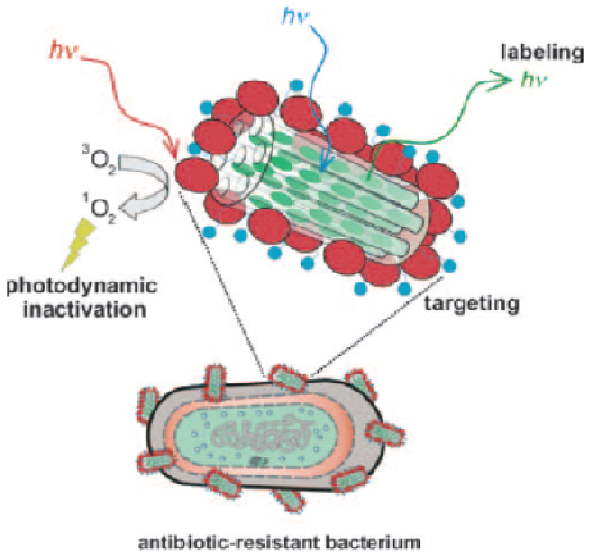

Figure 2.1.3. Scheme of the multifunctional nanomaterial used to target, label, and photoinactivate antibiotic-resistant bacteria. ZL is loaded with the DXP dye (green ellipsoid), and its surface is functionalized with a phthalocyanine derivative (red ellipsoid) and with amino groups (blue circles), where the latter provide non-covalent binding of the hybrid nanomaterial to the bacterial surface.

2.2. MIMICKING THE GREEN PLANTS - ARTIFICIAL ANTENNA SYSTEMS

The pioneering work of Theodor Förster allowed to understand the basic principles that govern the transport of electronic excitation energy, that is at the base of the natural and sophisticated process of photosynthesis. Green plants, in fact, can be thought as natural antenna systems (Figure. 2.2.1).

The light absorbed by the chlorophyll molecules, regularly arranged and hold at fixed positions by means of proteins, is transported to the reaction center, providing the energy necessary for chemical processes to be initiated. A green leaf consists of millions of such well organized antenna devices.

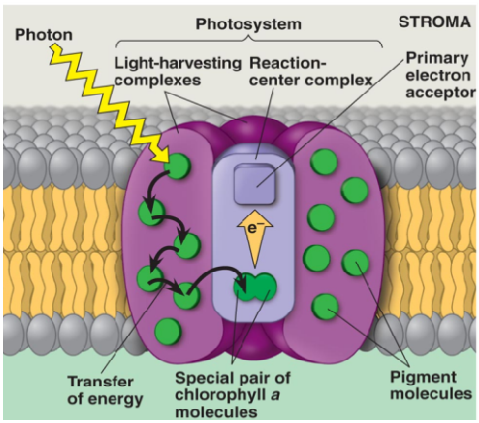

Figure 2.2.1. Scheme of the photosynthesis process.

Is it possible to recreate systems with similar light harvesting properties in laboratory? This question inspired the work of the group of Calzaferri and other authors [9,17] in designing a model to mimic the key functionality of the green plants antenna system and to realize devices with various fields of application, as photochemistry, technology and biology. By their experience with zeolite materials Calzaferri et al. [9,17] developed systems built by the arrangements of different dyes in the zeolite microporosity, called artificial antenna systems. In their studies these authors explained as a 1-dimensional channel system has the advantage of being the simplest possible system. In Figure 2.2.2 an artificial antenna is represented where the donor molecules are in green and the acceptors in red. A donor, being excited by photon absorption, transfers its electronic excitation (via FRET) to an unexcited neighbor. After a series of such steps, the

electronic excitation reaches a luminescence trap (acceptor molecule) and is then released, for example, as fluorescence. The acceptors are thought to mimic the “entrance to the reaction center ” of the natural antenna [18,19].

According to the Förster theory [20], the largest Energy Transfer rate constant (EnT) is observed if the electronic transition dipole moments (ETDMs) of the donor and acceptor molecules are oriented parallel to the channel axis. Electronic excitation energy transport can be extremely fast in such systems because of its low dimensionality.

Different zeolites with suitable channel dimensions, such as $AlPO_4$-5 [21, 22], zeolite Y, [23], zeolite L, [24,25] and mesoporous materials such as MCM-41 [26], have been successfully envisaged for realizing the supramolecular assembly of dye molecules. In particular, the Calzaferri group [18,19] found that zeolite L is an excellent host because its structure allows, through geometrical constraints, the realization of extremely high concentrations of well - oriented molecules that behave essentially as monomers.

The structure of zeolite L will be described in detail, in chapter 4.

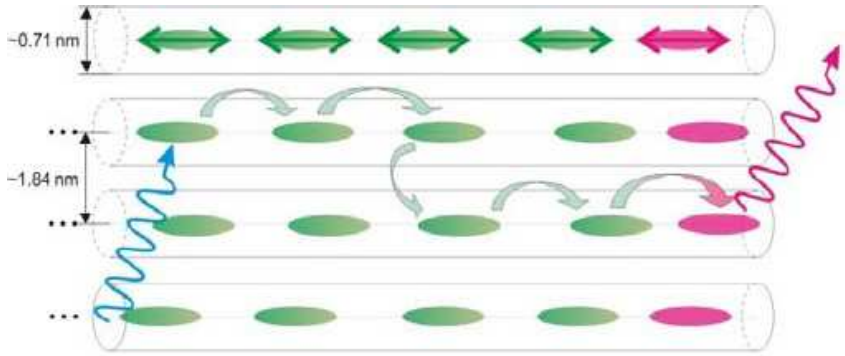

Figure 2.2.2. Schematic overview of an artificial photonic antenna.

2.3. SUPRAMOLECULAR ORGANIZATION OF ORGANIC DYES INSIDE THE ZEOLITE L CHANNELS

Organic dye molecules tend to form aggregates, which are known to cause fast thermal relaxation of the electronically excited states. Nevertheless, they are usually unstable under irradiation, especially when present as monomers. Protection against bimolecular reactions, but also unwanted isomerization reactions, is possible by encapsulating them in an appropriate host such as zeolite L. Furthermore, such encapsulation provides a protection from the environment and avoids for example quenching of the photoluminescence due to photo oxidation.

Zeolite L (ZL) allows to design and prepare a large variety of highly organized host – guest systems; some relevant types are illustrated in Figure 2.3.1. Important steps in the development of these composite materials are the preparation of materials containing two or more different guests (single and mixed dye materials), the sequential filling with different dyes, that leads to sandwich structures (antenna materials), and the invention of the stopcock principle (stopcock plugged antenna materials).

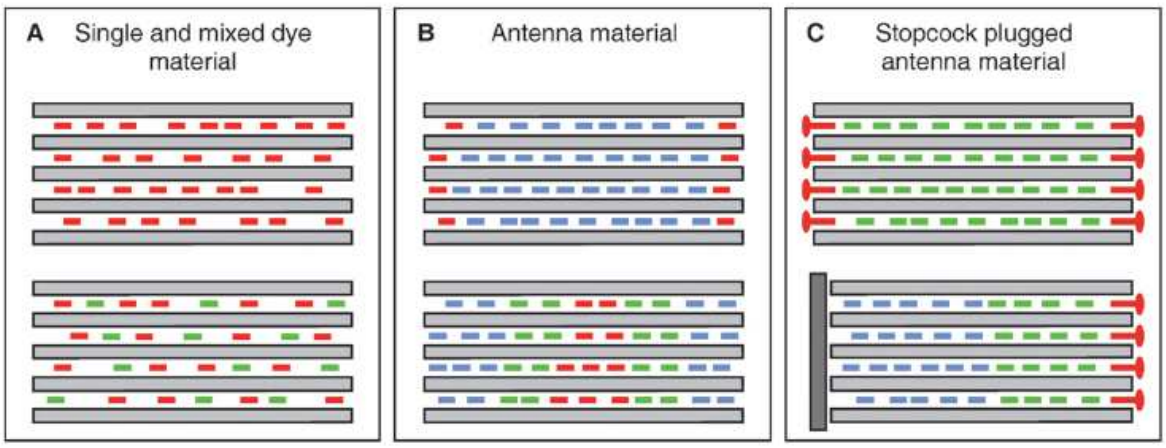

Figure 2.3.1. Representations of supramolecular organized ZL-dye- composites. (A) Single and mixed dye materials are obtained by either loading zeolite crystals with one kind of dye (top) or by simultaneous insertion of different dye molecules (bottom). (B) Antenna materials can be prepared by the sequential insertion of different dyes. (C) Stopcock-plugged antenna materials are obtained by modifying either bidirectional (top) or unidirectional (bottom) antenna materials with stopcocks.

Single and mixed dye materials: consist of ZL crystals that contain only one dye. In few cases, it was possible to prepare mixed dye materials. A condition for the preparation of such materials is that both dyes enter the channels at about the same rate [5].

Antenna materials: obtained by consecutive incorporation of dyes with appropriate size and shape so that can enter the channels, without gliding past each other. The resulting dye-loaded materials can be divided into compartments where the density of one dye is dominant. If first a donor and then an acceptor are incorporated, electronic excitation energy is transported from the center to the channel entrances after selective excitation of the donor (vice versa if an acceptor is incorporated first). Domains of two, three or even more different dyes are feasible.

Stopcock-plugged antenna materials: obtained modifying the channel ends of dye-loaded ZL by specific closure molecules, which can only partially enter the channels. The stopcock principle is based on a dye that consists typically of an head and a tail. Due to size restrictions, only the tail can enter the channel [5, 25, 27-32]. Depending on their nature, stopcocks can be bound either by physisorption and electrostatic interaction, or by covalent bonding. Examples of stopcocks are given in Table 2.3.1. Since these molecules are located at the interface between the interior of a ZL crystal and the surrounding, they can be considered as mediators for communication between molecules inside the nanochannels and objects outside the crystals. Stopcock molecules can also be used to prevent penetration of small molecules such as oxygen and water or to hinder encapsulated dye molecules from leaving the channels [33].

Table 2.3.1. Examples of stopcock molecules that can been used in ZL/dye composites.

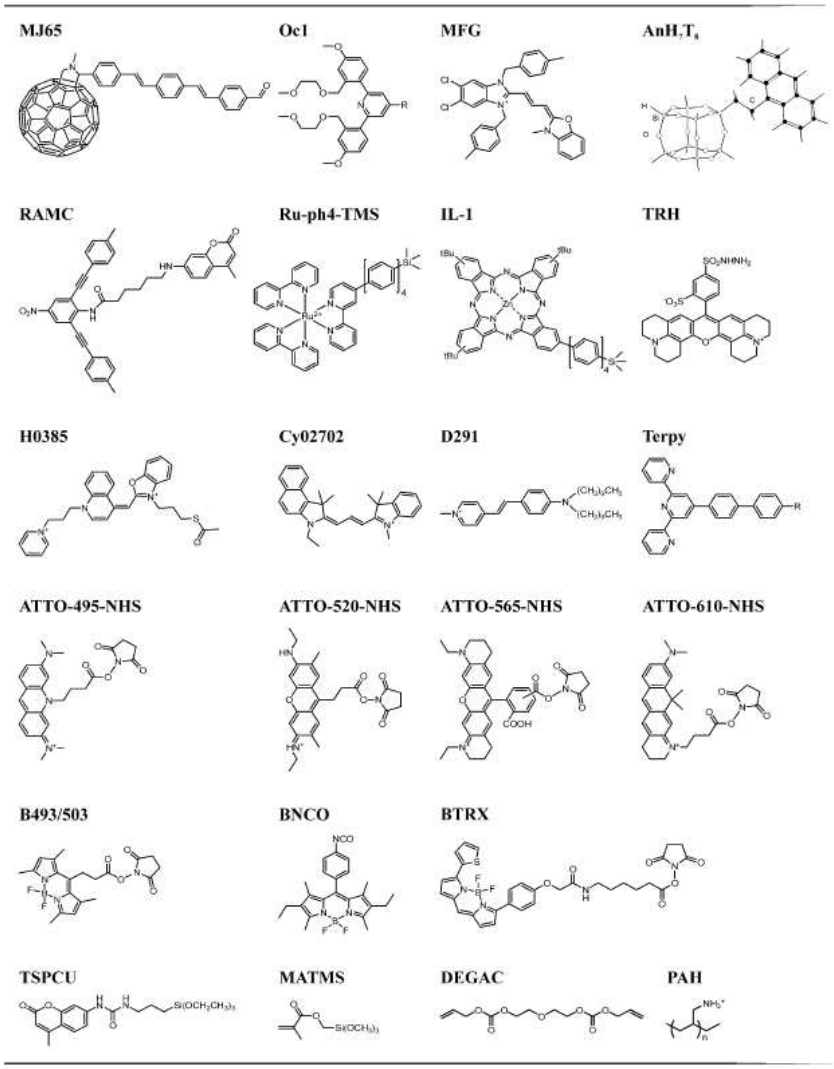

The orientation and the packing of the dyes in the channels has a large influences on the optical properties of the host-guest materials (Figure. 2.3.2).

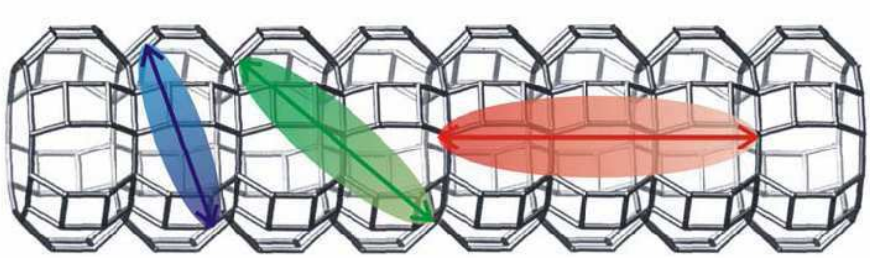

Figure 2.3.2. Influence of size on the position of the dye molecule respect the channel axis of ZL [34].

Guests can be chosen in such a way that: i) they can stack inside, forming, e.g. H-type aggregates (i.e. molecules in which the transition moments of individual monomers are aligned parallel to each other but perpendicular to the line joining their centers, *face-to-face arrangement*) [35]; ii) they can touch each other at van der Waals distance, leading to J-aggregate coupling (i.e. a one-dimensional molecular arrangement in which the transition moments of individual monomers are aligned parallel to the line joining their centers, *end-to-end arrangement*), [36] or iii) they can arrange in a such a way that intermolecular interaction becomes negligibly small.

In particular: J-aggregate exhibit a narrow peak (J-band) red-shifted in the absorption spectrum with respect to the monomer absorption. The absorption spectrum of the H-aggregate consists of a blue-shifted band (generally not as narrow as the J-band) respect to the monomer absorption.

The energy shift of the absorption bands of the aggregates has been explained by exciton theory. When two identical molecules come to close proximity to each other, their transition dipole moments will start interacting and lead to a so called “ excitonic coupling” (Figure. 2.3.3)

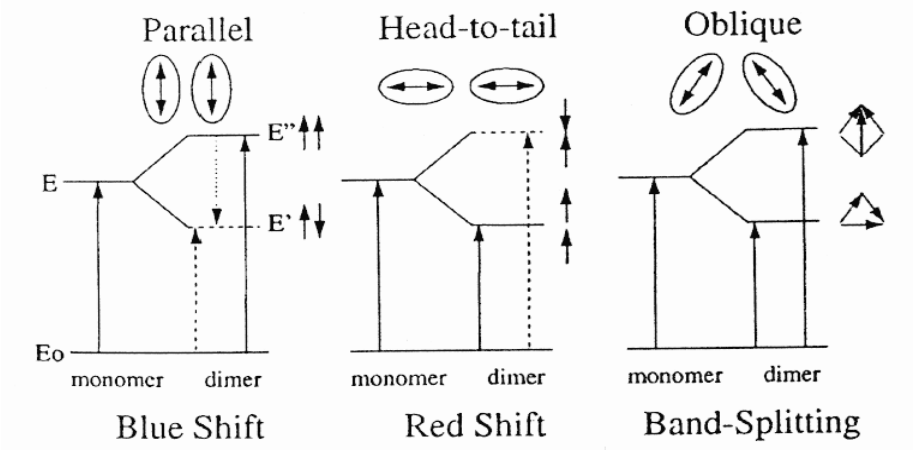

Figure 2.3.3. Schematic representation of the relationship between chromophore arrangement and spectral shift based on the molecular exciton theory.

When two dipoles are brought to close proximity, side by side, their relative orientation (parallel *vs.* antiparallel) will cause two things to happen:
a) the energy of individual molecules, *E*, will split into two new states with the energies *E''* and *E'*, parallel dipoles repel each other and get the higher energy state, while the antiparallel dipoles attract each other and lower the energy of that state;
b) parallel dipoles make up an overall higher dipole moment, *i.e.* stronger absorption, while antiparallel dipoles cancel each other to make a weak absorption, resulting in a blue shift of absorption (H-aggregates).

Similarly for head-to-tail arrangement, the lower energy state has larger transition dipole moment and the effect is a red shift in the absorption (J-aggregates). The intermediate, oblique orientation, results in band splitting - two bands appearing at lower and higher energy.

In the dipole-dipole approximation, the interaction energy (V_{12}) between two dipoles, μ_1 and μ_2, separated by distance *R*, is given by the formula:

$$V_{12} = \frac{\vec{\mu}_1 \cdot \vec{\mu}_2}{R^3} - 3\frac{\left(\vec{\mu}_1 \cdot \vec{R}\right)\left(\vec{\mu}_2 \cdot \vec{R}\right)}{R^5}$$

which tells us that the shift in the absorption bands, declines dramatically with increasing distance between the dipoles. Obviously, intermediate (oblique) orientations have two bands with the splitting between them depending on both the separation distance and the angles between dipoles and the vector connecting them. Such exciton coupling between more than

two molecules allows substantially to extend absorption spectrum, that can result into an increase of the efficiency of light collection.

Calzaferri and co-workers [18, 29, 37-40] classified the guest dye molecules in three categories on the basis of the size with respect to the channel dimensions (Figure 2.3.2)

(i) molecules which are small enough to fit into a single unit cell. Examples are biphenyl, 4-hydroxy-TEMPO, 9-fluorenone, and methyl viologen (MV^{2+}) [41];

(ii) molecules with a size which makes it difficult predict whether they align along the c-axis or if they find a different orientation to fit into a single unit cell (i.e oxonine, pyronine, and thionine);

(iii) molecules which are longer than the channel diameter and that have no other choice but to align along the zeolite channels (es. Diphenylhexatriene (DPH)).

2.4. INSERTION OF THE DYE INTO ZL

Three different methods for dye incorporation have been established in [34]:

(1) ion exchange: possible only for cationic dye molecules which can be encapsulated into zeolites replacing the charge compensating cations present in the channels;

(2) gas-phase adsorption: used for neutral chromophores, which are inserted into the zeolite porosities via sublimation. Incorporation by gas phase requires a preceding zeolite dehydration since H_2O molecules hinder the guests loading;

(3) in-situ encapsulation: the molecules are encapsulated directly during the zeolite synthesis.

The same authors introduced a parameter, bearing the information on dye concentration, based on purely geometrical (space - filling) properties of ZL , that shows how much the channels are filled with dye molecules.

They also define the *loading*, or occupation probability *p*, of a ZL/dye material as follows:

$$p = \text{Number of occupied sites/Total amount of sites}$$

where the Number of occupied sites (n_s) represents the number of unit cells occupied by a dye molecule. It can, for example, be equal to 1, 2, or 3 but it must not necessarily be an integer number. The loading ranges from 0 for an empty ZL to 1 for a fully loaded one.

The dye concentration of a dye – ZL material $c(p)$ can be expressed as a function of the occupation probability as follows:

$$c(p)=0.\ 752\ p/ns\ (mol/L)$$

A wide variety of molecules has been successfully incorporated into ZL or used as stopcocks (Table 2.3.1). Tables 2.4.1 and 2.4.2 give some examples of cationic or neutral dyes inserted in ZL channels.

Table 2.4.1. Examples of cationic and zwitterionic dyes inserted into the channels of ZL.

ProFl$^+$	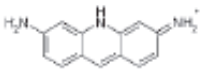	Th$^+$	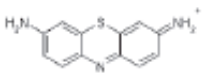	MC^{2+}	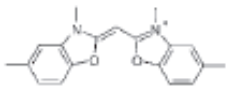
Py$^+$	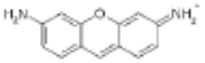	MeAcr$^+$	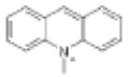	PC20$^+$	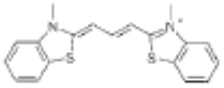
PyGY$^+$	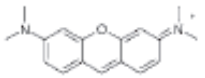	AY	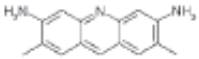	PC21$^+$	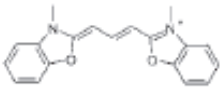
PyB$^+$	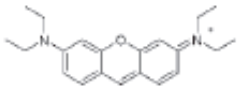	AQ	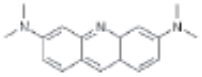	BTMPI$^+$	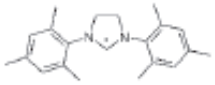
Ox$^+$	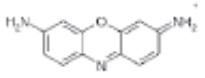	MV^{2+}		DSM$^+$ (n = 1)	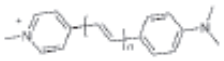
DEOx$^+$	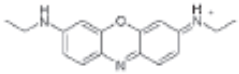	BDP$^+$		SQ III $R = CH_3$ SQ(JG9) $R = (CH_2)_3CH_3$	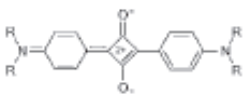
Ox1$^+$	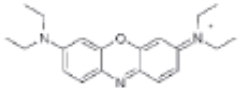			$Ln^{3+}L_n$	Ln^{3+} = Eu^{3+}, Tb^{3+}, Er^{3+} L = bpy, benzophenone

Table 2.4.2. Examples of neutral dyes inserted into the channels of ZL.

BP	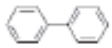	Naphthalene		NY43	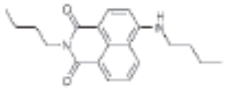
*p*TP		Anthracene	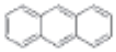	JCG65	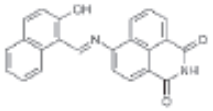
DPH		ResH	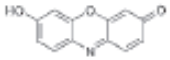	Hostasol red	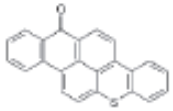
PBOX	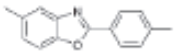	*N*-ethylcarbazole	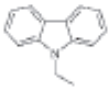		
MBOXE	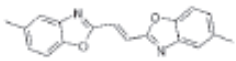	Fluorenone	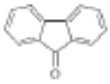	Hostasol yellow	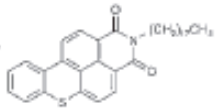
POPOP	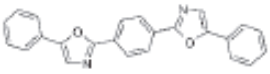	DCS			
DMPOPOP	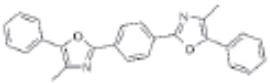	Stilbene		PR149	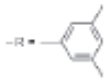
Isoviolanthrone		Azobenzene	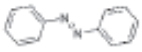	DXP	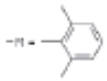
SG 5		DANS		Perylene-73	
DM4T	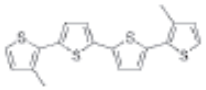	TTF		Hydroxy-TEMPO	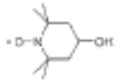

References

[1] Calzaferri G., Huber S., Maas. H., Minkowski. C, (2003) *Angew. Chem. Int. Ed*., 42, 3732–3758

[2] Huber S., Calzaferri G. (2004), *ChemPhysChem* ,5, 239–242

[3] Koeppe R., Bossart O., Calzaferri G., Sariciftci N.S. (2007),*Sol. Energy Mater. Sol. Cells* , 91 , 986–995

[4] Calzaferri G., Li H. (2008) Mimicking the antenna system of green plants, Photonics for Solar Energy Systems II, edited by Andreas Gombert Proc. of SPIE Vol. 7002, 700202-2

[5] Calzaferri G., Lutkouskaya K. (2008) *Photochem. Photobiol. Sci*. ,7, 879 – 910

[6] Batchelder S., Zewail A.H., Cole T. (1979), *Applied Optics*, 18 , 3090-3110

[7] http://mtlsites.mit.edu/energy/agenda/poster-mulder

[8] Kittidachachan P., Danos L., Meyer T.J.J., Alderman N., Markvart T. (2007), *CHIMIA*, 61, 780–786

[9] Brühwiler D., Dieu L.-Q., Calzaferri G. (2007), *CHIMIA*, 61, 820–822

[10] Dieu L.-Q., Devaux A., López-Duarte I., . Martínez-Díaz M. V, BrühwileD. , Calzaferri G., Torres T. (2008), *Chem. Commun.*, 1187-1189

[11] G. Calzaferri, A. Zabala Ruiz, H. Li, Huber S., (2007) Patent WO, 2007/012216

[12] Strassert C. A. et al. (2009): *Angew. Chem*. Int. Ed. 48, 7928-7931

[13] Dougherty T. J., Gomer C. J., Henderson B.W., Jori G., Kessel D., Korbelik M., Moan J., Peng Q. (1998), *J. Natl. Cancer Inst*., 90, 889 – 905

[14] Juzeniene A., Peng Q., Mohan J.(2007), *Photochem. Photobiol. Sci*., 6, 1234 – 1245

[15] Hamblin M. R., Hasan T.(2004), *Photochem. Photobiol. Sci*., 3, 436 – 450

[16] Popovic Z., Otter M., Calzaferri G., De Cola L. (2007), *Angew. Chem.*, 119, 6301 – 6304

[17] Popovic Z., Otter M., Calzaferri G., De Cola L. (2007) *Angew. Chem*. Int. Ed., 46, 6188 – 6191

[18] Calzaferri, G. ; Gfeller, N. (1992) *J. Phys. Chem.*, 96, 3428-3435

[19] Gfeller , N.; Calzaferri, G. (1997). *J. Phys. Chem.* B, 101 , 1396-1408

[20] Förster T., (1948) *Ann. Physik*, 437, 55

[21] Caro, J.; Marlow, F.; Wu□st, M (1994). *AdV . Mater.*, 6 (5), 413- 416

[22] Ihlein, G., Schüth, F., Krauss, O., Vietze, U., Laeri, F.(1998) Adv.Mater. 10, 1117 – 1119

[23] Hoppe, R.; Schulz-Ekloff, G.; Wo□hrle, D.; Kirschhock, C.; Fuess, H.; Uytterhoeven, L.; Schoonheydt, R(1995). *Adv . Mater.,* 7 (1), 61 -64

[24] Calzaferri, G. (2001) *Chimia,* 55, 1009-1013

[25] Calzaferri G. , Pauchard M., Maas H., Huber S., Khatyr A., Schaafsma T(2002). *J . Mater. Chem* . , 12 , 1-13

[26] Onida, B.; Bonelli, B.; Lucco-Borlera, M.; Flora, L.; Otero Arean, C.; Garrone, E. (2001) *Stud. Surf. Sci. Catal.* , 135, 364

[27] Calzaferri, G., Brühwiler, D., Megelski, S., Pfenniger, M., Pauchard, M., Hennessy, B., Maas, H., Devaux, A., Graf, U. (2000). *Solid State Sci*., 2, 421-447

[28] Calzaferri G., Maas H., Pauchard M., Pfenniger M., Megelski S., Devaux A. (2002) *Advances in Photochemistry* , Editors D.C. Neckers, G. von Bünau, W.S. Jenks, Vol 27, 1-50.

[29] Calzaferri, G. ; Huber, S. ; Maas, H. ; Minkowski, C. (2003). *Angew. Chem*. Int. Ed. Engl. , 42 , 3732-3758

[30] Calzaferri, G. (2008). EU and US patents. EP 1335879B1, US 6932919B2, US7327012 ,

[31] Maas, H.; Calzaferri, G. (2002). *Angew. Chem*. Int. Ed. Engl., 41 , 2284-2288

[32] Calzaferri, G. (2008) Il Nuovo Cimento, 123B , 1337-1367

[33] Albuquerque, R.Q.; Calzaferri, G. (2007) *Chem. Eur. J.* , 13 , 8939-8952

[34] Bruhwiler D. et al (2009) *J. Mater.Chem*., 19, 8040-8067

[35] Hashimoto, S.; Hagiri, M.; Matsubara, N.; Tobita, S. (2001) *Phys. Chem. Chem. Phys*., 3, 5043−5051

[36] Calzaferri, G.; Devaux, A. Ramamurthy, V., Inoue, Y., (Editors).; John Wiley & Sons: New York, 2011; Chapter 9, 285−387

[37] Calzaferri,G., Bossart O., Brühwiler D., Huber S., Leiggener C., Van Veen K M. , Zabala Ruiz A. (2006),C. R. *Chimie* 9, 214-225

[38] Pfenniger M. and Calzaferri G. (2000). *Chem.Phys.Chem*., 1 , 211-216,

[39] V. Ramamurthy, D.R. Sanderson, D.F. Eaton (1993), *J. Am. Chem. Soc*., 115 10438–10439

[40] Pauchard M., Devaux A. and Calzaferri G (2000) *Chemistry, a European Journal* , 6, 3456-3470

[41] Hennessy B., Megelski S., Marcolli C., S. Valery, Bärlocher C. and Calzaferri G. (1999) *J. Phys. Chem. B*, 103, 3340 - 3351

3. ZEOLITE THERMAL BEHAVIOUR

3.1. Thermal behavior of zeolites

The study of the thermal behavior of zeolites is of fundamental importance since the most relevant properties of zeolites, such as catalytic activity, adsorption capacity, and molecular sieving can be exploited when zeolites are in their anhydrous form. Moreover zeolites, and in particular zeolites in their acid form, are widely used in catalysis and these kind of processes, such as hydrocarbon cracking, require quite high temperatures.

The most common method used to study zeolite dehydration processes is thermogravimetric analysis (TG, DTG) and differential thermal analysis (DTA). The structural studies began during the 70s, with the first experiment based on data collected by single crystal “ex-situ” XRD.

In recent years the develop of CCD or Image Plate detector systems and/or synchrotron radiation sources allowed faster data collection with the possibility to obtain a continuous picture of the dehydration process. In this way the in situ time resolved dehydration can be followed. For this PhD thesis the knowledge of the response of ZL to the thermal treatment is essential as the insertion of neutral dyes (such as Fluorenone and tB-DXP) requires a previous dehydration of the zeolite to facilitate the penetration of the molecules. The thermal properties of the zeolite L will be shown in detail in the chapter 5. In the following paragraphs the classification of zeolites based on their thermal behavior, the parameters that affect their thermal response and the changes induced by high temperature treatment in their structure will be quickly summarized.

3.2. CLASSIFICATION OF ZEOLITES BASED ON THEIR THERMAL BEHAVIOR

Alberti and Vezzalini [1] divided zeolites in 3 different categories based on the framework response to the heating treatment, a classification in agreement with that proposed more recently by Bish & Carey [2]:

- Group I: dehydration is completely reversible and the rearrangement of the extraframework cations and water molecules occurs without substantial modifications of the framework and of the cell volume (e.g. mordenite);

- Group II: dehydration is reversible or almost completely reversible, but the framework is subjected to important distortions with significant decrease of the cell volume (e.g. clinoptilolite);
- Group III: dehydration is accompanied by changes in the framework due to the breaking of some T - O - T bridges (e.g. barrerite, stilbite and stellerite).

Baur [3] classified zeolites on the basis of framework flexibility as follows:

1) inflexible frameworks, which are quite rigid and do not show important structural modifications when heated, whatever is their chemical composition;

2) flexible frameworks, which in turn are divided into the following groups:

2.1) collapsible frameworks, in which hinges (oxygen atoms connecting two adjacent tetrahedra) co-rotate and the distortion of the framework is enhanced;

2.2) non-collapsible frameworks, in which T-O-T hinges antirotate, so compression at one hinge needs tension at another hinge and vice versa. Unit cell variations in this case are modest (e.g. zeolite A).

It is interesting to note that some zeolites can show different thermal behavior depending on the thermal conditions (temperature of heating, time of heating, time elapsed after heating, X-ray diffraction data collected near or far from equilibrium conditions). For example, brewsterite, when heated under vacuum and analyzed by ex-situ XRD on single crystal, shows almost complete dehydration, T-O-T bond breaking inside the 4-rings and tetrahedral (T) cation migration towards a new site with the formation of statistically occupied face-sharing tetrahedra. If the same sample is heated and the powder diffraction data are collected in-situ, no T-O-T breaking is observed, as a consequence of different kinetics.

Cruciani [4] defined the empirical Stability Index (SI), a parameter aimed to quantify the zeolite thermal stability, which considers the collapse/breakdown temperature (determined by X-ray diffraction measurements), the maximum volume contraction and the presence of phase transformations. The correlation between SI and the Si/Al ratio confirmed the relevance of this parameter in controlling the thermal stability of zeolites.

The same author observed that: (i) zeolites with Si/Al 3.80 are very stable; (ii) zeolites with Si/Al 1.28 are fairly unstable; and (iii) zeolite stability in the intermediate Si/Al range cannot be directly predicted from the Si/Al ratio.

3.3. STRUCTURAL CHANGES INDUCED BY THERMAL TREATMENT

During dehydration –by heating or under vacuum- zeolites are subjected to different types of structural changes:

1) Contraction of the unit cell volume, due to the release of water molecules and/or of the organic molecules used as template;

2) Migration of extraframework cations, which, losing coordinating water molecules, tend to change coordination site; in general, weakly polarizing cations migrate towards the framework oxygen atoms causing deformations of the angles T-O-T;

3) Displacive or reconstructive phase transitions, also associated with the formation of transient and metastable phases;

4) Breaking of T-O-T bonds and formation of new bridges with consequent structural collapse;

5) Structural breakdown, complete amorphization or recrystallization.

3.4. FACTORS GOVERNING THE ZEOLITE THERMAL BEHAVIOUR OF ZEOLITES

Dehydration is a complex process and there are no general rules that allow to predict the thermal behaviour of a zeolite. In general, as discussed in the review paper of Cruciani [4], several factors may control zeolite thermal behavior:

a. Si/Al ratio - Thermal stability increases with the Si/Al ratio. This depends on the fact that the energy for Si-O bond breaking is greater than the energy required to break an Al-O bond. This is not a general rule, in fact some zeolites with a low Si/Al ratio (merlinoite, laumontite, bikitaite, analcime and chabazite) show more stable thermal behaviour than zeolites with higher Si/Al ratio (tschernichite, heulandite, barrerite and brewsterite).

b. size and ionic potential (Z/r) of the exchangeable cations - Zeolites with monovalent cations (e.g. K^+ and Na^+) are generally more stable than those containing divalent ones (e.g. Ca^{2+}, Mg^{2+}).

Furthermore, cations with a great ionic radius (e.g. K^+ in clinoptilolite) prevent the collapse of the structure for a packing effect, while those with smaller ionic radius (e.g. Na^+, Ca^{2+}) are too small to keep the channels expanded [5].

c. coordination of bare cations after dehydration - The extraframework cations, after zeolite dehydration, lose their coordination with water molecules and are forced to move to find a

new low-energy configuration, and a new coordination. Consequently, they come closer to the oxygens of the framework by creating new links with them and causing distortions in the T-O-T bonds. Such distortions may also lead to breakage of these bridges.

d. topology of the framework - Zeolites with a high framework density (FD) have thicker walls between pores and channels, so they are more stable [6,7]. Furthermore regular shaped tetrahedral n-rings (and T-O-T angles) are more stable than zeolites with distorted T-O-T. Also the presence of specific unit or sub-structural units -such as rings or columns of 5 tetrahedra, 4 or 6 rings that surround the channels- lead to more rigid structure, and often no contraction of the channels during the heating is shown.

e. other factors (pressure of water, amount and duration of treatment, or conditions close/far from equilibrium, crystal size, heating rate).

References

[1] Alberti A., Vezzalini G. (1984), Proceedings of the Sixth International Zeolite Conference, Butterworths

[2] Bish D. L., Carey J. W. (2001), *Natural zeolites: Occurrence, Properties, Applications*, 45, 403-452

[3] Baur, W. H. (1992), *Journal of Solid State Chemistry*, 97, 243-247

[4] Cruciani, G. (2006), *Journal of Physics and Chemistry of Solids*, 67, 1973-1994

[5] Koyama K., Takeuchi Y. (1977), *Zeitschrift für Kristallographie*, 145, 216-239

[6] McDaniel, C. V., Maher, P. K. (1976), *Zeolite Chemistry and Catalysis*, (ed. J.A.Rabo), American chemistry society, Waschington, 285

[7] Tschaufeser, P., Parker, S. C. (1995), *J. Phys. Chem*., 99, 10609-10615

AIMS OF THE THESIS

This PhD thesis focuses on host-guest dye-zeolite L systems, where the photoactive molecules are organized in the one-dimensional channels of the zeolite. The excellent optical properties, chemical stability and biocompatibility of these composites make them key components of artificial antenna systems, sensors, LED_S and bio-nano devices such as markers of tumor cells in-vivo.

The artificial antenna systems [1-3] have been mostly realized using the zeolite L as host because of its high versatility. In fact, the size and shape of its crystallites can be tuned over a wide range; a nanometer sized crystal consists of many thousand one-dimensional channels oriented parallel to the zeolite *c* axis and, as a consequence, strong geometrical constraints are imposed to the encapsulated dye molecules. This leads to a supramolecular organization of a very high concentration of the guests non- or very weakly- interacting in the channels.

Owing to the relevance of dye-zeolite L hybrids for environmental sustainability and human health, in this work they will be studied at molecular level detail, to unravel and understand the host–guest interactions that govern the functionality and the optical efficiency of these composites.

In order to achieve this aim, three dye- ZL composites have been prepared and investigated with an integrated experimental-theoretical strategy, based on the use of in-situ and ex-situ X-ray diffraction, with both conventional and non-conventional sources, thermal gravimetric analysis, infrared spectroscopy, UV-Vis and luminescence experiments, and molecular dynamics simulations.

The guest molecules studied belong to two different dye species: neutral, Fluorenone and tB-DXP and cationic, thionine.

In the chapter 4.1.2. the structure, chemical and optical properties of the pure dye molecules will be reported in detail. The neutral molecule Fluorenone has been chosen because is an excellent probe molecule for studying the interaction of the carbonyl functional group (C=O) inside the channels of ZL. In fact, theoretical studies showed its high stability inside ZL due to the strong interaction of the C=O group with the ZL extraframework potassium [4].

Dye molecule tB-DXP, belonging to the perylene family, was recently synthetized [5] and inserted into ZL because shows high quantum yield and strong absorption in visible light and hence a new promising composite. Its fascinating properties are due to the presence of a different end-substituent, respect to the normal perylene core, that can act as a spacer between

neighbor molecules. This feature leads to an increase of the minimum contact distance and hence to a decrease of the interaction with the neighbor molecule, that would entail to the formation of J- aggregate, well known to cause a fluorescence quenching effect. For this reason it would be of extremely interest to investigate its orientation in the zeolite channels and its interactions with the channel walls that favor so surprising properties.

The cationic thionine was chosen since ZL framework cannot accommodate thionine dimers, such as H-aggregates due to the size of the molecule, so the composites show intense fluorescence within the zeolite channels [6]. Moreover thionine contains a sulfur atom, a relatively heavy atom that can be easily located by X-ray diffraction respect to other dye molecule consisting of only C, N and O atoms, more difficult to localize in the relatively heavy matrix of a zeolite.

A recurring question that arises in the study of encapsulated molecules regards the location and the number of guests trapped in the zeolite voids. A detailed structural characterization of the alignment/orientation of the dye into the zeolite channels is still lacking. This aspect has a great importance because the organization of the molecules can affect the optical performances of the composites. For this reason structural investigation can provide useful information for understanding the mechanisms which can explain the observed optical phenomena.

References

[1] Brühwiler D., Dieu L.-Q., Calzaferri G., (2007). CHIMIA , 61 , 820–822

[2] Lopez-Duarte, L.-Q. Dieu, I. Dolamic, M. V. Martinez-Diaz, T. Torres, G. Calzaferri, D. Brühwiler (2011) *Chemistry - A European Journal* 17 1855 - 1862.

[3] Calzaferri G., Zabala Ruiz A., Li H., Huber S., PCT/CH2006/000394; priority US 60/698,480 and CH 1266/05 (2005)

[4] Fois, E.; Tabacchi, G.; Calzaferri, G. J. (2010) *Phys. Chem. C*, 114, 10572 – 10579

[5] Devaux A., Calzaferri G., Miletto I, Cao P., Belser P., Brühwiler D., Khorev O., Häner R., Kunzmann A. (2013) *J. Phys. Chem. C*, 117, 23034-23047

[6] Ramamurthy V., Sanderson D.R., and Eaton D.F. (1993) *J. Am. Chem. soc.* 115, 10438-10439

4. MATERIALS AND METHODS

4.1. Materials

In this section a detailed crystallographic and chemical characterization of zeolite L and dye molecules used in this study will be provide.

4.1.1. Zeolite L structural and chemical features

The most attractive antenna systems are based on the potassium zeolite L [1-7]. Synthetic ZL (ideal formula $K_6Na_3Al_9Si_{27}O_{72}{\cdot}21H_2O$, framework type LTL [8], (s.g.P6/mmm) (Figure 4.1.1.1 a,b), configures itself as an ideal host matrix because its arrays of parallel channels imposes severe space restrictions and geometrical constraints to any inserted guest species.

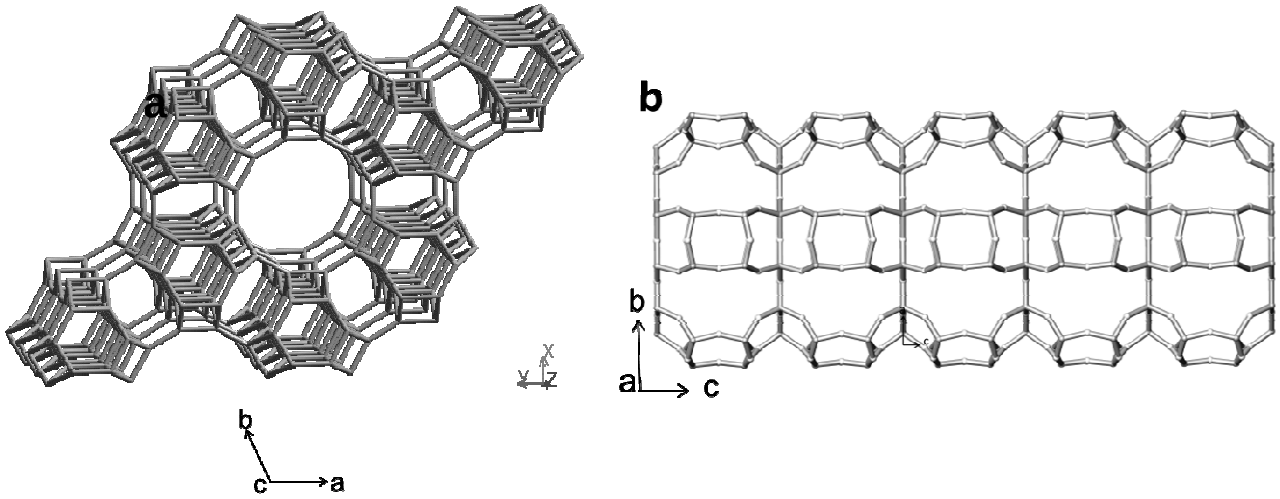

Figure 4.1.1.1. Projection along [001] (a); side view (b) of the 12MR channel running along the *c* axis.

As a result, very high concentrations of well oriented dye molecules can be obtained [1,9,10]. In the 1950s, the scientists of the Linde Company, a division of Union Carbide Corporations, were the first to synthesize zeolite Linde type L [11,12]. Since its first synthesis, zeolites with LTL framework type have been reported in various extraframework cationic forms, tetrahedral ion and hydration status, such as: hydrated (Na, K)-L [13], hydrated (K,Ba)-L [14], K-GaSi-L [15], Rb-GaSi-L [16], AlPO-LTL [17], LZ-212 [18]. The natural counterpart of zeolite L is perlialite [19].

The LTL framework [13, 20] is built from columns of cancrinite cages stacked with double six membered rings (D6R) along the *c* axis. These columns are connected to form larger circular 12-ring (12MR) channels and smaller elliptical 8-ring (8MR) channels, all running along the *c* axis (Figure 4.1.1.1 a and b). The main channels are connected to the parallel 8-ring channels by a non-planar boat-shaped 8MR.

Barrer and Villiger [13] (here after named BV) were the first to investigate the structure of the synthetic zeolite L. These authors localized four extraframework cationic sites [13]:

(i) site **KA** – in the center of the D6R – is partially occupied by both K and Na and is coordinated to six framework oxygen atoms;

(ii) site **KB** – in the center of the cancrinite cage – is fully occupied by K and is coordinated to six framework oxygen atoms;

(iii) site **KC** – located in the center of the 8MR channel, midway between the centers of two adjacent cancrinite cages – is occupied by K (with an occupancy factor of 0.9) and is coordinated by four framework oxygen atoms;

(iv) site **KD** – the only cation site found in the main 12MR channel – is partially occupied by Na and is coordinated to six framework oxygen atoms and two water molecules.

The BV sample contains 21 water molecules, distributed over eight extraframework sites in the main channel. These sites are partially occupied and weakly bonded to the framework.

Lee et al [16] determined that in the rubidium gallosilicate form, water molecules constitute a sequence of hydrogen bonded water clusters and cation-water layers running along *c*. Newsam [22] reports the results of a neutron powder diffraction study – performed at 298 and 78° K – of an in-vacuum-dehydrated potassium zeolite L and of the same zeolite containing perdeuterio-benzene molecules. The average framework geometry exhibits only small changes as a consequence of dehydration or benzene sorption, suggesting that the LTL framework is rather inflexible. The same author refined the structure of the dehydrated gallium zeolite L [15] and underlined that the non-framework cation configuration is similar to that described for the aluminum ZL [13], suggesting that little change in cations distribution accompanies dehydration.

For this PhD thesis two different synthetic potassium ZL samples have been studied. One, named *som27,* has been synthetized, in the laboratory of the Institut Charles Gerhardt, Montpellier, with the following method: a template solution A was prepared by dissolving 6 g KOH (SdS) and 3.15 g $Al(OH)_3$ (Merck) in 10 mL of de-ionized water. The solution was

boiled until clear, cooled to RT and restored to 10 mL volume by addition of water. A solution B was prepared by diluting 30 g Ludox HS-40 (Dupont) with 20 g of H_2O. Then 3 mL of 0.01 M $Mg(NO_3)_2$ solution, corresponding to a Mg/silica molar ratio 6900, were added to solution B in order to improve the selectivity of the synthesis [22]. Solutions A and B and a further 4 mL of water were poured into a 130 mL stainless steel autoclave while stirring. The autoclave was sealed and heated at 150 °C for 96 h without stirring. After cooling to RT, the suspension was filtered, washed with water until pH 9, and dried at 80°C.

Its chemical composition was determined using a Cameca SX 50 Electron microprobe on a pellet (experimental conditions: 20 kV, beam current 2 nA, the standards used were natural minerals) and thermogramivimetric analysis. The resulting chemical formula was $K_{8.46}$ [Al $_{8.35}$ Si $_{27.53}$]O $_{72}$·17.91 (H_2O), with an Si/Al ratio equal to 3.29. The cell parameters determined at room temperature (RT) are: a= 18.3367(1) and c= 7.5176(1) Å

The other ZL sample, named hereafter *Tosoh*, has been purchased by Tosoh corporation, and has Si/Al ratio equal to 2.9. The chemical composition of the zeolite was determined by X-ray fluorescence and thermogravimetric analysis. The resulting chemical formula is K $_{8.76}$ [Al $_{9.21}$ Si $_{26.80}$ O $_{72}$]•17.91 (H2O). The cell parameters determined at RT are: a= 18.3795(4) and c= 7.5281(2)Å larger than those obtained for *som27* and in agreement with the larger amount of Al.

In Figure 4.1.1.2 the comparison among the Synchrotron-XRPD patterns collected on *som27* and *Tosoh* ZL samples is shown. The patterns confirm the good crystallinity of both zeolite samples and the absence of impurities. Moreover, the two samples show also no substantial differences in intensity and peak position.

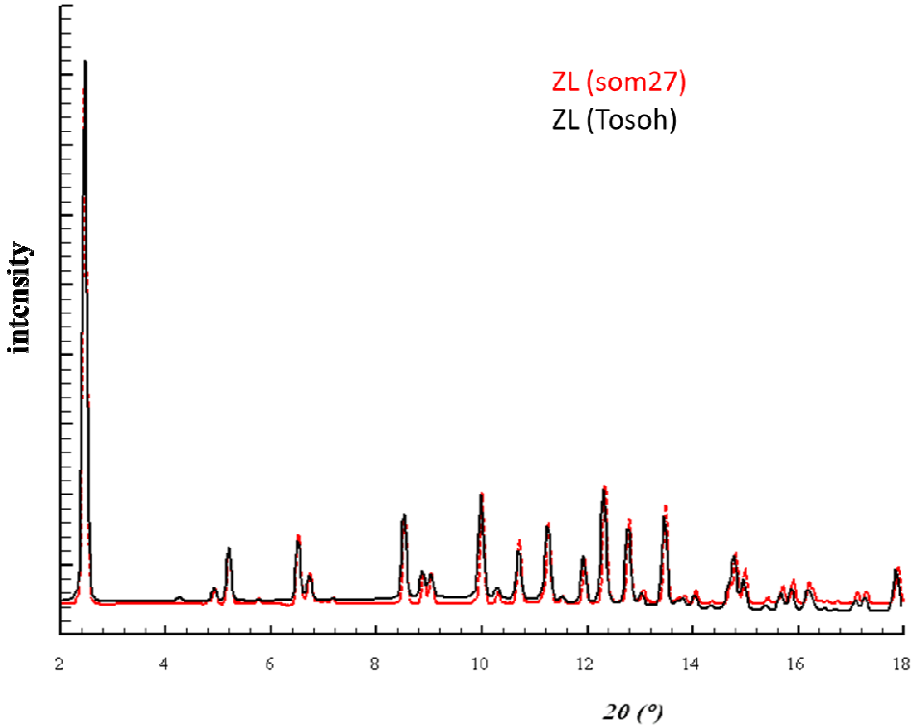

Figure 4.1.1.2. Comparison between the powder patterns of ZL (som27) an ZL (Tosoh) in the 2theta range: 2–18.

Structural refinements on both ZL samples were performed in the s.g P6/mmm with two independent tetrahedral sites: T1, in the cancrinite cage and T2, shared between the cancrinite cage and the D6R (Figure 4.1.1.3. a, b).

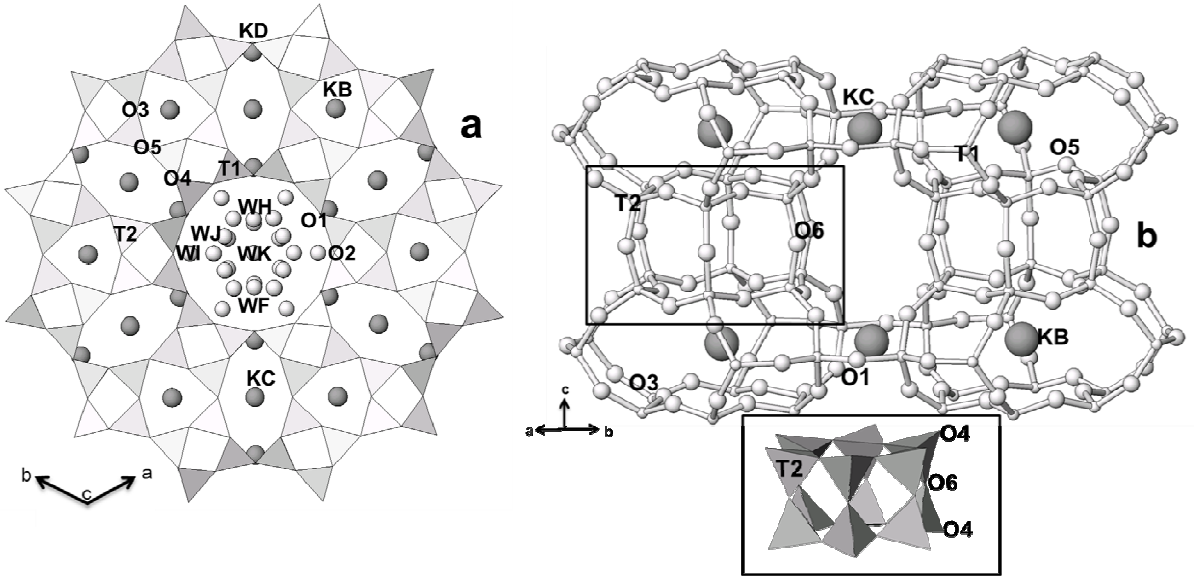

Figure 4.1.1.3. Projection along the *c* axis (a) and view from the inside of the 12MR channel (b) of *som*ZL at room temperature. Light grey: water sites; dark grey: K sites. The D6R is reported in the inset.

The framework structure determined at RT fully agrees with that reported by BV [13]. However, the preference of Al atoms for the T1 site suggested by Newsam [21], on the basis of the bond lengths determined by neutron powder diffraction, was not observed in our study.
Concerning the extraframework sites the following species distribution has been found in both ZL samples (Figure 4.1.1.3 a, b):
site **KB** – in the center of the cancrinite cage – is fully occupied by K and coordinated to six framework oxygen atoms;
site **KC** – located in the center of the 8MR channel, midway between the centers of two adjacent cancrinite cages, is fully occupied by K and coordinated to four framework oxygen atoms;
site **KD** –found in the main 12MR channel – is partially occupied and is coordinated to six framework oxygen atoms and two water molecules.
No extraframework species are found at the center of the D6R, in contrast with that reported in [13].
The water content, is almost similar in the two ZL samples and corresponds to about 18 molecules, distributed over five extraframework sites located in the main channel, labeled

WF, WH, WI, WJ and WK (Figure 4.1.1.3 a). All are partially occupied and weakly bonded to the framework.

As already mentioned in the chapter 1, the knowledge of the thermal stability of the ZL is of fundamental importance for the guest encapsulation. Incorporation by gas phase requires a preceding zeolite dehydration because H_2O molecules can hinder the molecules loading. For this reason in this thesis the dehydration mechanism study on the synthetic zeolite L, by in situ synchrotron XRPD experiment, has been performed (see chapter 5).

References

[1] Bruhwiler D., Calzaferri G., Torres T., Ramm J. H., Gartmann N., Dieu L.-Q. Lopez-Duarte I., Martinez-Diaz M. V. (2009) *J. Mater.Chem*., 19, 8040-8067

[2] Calzaferri G., Méallet-Renault R., Brühwiler D., Pansu R., Dolamic I., Dienel T., Adler P., Li H., Kunzmann A. (2011) *Chem.Phys.Chem*.,12 , 580-594

[3] Calzaferri, G. (2008) Il Nuovo Cimento, 123B , 1337-1367

[4] Calzaferri G., Li H., Brühwiler D. (2008) *Chem. Eur. J*., 14, 7442- 7449

[5] Calzaferri G. (2010) *Topics in Catalysis*, 53, 130 – 140

[6] Calzaferri G. (2012) *Langmuir* , 28, 6216 – 6231

[7] Gfeller N., Megelski S. , and Calzaferri G. (1998) *J. Phys. Chem. B*, 102 (14), 2433–2436

[8] Baerlocher Ch., McCusker L.B., Olson D.H. (2007) Atlas of Zeolite Framework Types, 6th ed., Elsevier, Amsterdam

[9] Calzaferri G., Huber S., Maas H., Minkowski C. (2003) *Angew. Chem. Int. Ed*. 42, 3732–3758

[10] Wang Y., Li H., Feng Y., Zhang H., Calzaferri G., Ren T. (2010) *Angew. Chem. Int. Ed*., 49, 1434–1438

[11] Wenzel R.N. (1936) *Ind. Eng. Chem*., 28, 988-994

[12] Gu Z.Z., Uetsuka H., Takahashi K., Nakajima R., Onishi H., Fujishima A., Sato O., *Angew. Chem*. Int. Ed. 2003, 42, 894

[13] Barrer R.M., Villiger H.Z. (1969) *Z. Kristallogr*., 128, 352–370

[14] Baerlocher Ch., Barrer R.M. (1972) *Z. Kristallogr*., 136, 245–254

[15] Newsam J.M. (1986) *Mater. Res. Bull*., 21, 661–672

[16] Lee Y., Kim S.J., Ahn D.C., Shin N.S. (2007) *Chem. Mater*., 19, 2277–2282

[17] Venkatathri N. (2002), *Indian J. Chem., Sect A*, 41, 2223–2230

[18] Breck D.W., Skeels G.W., (1985).U.S. Patent 4,503,023

[19] Artioli G., Kvick A. (1990) *Eur. J. Mineral*., 2, 749–759

[20] Gigli L., Arletti R., Quartieri S., Di Renzo F., Vezzalini G. (2013) *Microporous and Mesoporous Materials*, 177, 8–16

[21] Newsam J.M., (1989) *J. Phys. Chem*., 93, 7689–7694

[22] Verduijn J.P., (1993) U.S. Patent 5, 242, 675

[23] Larson A.C., Von Dreele R.B. (1994) Los Alamos National Laboratory Report LAUR 86–748

[24] Toby B.H., (2001) *J. Appl. Crystallogr*., 34, 210–213

4.1.2. GUEST SPECIES – DYES

An important and recurring question that arises in the study of encapsulated molecules regards the location and the number of guests trapped in the zeolite voids. In fact, a detailed structural characterization of the alignment/orientation of the dye into the zeolite channels and the quantification of the dye maximum loading are still lacking. This represent a fundamental issue, since the organization of the molecules can affect the optical performances of the composites. For this reason structural investigations can provide useful information for understanding the mechanisms responsible of the observed optical phenomena.

In the following a detailed characterization of the selected dyes, two neutral dyes (9-fluorenone and tB-DXP) and a cationic dye (thionine) will be reported.

The choice of the guests molecules to be encapsulated in the zeolite L was based on the chemical, structural and optical properties.

.

4.1.2.1. 9-fluorenone.

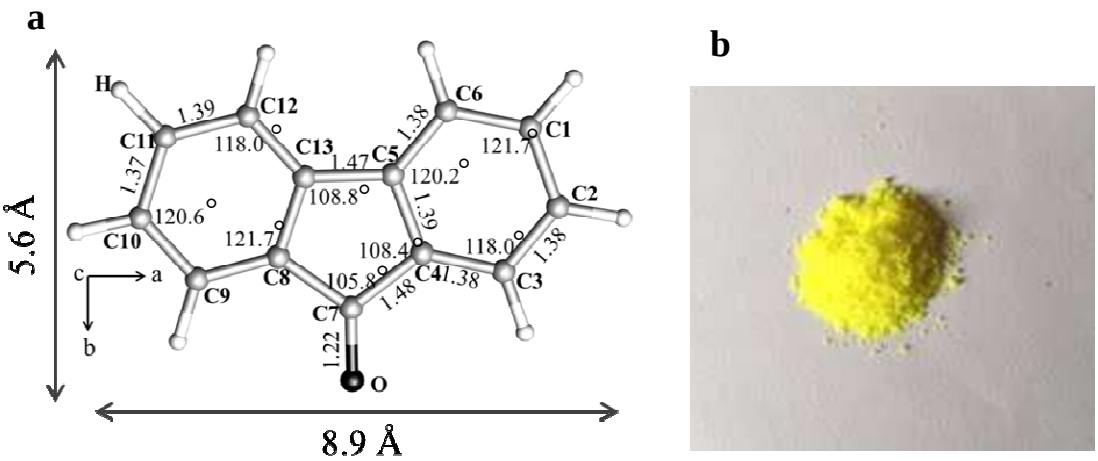

Figure 4.1.2.1. a) Molecular structure (in light grey, C atoms; in black O atom and in white H atoms, dimensions, bonds lengths and angles of 9-fluorenone, b) 9-fluorenone powder

9-fluorenone [1] ($C_{13}H_8O$) belongs to a group of molecules possessing intriguing spectroscopic and photophysical properties [2–5]. Its color originates from the low-lying electronic states, influenced by the bridge joining the carbonyl group (--C=O), which introduces a certain compactness of a closed structure to the molecule skeleton.

From figure 4.1.2.1 it is clear that the fluorenone molecular length, 8.9 Å along its longest axis, is greater than the ZL cell dimension along the channel (7.52 Å) and is however noticeably shorter than the maximum channel opening (~12 Å), indicating that this dye could have orientation freedom inside the zeolite. Experimental and theoretical studies showed the ability of FL in forming stable composites with zeolite L and demonstrated the influence of its orientation and of the water molecules present in the channels on the light harvesting properties. A first model of the host–guest interactions in the system ZL/FL obtained by experimental data is reported in [6]. On the basis of the results obtained by FTIR, Raman spectroscopy, thermal analyses and fluorescence spectroscopy, the authors suggested that a maximum of 1.1 FL molecules can be hosted in ZL channels. They located the dye close to the channel walls and justified the high stability in air conditions of ZL/FL composite on the basis of two molecule-framework interactions: 1) FL carbonyl group with an Al^{3+} of the zeolite framework and 2) FL aromatic ring with K^{+}. On the contrary, a further paper based on first principle molecular dynamics simulations [7] established, that the stability of the ZL/FL material, both in dehydrated and hydrated forms, is due to the strong interaction between the oxygen of the carbonyl group with the extraframework potassium cation.

Recently Zhou et all [8] reported the comparison between the simulated and measured UV-Vis absorption spectra of fluorenone both in hydrated and dehydrated zeolite L. The authors confirmed the K---O=C motif and stated that the shape of the absorption spectra is affected by the fluorenone's orientation, which is in turn strongly affected by the presence of water, although the interactions between the fluorenone and water molecules are negligible.

For this thesis the dye - purchased as analytical standards by Sigma-Aldrich with a purity of 98.0% - was used without further purification.

In Figure 4.1.2.2 is reported the TGA of crystalline fluorenone. The dye exhibits only one sharp weight loss at 220°C and the mass spectrometry (MSEGA) reveals that FL does not decompose in sub-moieties, but is released in its molecular form.

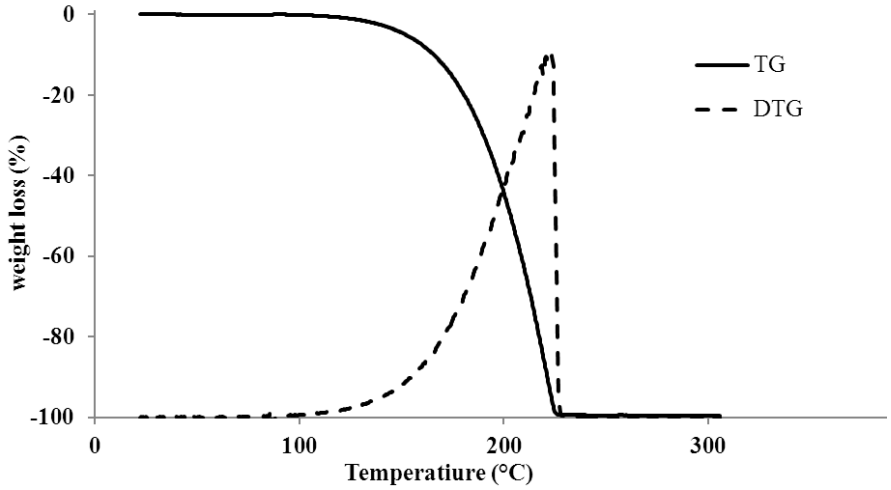

Figure 4.1.2.2. TG (continuous line) and DTG (dashed line) curves of crystalline 9-fluorenone.

An XRPD pattern (Figure 4.1.2.3) of the 9-fluorenone was collected to verify the purity and the crystallinity of the compound

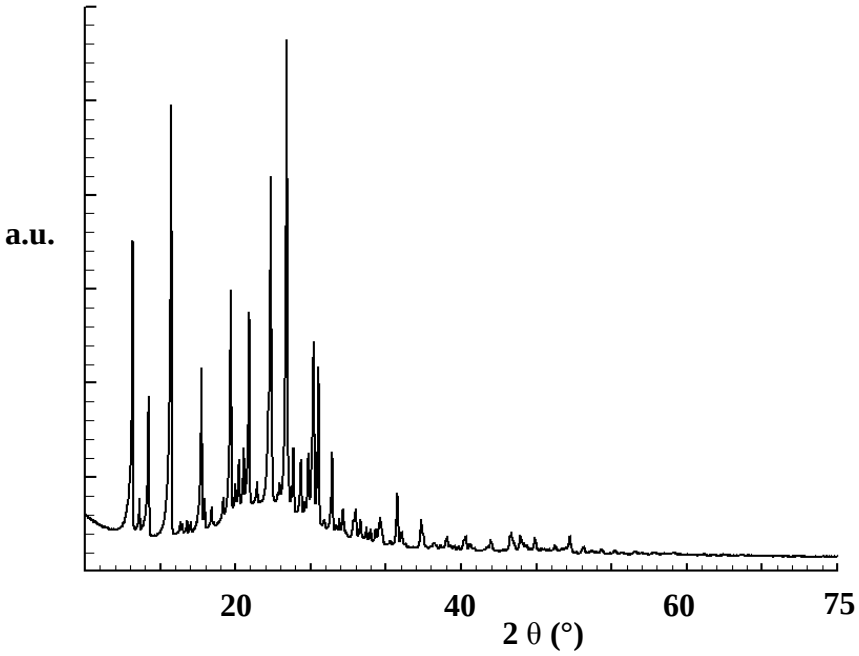

Figure 4.1.2.3. XRPD pattern of crystalline 9-fluorenone collected in a quartz capillary

Figure 4.1.2.4 A and B display a comparable peak distribution of the UV –vis absorption and fluorescence spectra collected for this study and that reported in [6].

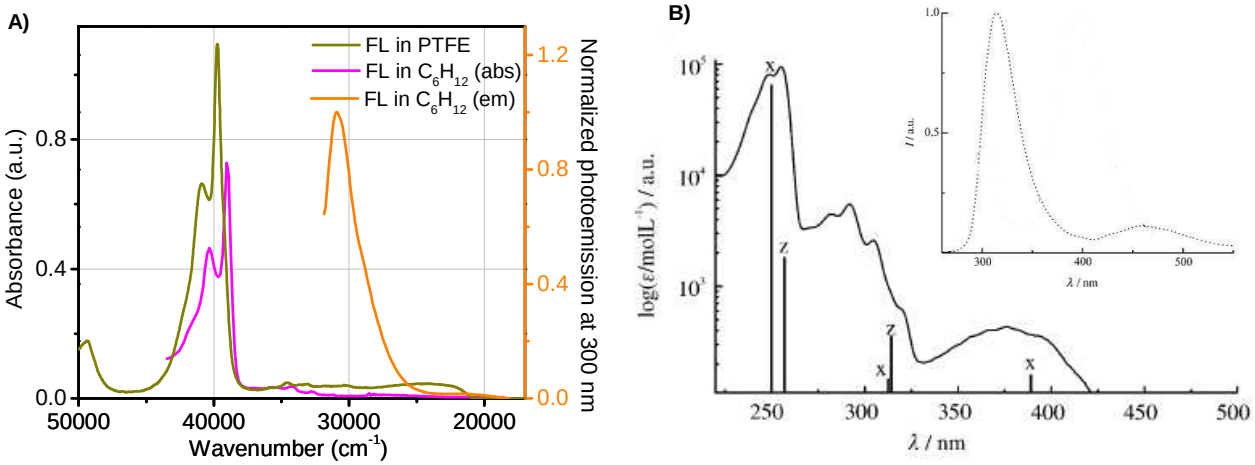

Figure 4.1.2.4 A) UV-vis absorption spectra of FL in cyclohexane solution (10^{-6} M, magenta line) and diluted in teflon (1:60 weight ratio, green line). The emission spectrum of FL in cyclohexane solution is also reported (orange curve); B) absorption and emission spectra (inset) of FL in cyclohexane solution as reported in [6].

4.1.2.2. tB-DXP

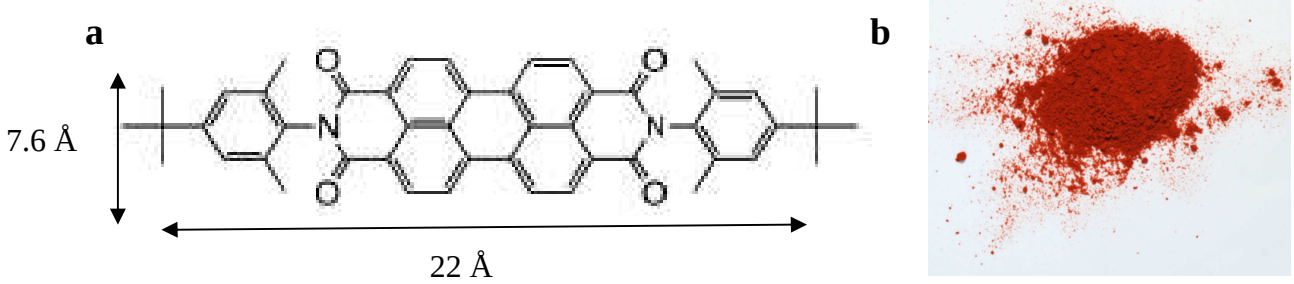

Figure 4.1.2.2.1. a) Molecular Structure dimensions of tB-DXP; b) tB-DXP powder

N,N′-bis(4-tert-butyl-2,6-dimethylphenyl)-3,4,9,10-perylenetetracarboxylicdiimide ($C_{48}H_{42}N_2O_4$), named tB-DX, is a neutral dye molecule, belonging to the perylene family (Fig. 4.1.2.2.1).

Perylene dyes and their derivatives are promising compounds for their intense visible light absorption, high stability, electron accepting ability, and unity quantum yields [9]. Due to

these properties, these are actually studied for optoelectronic and photovoltaic devices, energy-transfer cascades, light-emitting diodes, and near-infrared-absorbing systems

tB-DXP, in particular, was recently synthesized [10] according to newly developed procedures based on previously published works [11], in the laboratory of the Department of Chemistry at the University of Fribourg.

Given its large size tB-DXP belongs to the third group of guest molecules as described in chapter 2.3. For this reason it is expected that it aligns parallel to the *c* axis of ZL and that the formation of aggregates is avoided for the geometric inability of the molecules to slide over each other.[12].

Moreover, the presence of substituents in the para positions, acting as spacers, leads to an increase of the minimum contact distances and hence to a decrease of the interaction with the neighbor molecule, that would entail to J-coupling when the dyes are densely packed inside the ZL channels.

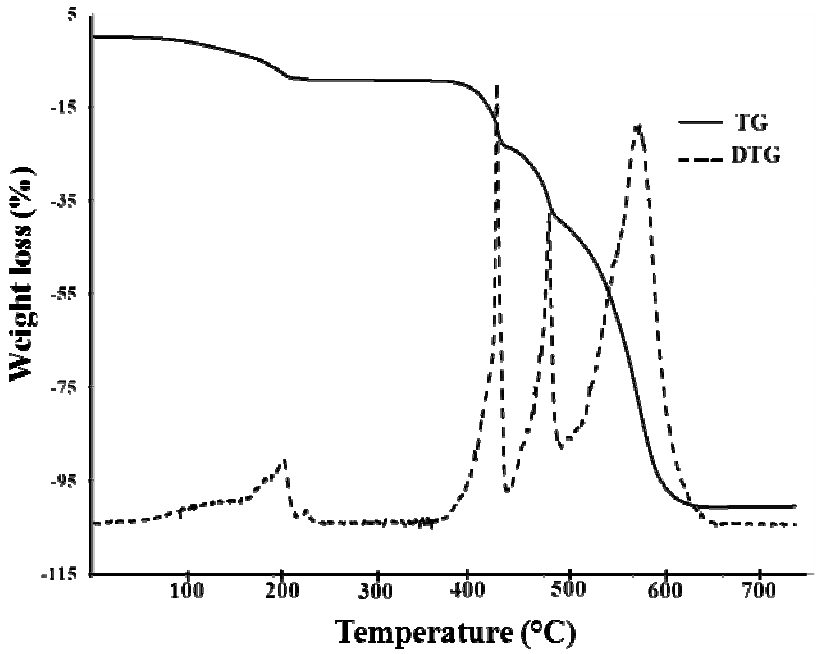

Figure 4.1.2.2.2. TG (continuous line) and DTG (dashed line) curves of crystalline tB-DXP.

In figure 4.1.2.2 is reported the TGA of crystalline tB-DXP. The dye exhibits four degradation steps at 170, 410, 480 and 570 °C and the mass spectrometry (MSEGA) reveals that tB-DXP decomposes in sub-moieties, such as CH_3CH_3 and CO_2(m/z 44-45).

A XRPD pattern (Fig. 4.1.2.2.3) of the tB-DXP was collected to verify the purity and the crystallinity of the compound.

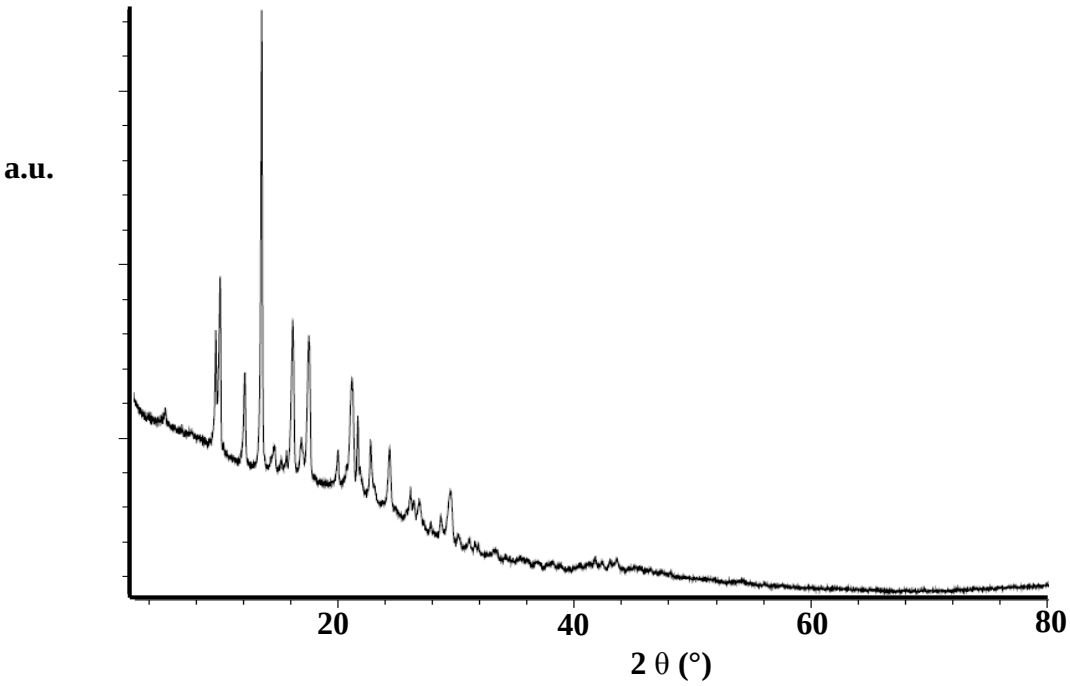

Figure 4.1.2.2.3 XRPD pattern of crystalline tB-DXP

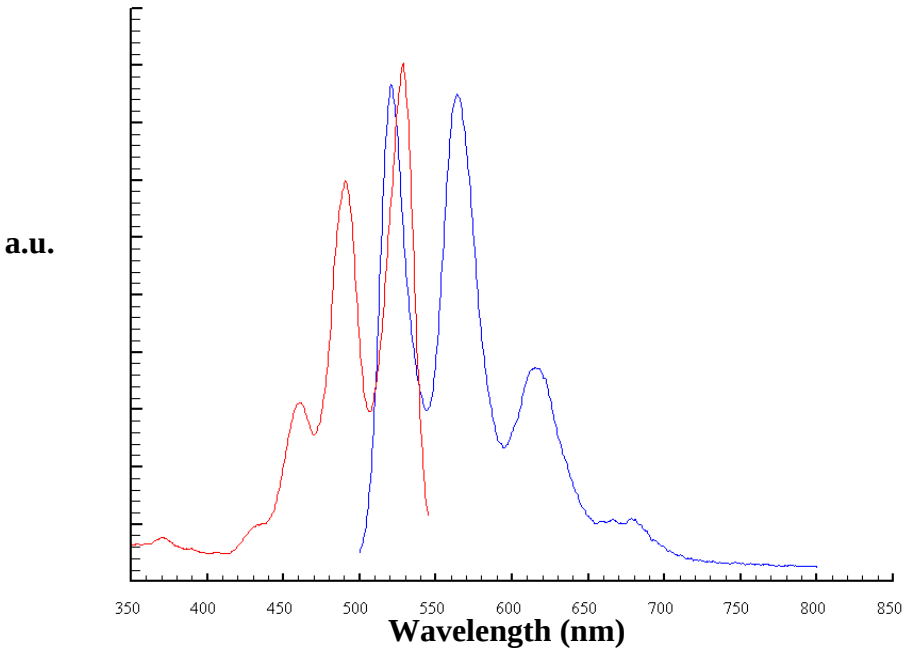

Figure 4.1.2.2.4 Superimposition of the absorption (red line) and florescence spectra (blue line) of the dye tB-DXP in dichloromethane solution

The absorption and fluorescence spectra of tB-DXP illustrated in figure 4.1.2.2.4 are identical to those of other studied in ref [10] and this is not surprising because all the dyes belonging to the perylene family are characterized by the same chromophoric core. Devaux at al. [10] reported also that the value of the luminescent quantum yield of the tB-DXP is close to one, making this dye a good candidate to be used as donor molecule in the antenna systems.

4.1.2.3. Thionine acetate salt

Thionine (3,7-Diamino-5-phenothiazinium acetate) ($C_{12}H_9N_3S \cdot C_2H_4O_2$) is a cationic and plane dye molecule, named Th hereafter.

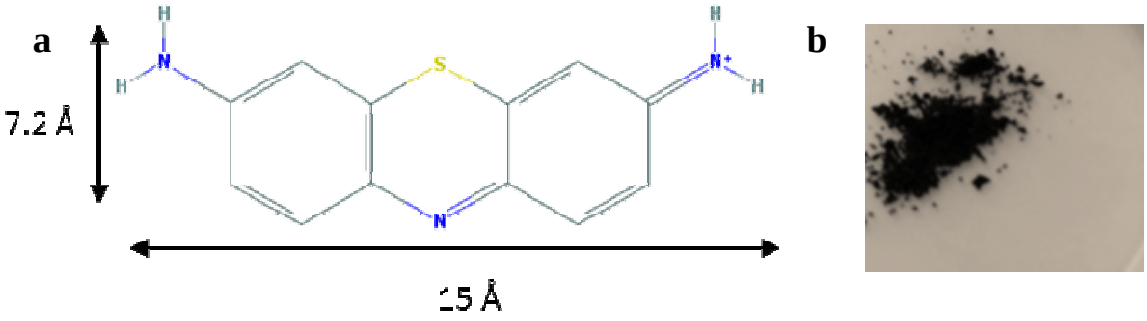

Figure 4.1.2.3.1. a) Molecular structure dimensions of thionine; b) thionine powder.

For this thesis the dye was purchased by Sigma-Aldrich with a purity of 98.0% and was used without further purification.

In figure 4.1.2.3.2. is reported the TGA of crystalline thionine acetate salt. The curve exhibits three steps at 65, 225 and a broad peak in the range of 320-575°C. The mass spectrometry (MSEGA) reveals that Th decomposes in sub-moieties, in particular CO_2(m/z=45) at 225°C and CO_2(m/z=44), NO_2, C_4H_4, N_2O_3, SO_2 and CO_2(m/z=45) as third step (320-575°C).

The cationic thionine was chosen because ZL cannot accommodate thionine dimers such as H-aggregates due to space filling effect, so the composites show intense fluorescence within the zeolite channels [13]. Moreover Th contains a sulfur atom, a relatively heavy atom, that can be more easily located by X-ray diffraction study respect to other dye molecules consisting of only light atoms (C, N and O), more difficult to localize in the zeolite framework.

A single crystal X-ray study of Th incorporated into a mordenite –Na [14] reported strong host-guest interactions through short C-O, N-O and S-O distances favored by a slight tilted arrangement of the molecule inside the 12 member ring of the mordenite.

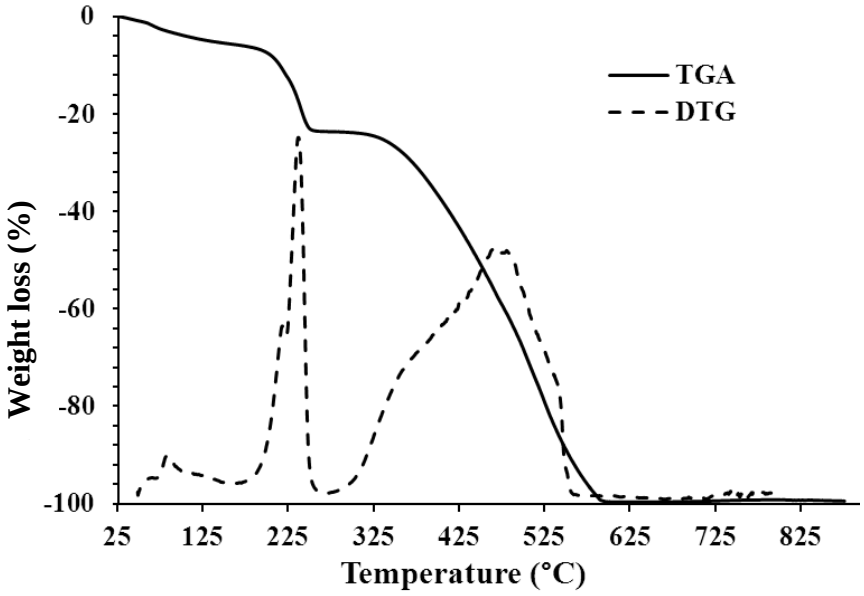

Figure 4.1.2.3.2. TG (continuous line) and DTG (dashed line) curves of crystalline thionine acetate salt.

Also for the pure Th compound was collected an XRPD pattern to verify the purity and the crystallinity of the compound (Figure 4.1.2.3.3).

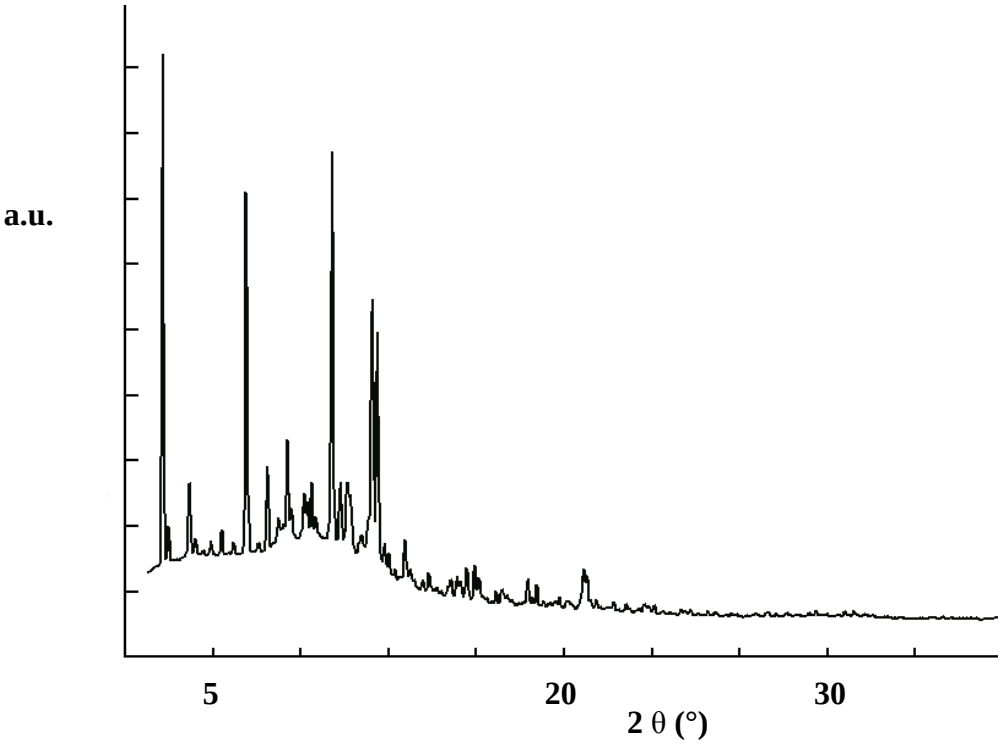

Figure 4.1.2.3.3 XRPD pattern of crystalline thionine collected in quartz capillary

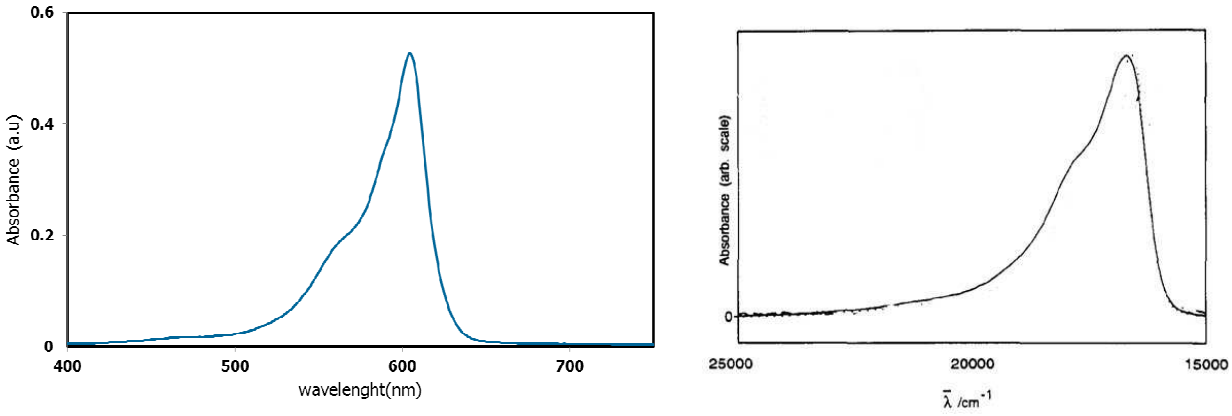

Figure 4.1.2.3.4 A) UV-vis absorption spectra of Th in ethanol solution and B) absorption spectra of Th in ethanol as reported in [15].

The absorption spectra of Th in ethanol solution performed for this study as illustrated in figure 4.1.2.3.4 a, is identical to that of ref [15].

References

[1] Luss H. R. and Smith D.L., (1972) *Acta Cryst*., B28, 884-889

[2] Andrews L. J., Deroulede A., and Linschitz H. (1978) *J. Phys. Chem*., 82, 2304–2309

[3] Arathi Rani S., Sobhanadri J., and Prasada Rao T. A. (1996) *J. Photochem. Photobiol. A. Chem*. 94, 1–5

[4] Kabayashi T. and Nagakura S. (1976) *Chem. Phys. Lett*. 43, 429–434

[5] Murphy R. S., Moorlag C. P., Green W. H., and Bohne C. (1997) *J. Photochem. Photobiol. A Chem*. 110, 123–129

[6] Devaux A., Minkowski C., and Calzaferri G. (2004) *Chem. Eur. J.*,10, 2391-2408

[7] Fois, E.; Tabacchi, G.; Calzaferri, G. J. (2010) *Phys. Chem. C*, 114, 10572 – 10579

[8] Zhou X., Wesolowski T. A., Tabacchi G., Fois E., Calzaferri G., Devaux A., (2013) *Phys. Chem. Chem. Phys*., 15, 159−167

[9] Huang C., Barlow S., Marder S. (2011), J. Org. Chem., 76, 2386–2407

[10] Devaux A., Calzaferri G., Miletto I, Cao P., Belser P., Brühwiler D., Khorev O., Häner R., Kunzmann A. (2013) *J. Phys. Chem. C*, 117, 23034-23047

[11] Rademacher, A.; Ma□rkle, S.; Langhals, H. Lo□sliche (1982) *Chem. Ber.*, 115, 2927−2934

[12] Busby M. , Devaux A., Blum C., Subramaniam V., Calzaferri G., and De Cola L. (2011) *Phys. Chem. C*, 115 (13), 5974–5988

[13] Ramamurthy V., Sanderson D.R., and Eaton D.F. (1993) *J. Am. Chem. Soc.*, 115, 10438-10439

[14] Simoncic P., Armbruster T. and Pattison P., (2004) *J. Phys. Chem. B*, 108, 17352-17360

[15] Calzaferri G., Gfeller N., (1992) *J. Phys. Chem.*, 96, 3428–3435

4.2 METHODS

A short overview of the experimental techniques (X-ray powder diffraction, thermal analyses, ATR-IR spectroscopy, computational modeling and UV/vis, photoluminescence spectroscopy) is presented in the Appendix II, III, IV, V and VI, respectively. In the following the experimental conditions of each technique adopted for this work are reported.

4.2.1. X-RAY POWDER DIFFRACTION

For this PhD thesis, both conventional and synchrotron sources have been used. In particular two different beamlines at the European Synchrotron Radiation Facilities (ESRF) (Grenoble, France) have been employed.

The temperature-resolved XRPD experiment on the sample ZL *som27* was performed at the GILDA beam line (BM08). The powder sample was loaded and packed in a 0.3 mm quartz capillary and heated in situ from RT up to 814°C by means of a gas blowing system. The heating rate was 5 °C/min. The capillary was mounted on a standard goniometric head and spun during data collection in parallel beam Debye–Scherrer geometry and a monochromatic wavelength of 0.6530 Å was used. The powder diffraction patterns were collected every 25 °C, on an image plate detector MAR345 positioned at 352 mm from the sample. LaB_6 was used as a standard to calibrate wavelength, sample to detector distance, and tilting angle of the detector. Al_2O_3 thermal expansion was used for temperature calibration.

To study the re-hydration process, an XRPD pattern was collected on a small quantity of zeolite L previously heated at 250 °C and left in air for about two months. This last pattern was collected at the Centro Interdipartimentale Grandi Strumenti (CIGS) of the University of Modena and Reggio Emilia, using a Panalytical X'Pert PRO diffractometer (θ/θ geometry, CuKα radiation) equipped with an X-celerator detector. A parabolic X-ray mirror was mounted on the incident beam to focus the beam on the sample. The powder was loaded in a glass capillary and spun under the X-ray beam. Data were collected in the 2θ range 3–120°, with steps of 0.02° and at 900 s per step speed. The fluorenone dye was also collected at the Centro Interdipartimentale Grandi Strumenti (CIGS) of the University of Modena and Reggio Emilia, in the 2θ range 3–80°, with steps of 0.03° and at 10 s per step speed.

The patterns of the dye tB-DXP was collected at the department of Chemistry at the University of Fribourg, using a STOE STADI P diffractometer (transmission geometry, CuK

alpha 1 radiation) equipped with an image plate detector. Data were collected in the 2θ range 3–80°, with steps of 0.03° and at 10 s per step speed.

All the composites (ZL/FL, ZL/tB-DXP and ZL/Th) and the thionine dye were collected at the SNBL1 (BM01a) beamline equipped with a PILATUS3 M-Series hybrid pixel detector (pixel dimension 172 μm). The powder was loaded and packed in a 0.3 mm boron capillary mounted on a standard goniometric head and spun during data collection in parallel beam Debye–Scherrer geometry with a monochromatic wavelength of 0.6825
In each experiment the one-dimensional diffraction patterns were obtained integrating the two-dimensional images with the program FIT2D [1].

4.2.2. THERMAL ANALYSIS/ TGA-MSEGA

In this work a Seiko SSC 5200 thermal analyzer equipped with a quadrupole mass spectrometer (ESS, Genesys Quadstar 422), was used, with the following experimental conditions: heating rate 10°C/min, temperature range RT - 900°C, 100 μL/min of air flux. The gas evolved analysis during the thermal reactions was carried out in Multiple Ion Detection mode (MID).

4.2.3. ATR-IR SPECTROSCOPY

The ATR-IR spectra on the powder samples were collected on a Bruker Vertex70 spectrophotometer, equipped with a diamond detector. Atmospheric carbon dioxide and moisture signals were subtracted to all the spectra by applying the atmospheric correction tools, as implemented in the Opus 6.5 software.

4.2.4. TRANSMISSION FT-IR

In this work, transmission FT-IR spectra were collected (at 2 cm^{-1} resolution) on a Vertex70 Bruker instrument. The self-supported sample wafer was placed inside a home-made quartz cell that allowed thermal activation, in-situ gas dosage and thermal treatments in a controlled atmosphere.

4.2.5. COMPUTATIONAL METHODS

Density functional theory (DFT) calculations were performed on the ZL/1.0FL and ZL/1.5FL ZL/FL composites. The PBE approximation [2] with periodic boundary conditions and Grimme corrections [3] for the FL-FL interactions was applied throughout. For both systems the simulation cell was twice the experimental unit cell of the ZL host along *c*. Calculations on the ZL/0.5FL composite (simulation cell stoichiometry: $K_{18}[Al_{18}Si_{54}O_{144}]\cdot FL$, with the PBE functional and periodic boundary conditions, were previously performed and thoroughly described in [4,5].

Electronic wavefunctions were expanded in planewaves up to a kinetic energy cutoff of 25 Ry (200 Ry for the density). Electron-ionic cores interactions were computed with ultrasoft Vanderbilt pseudopotentials for H, C, O, norm conserving pseudopotentials for Si, Al, K (semi-core in the case of K) [6-9]. All calculations were performed with the CPMD code [10], a particularly valuable approach in the study of quasi one-dimensional supramolecular systems inside zeolite nanochannels [11-14].

In order to establish which arrangements of FL molecules could be possible inside ZL channels, dry ZL/FL models were first considered. Local energy minima for the dry ZL/1.0FL and ZL/1.5FL models, characterized by simulation cell stoichiometry $K_{18}[Al_{18}Si_{54}O_{144}]\cdot 2FL$ and $K_{18}[Al_{18}Si_{54}O_{144}]\cdot 3FL$, respectively, were obtained by geometry optimization of different guess configurations. In all cases, the stabilization energy of the composites with respect to the isolated ZL and FL components was calculated with the formula:

$$\Delta E(\text{ZL}\cdot n\text{FL}) = E(\text{ZL}\cdot n\text{FL}) - E(\text{ZL}) - n\times E(\text{FL})$$

where E(ZL·nFL) is the energy of the optimized dry ZL/nFL model (n=2,3 for ZL/1.0FL and ZL/1.5FL, respectively), E(ZL) is the energy of the empty ZL, while E(FL) is the energy of an isolated FL molecule calculated in the same simulation cell.

In the case of the low FL-content system, *i.e.*, the ZL/0.5FL composite, an atomistic-level structural description is discussed in [4]. Stabilization energies of the hydrated ZL/1.5FL models with respect to the isolated components were calculated with the formula:

$$\Delta E(\text{ZL}\cdot 3\text{FL}\cdot x\text{H}_2\text{O}) = E(\text{ZL}\cdot 3\text{FL}\cdot x\text{H}_2\text{O}) - E(\text{ZL}) - 3\times E(\text{FL}) - x\times E(\text{H}_2\text{O})$$

where E(ZL·3FL·xH$_2$O) is the energy of the optimized hydrated ZL/1.5FL model (x=12,13,14), E(ZL) is the energies of the empty ZL, while E(FL) and E (H_2O) are

respectively the energies of an isolated FL molecule and an isolated water molecule calculated with the same simulation cell parameters. The relative stabilities of the systems with 12 and 14 water molecules with respect to that containing 13 H_2O's, were calculated with the formulas:

$$\Delta E(14/13) = E(\mathrm{ZL}\cdot 3\mathrm{FL}\cdot 14\mathrm{H_2O}) - [E(\mathrm{ZL}\cdot 3\mathrm{FL}\cdot 13\mathrm{H_2O}) + E(\mathrm{H_2O})]$$

$$\Delta E(12/13) = E(\mathrm{ZL}\cdot 3\mathrm{FL}\cdot 12\mathrm{H_2O}) - [E(\mathrm{ZL}\cdot 3\mathrm{FL}\cdot 13\mathrm{H_2O}) - E(\mathrm{H_2O})]).$$

4.2.6. OPTICAL SPECTROSCOPY: UV/Vis AND FLUORESCENCE

The ZL/FL composites absorption spectra were collected at the Nanostructured interfaces and surfaces laboratory of the University of Turin (NIS) in Diffuse Reflectance on a Cary5000 Varian spectrophotometer in the 2500-200 nm spectral range. All the samples were measured in the powder form inside a suprasil quartz cuvette having a width of 2 mm. The Fluorescence emission spectra were recorded also on the powder samples placed in a suprasil quartz cuvette (width of 2 mm) in reflection mode on a Horiba Jobin Yvon Fluorolog3 TCSPC spectro-fluorimeter equipped with a 450 W xenon lamp and a Hamamatsu R928 photomultiplier.
The spectra of the other dye-ZL samples (ZL/tB-DXP and ZL/Th) were collected using a different method experienced by the chemistry department of the University of Fribourg. This method consists in the preparation of the so called "oil glass sandwiches" (OGS) [15-17] All absorption spectra were recorded with a Lambda 25 spectrophotometer (Perkin-Elmer) with a slit width of 1 nm and a scan speed of 120 nm/min. Luminescence spectra were obtained on an LS50B (Perkin-Elmer) by using a slit width of 7.5 nm for oil−glass sandwiches. The scan speed in both cases was 120 nm/min. Both spectrometers were equipped with a custom-built sample holder for the solid-state samples (Fig. 4.2.6.1).

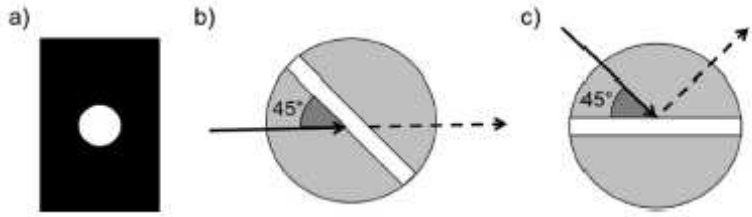

Figure 4.2.6.1. Working principle of custom-built sample holders used for the quantum yield determination of composite OGS. (a) Anodized black aluminum plate used as beam limiters. The OGS is placed between two such plates. (b) Sample holder used in the spectrophotometer. The gray disc represents the holder, the white bar is the slit into which the OGS-aluminum plate assembly is slid (held in place by Teflon screws), and the solid arrow indicates the incident light beam. (c) Sample holder used in the luminescence spectrometer (same legend as used for the previous holder [17].

The OGS was placed between two black anodized aluminum plates with the sample spot centered in the 6 mm hole. The whole assembly is then inserted into the sample holder slit and fixed by tightening two Teflon screws. The sample holder design ensures that the incident light beam hits the OGS at the same angle of 45° in both the absorption and luminescence spectrometer, thus ensuring a similar geometry in both measurements, which is crucial for relative quantum yield determinations. The anodized black aluminum plates serve as beam limiters and help in avoiding reflection effects from the glass plates.

References

[1] Hammersley A.P., Svensson S.O., Hanfland M., Fitch A.N., Häusermann D., (1996) *High Pressure Res.* 14 235–248

[2] Perdew, J. P., Burke, K., Ernzerhof, M. (1996) *Phys. Rev. Lett*., 77, 3865-3868

[3] Grimme, S. (2006) *J. Comput. Chem*., 27, 1787-1799

[4] Fois, E., Tabacchi, G., Calzaferri, G. (2010) *J. Phys. Chem. C*, 114, 10572 – 10579

[5] Zhou, X., Wesolowski, T. A., Tabacchi, G., Fois, E., Calzaferri,G., Devaux, A. (2013) *Phys. Chem. Chem. Phy*s., 15, 159−167

[6] Vanderbilt, D. (1990) *Phys. Rev. B*, 41, 7892-7895.

[7] Kleinman, L., Bylander, D.M. (1982) *Phys. Rev. Lett.*, 48, 1425-1428

[8] Hamman, D. R., Schlüter, M., Chiang, C. (1979) *Phys. Rev. Lett.*, 43, 1494−1497

[9] Troullier N., Martins, J. L. (1991) *Phys. Rev. B,* 43, 1993-2006

[10] CPMD code, MPI für Festkörperforschung: Stuttgart, Germany; IBM Zürich Research Laboratory: Zürich, Switzerland, 1990−2012, www.cpmd.org

[11] Fois, E., Tabacchi, G.; Quartieri, S.; Vezzalini, G. (1999) *J. Chem. Phys*., 111, 355-359

[12] Fois, E.; Gamba, A., Tabacchi, G., Quartieri, S., Vezzalini, G. (2001) *J. Phys. Chem. B*, 105, 3012-3016

[13] Fois, E., Gamba, A., Tabacchi, G., Quartieri, S., Vezzalini, G. (2001)*Phys. Chem. Chem. Phys*., 3, 4158-4163

[14] Fois, E., Gamba, A., Medici, C., Tabacchi, G. (2005) *ChemPhysChem*, 6, 1917-1922

[15] Calzaferri, G., Méallet-Renault, R., Bru□hwiler, D., Pansu, R., Dolamic, I., Dienel, T., Adler, P., Li, H., Kunzmann, A. (2011) *ChemPhysChe*m, 12, 580−594

[16] Fois, E., Tabacchi, G., Devaux, A., Belser, P., Bru□hwiler, D., Calzaferri, G. (2013) *Langmuir*, 29, 9188− 9198

[17] Devaux A., Calzaferri G., Miletto I., Cao P., Belser P., Bru□hwiler D., Khorev O., Ha□ner R., and Kunzmann A. (2013) *J. Phys. Chem. C* 117, 23034-23047

5. THERMAL BEHAVIOUR OF ZEOLITE L

The neutral chromophores, as above reported, can be inserted into the zeolite channels in gas phase and this procedure requires a preceding dehydration of the zeolite because the H_2O molecules block the molecule pathway. This implies that the thermal behavior of ZL has to be preliminary investigated. The study of the dehydration and re-hydration processes were carried out and the consequent structural modifications were studied by temperature resolved synchrotron X-ray powder diffraction**.**

5.1. STRUCTURAL REFINEMENT

Structural refinements were performed by full profile Rietveld analysis in the P6/mmm space group, starting from atomic coordinates reported for perlialite [1]. Since no evidence of symmetry change was found from the analysis of the powder patterns, the P6/mmm space group was used in all the structure refinements. A total of 20 patterns were fitted out of the 45 available, selected between RT and 707 °C. Notwithstanding the zeolite maintains a good crystallinity up to 814 °C (Fig. 5.1.1a, b) the diffraction data quality did not allow satisfactory structure refinement above 707 °C and only unit cell parameters were refined. The extracted Bragg peak profiles were modeled by a pseudo-Voight function with two refined coefficients (one Gaussian and one Lorentian term, Gw and Ly in GSAS terminology) and a 0.01% cut-off of the peak intensity. Due to high diffuse air scattering, the background was partially subtracted and then empirically fitted using a Chebyschev polynomial with 12 variable coefficients.

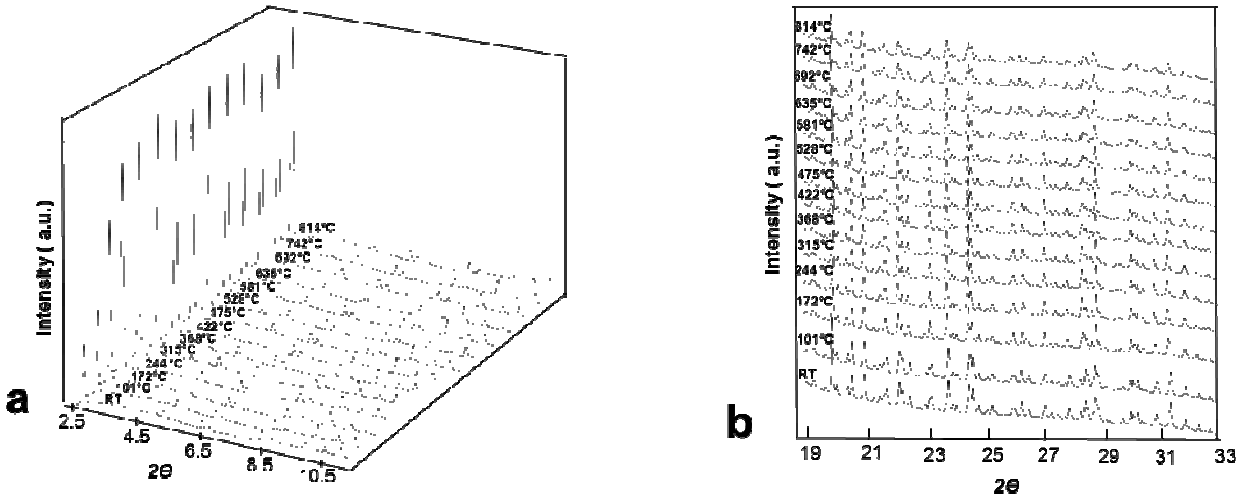

Figure 5.1.1 Selected powder patterns of zeolite L as a function of temperature reported in the 2theta ranges: (a) 2.5–10.5°; (b) 19–33°.

The 2θ-zero shift was preliminarily refined for all the collected patterns and then fixed at the mean value of the data set, since the variations were very low. The scale factor was allowed to vary for all histograms. In the final cycles, the refined structural parameters for each data histogram were the following: fractional coordinates for all atoms, occupancy factors for extra framework cations and water oxygen atoms, and thermal isotropic displacement factors. H-atoms were not considered during the structure refinement, due to their low scattering factors. Soft constraints were applied to the T–O bond distances and were gradually released after the initial stages of refinement. The thermal displacement parameters were constrained in the following way: the same value for all the tetrahedral atoms, a second value for all the framework oxygen atoms, and a third value for the water molecules. The thermal parameters of K sites were free of constraints. Occupancy factors and isotropic thermal displacement factors were varied in alternate refinement cycles. The Rietveld refinements of the powder patterns converged successfully up to 707 °C. The pattern of the re-hydrated phase was refined starting from the structural model obtained from the data collected at RT, by adopting the above described refinement strategy, except for the number of instrumental background coefficients (25 instead of 12). Table 5.1.1. (Appendix A) summarizes the refinement details of four selected patterns, collected at RT, 101 °C, 244 °C, and 707 °C. The refined cell parameters are reported in Table 5.1.2. (Appendix A) for each temperature value. The refined atomic coordinates, occupancy factors and thermal parameters for the corresponding

structures at the four temperatures are reported in Table 5.1.3 (Appendix A) and the bond distances in Table 5.1.4. (Appendix A). Figure 5.1.2. shows the observed and calculated profiles and the difference curves for the selected patterns.

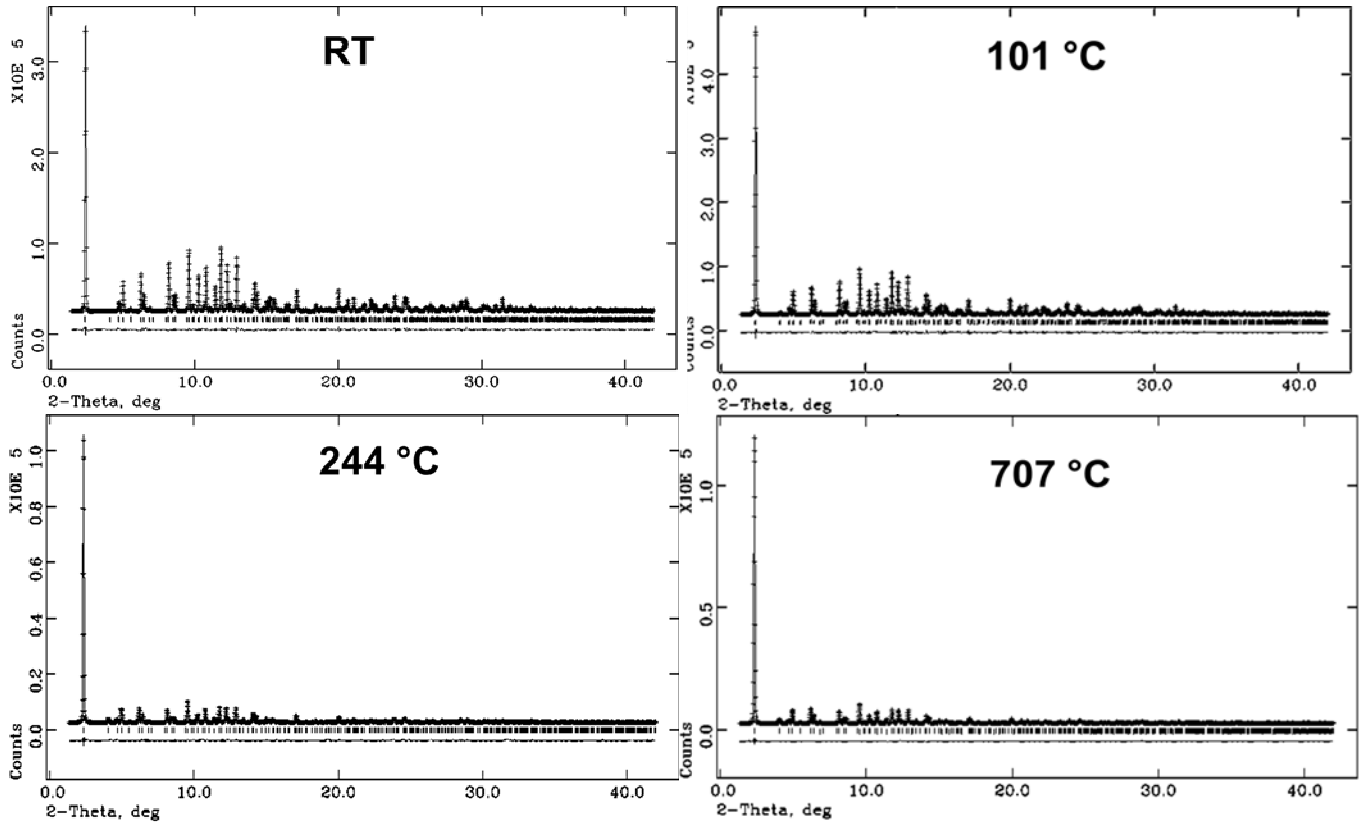

Figure 5.1.2. Observed (crossed line) and calculated (continuous line) diffraction patterns and final difference curve from Rietveld refinements of zeolite L at RT, 101°, 244° and 707 °C.

5.2. RESULTS

In the investigated temperature range, the cell parameter variations – although very small – are rather discontinuous (Table 5.1.2., Appendix A). In the initial heating stage (below 101 °C) zeolite L is essentially rigid, the a parameter decreasing and the *c* parameter increasing by less than 0.1% (Figure. 5.2.1). Between 101° and 244 °C, *a* increases by 0.33%, *c* decreases by 0.2% and the cell volume undergoes the largest increment observed in the whole investigated T range, i.e. 0.44%. Above 244 °C, the variation trend of a and c parameters inverts and the V–T curve flattens, though displaying a further slight cell volume increase.

The total variations of the *a*, *c*, and *V* parameters are 0.2%, 0.3% and 0.7%, respectively. ZL is stable up to 814 °C and no structural breakdown is observed.

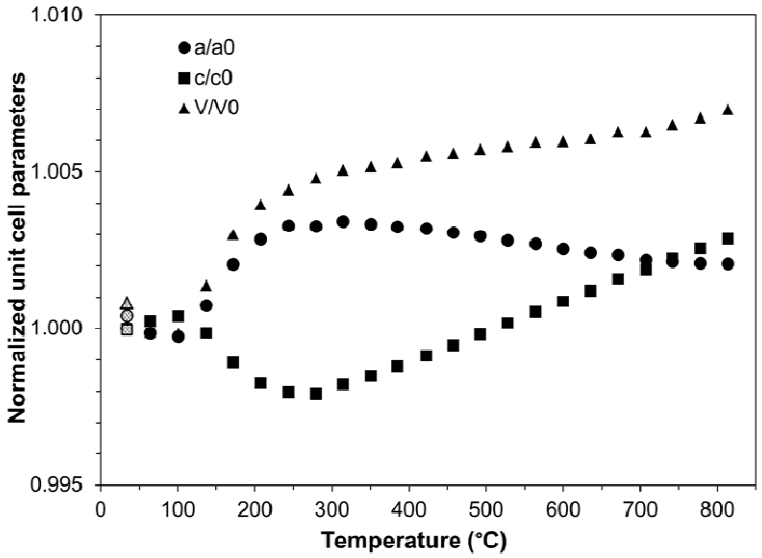

Figure 5.2.1. Normalized unit cell parameters vs. temperature. The grating symbols correspond to the rehydrated phase.

5.2.1. Framework

During dehydration we observed the following modifications in the zeolite L framework:
(i) the main 12MR channel, parallel to the *c* axis, becomes more circular upon heating, as a consequence of the increase and decrease in O1–O2–O1 and O2–O1–O2 angles, respectively (Figs. 5.2.1.1. a). The free diameters [2] of the 12MR (O1–O1 and O2–O2) change from 7.2 Å and 7.6 Å at RT, to 7.5 and 7.7 Å at 707 °C, respectively (Figure 5.2.1.1. b); (ii) the 8MR channel, parallel to the c axis, becomes more circular as a consequence of the decrease and increase of free diameters O1–O1 and O5–O5, respectively (Figures. 5.2.1.2); (iii) during water release, between 101° and 244 °C, the 8MR apertures surrounding the main 12MR channel become more circular, with a decrease in the free diameter O1–O1 (corresponding to the c axis trend) and an increase in the O6–O6 one. In contrast, after complete dehydration, above 244 °C, the trend inverts and the rings become more elliptic (Fig. 5.2.1.3); (iv) the T2-O6-T2 angle of the D6R decreases constantly upon heating (Figures. 5.2.1.4) via tetrahedral rotation. Also the O4–O4 distance (Figure 5.2.1.5), which can be assumed as the D6R

thickness, tends to decrease (even if not in a monotonic way). Moreover, the O3–O5–O3 and O5–O3–O5 angles (Figure 5.2.1.6) increase and decrease, respectively, becoming more similar to each other and hence reducing the di-trigonal distortion of the 6-membered ring.

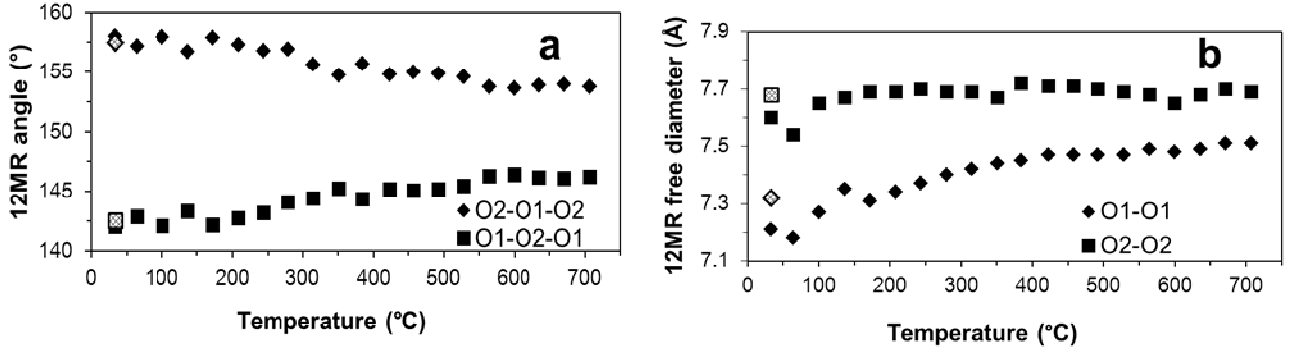

Figure 5.2.1.1. Temperature-induced shape change of the12MR delimiting the main channel parallel to c axis: (a) O2–O1–O2 and O1–O2–O1 angles; (b) O1–O1 and O2–O2 free diameters (calculated assuming an oxygen radius of 1.35 Å). The grating symbols correspond to the rehydrated phase.

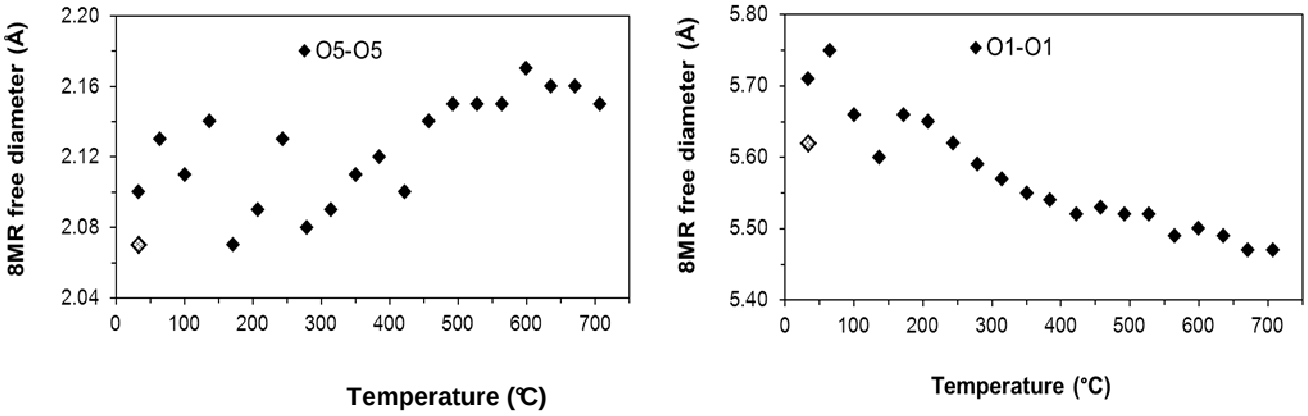

Figure 5.2.1.2. Temperature-induced shape change of the 8MR delimiting the corresponding channel parallel to c axis: O1–O1 and O5–O5 free diameters (calculated assuming an oxygen radius of 1.35 Å). The grating symbols correspond to the rehydrated phase.

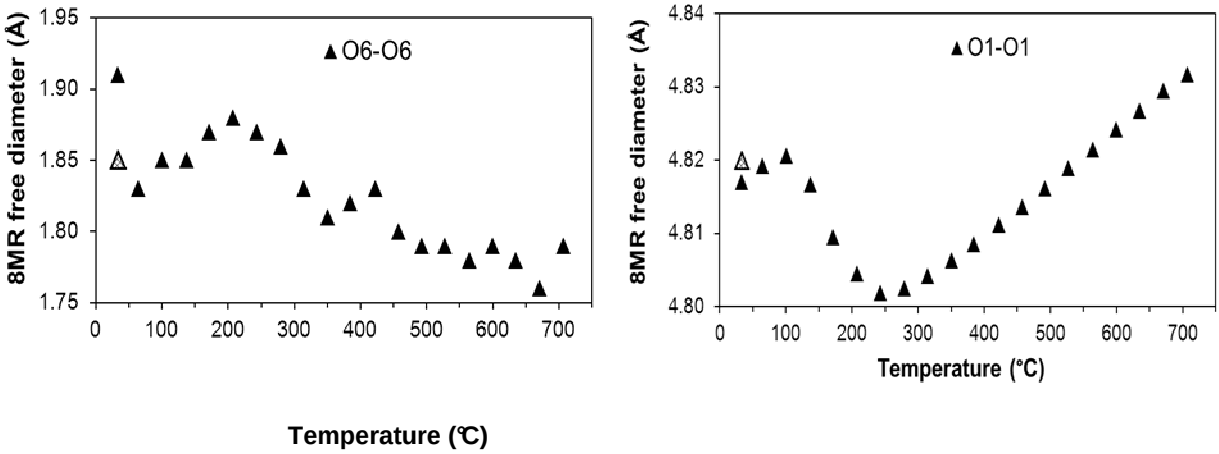

Figure 5.2.1.3. Temperature-induced shape change of the 8MR windows surrounding the 12MR channel: O1–O1 and O6–O6 free diameters (calculated assuming an oxygen radius of 1.35 Å). The grating symbols correspond to the rehydrated phase.

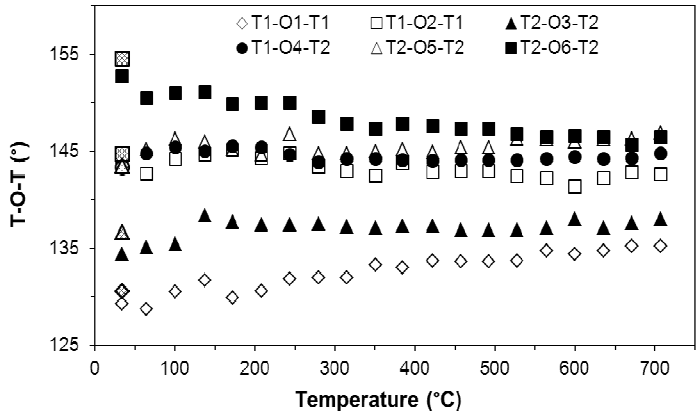

Figure. 5.2.1.4. Variation in T–O–T angles vs. temperature.
The grating symbols correspond to the rehydrated phase.

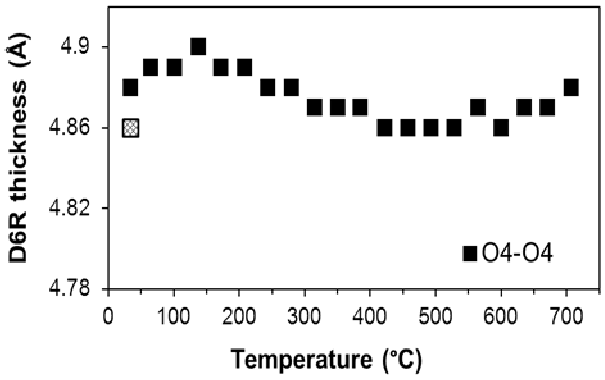

Figure 5.2.1.5. Thickness of the D6R (O4–O4 distance) as a function of temperature.

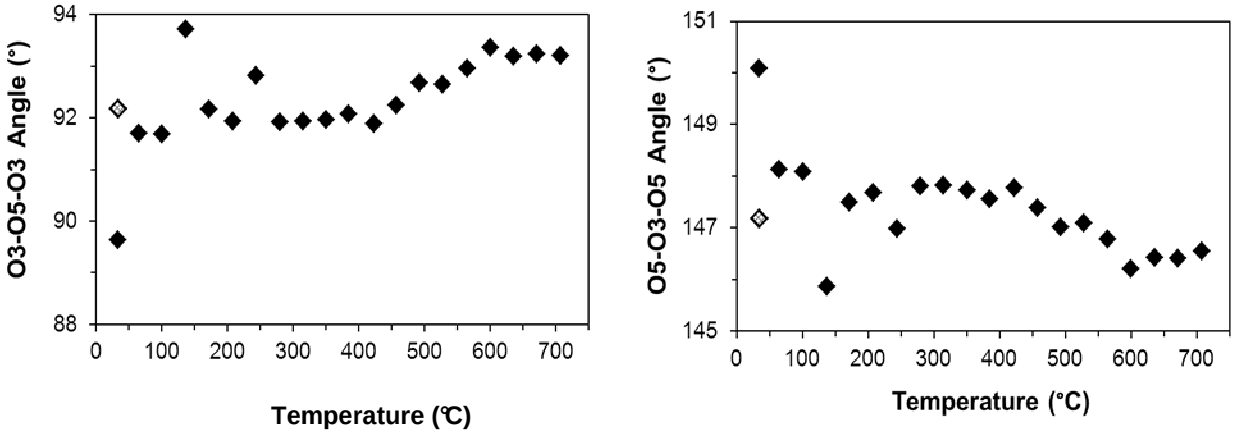

Figure 5.2.1.6. Variation of the O3–O5–O3 and O5–O3–O5 angles of the 6-rings of the D6R vs. temperature. The grating symbols correspond to the rehydrated phase.

5.2.2. Extraframework sites

The occupancy factors (Table 5.1.3. Appendix A) and the coordination distances (Table 5.1.4 in Appendix A) of the potassium sites (**KB, KC** and **KD**) at RT well agree with the results of the original structural resolution. The slight discrepancies can be explained by the different cation content in BV (6 K and 3 Na a.f.u) and in the present sample (8.46 K a.f.u).

Upon heating, KD slightly shifts from its original position (Table 5.1.3. in Appendix A) and the potassium distribution on KC and KD sites undergoes a slight reassessment (Fig. 5.2.2.1). The KB site maintains the same occupancy factor in all the studied T range, while the occupancy of KD and KC sites decreases and increases, respectively, indicating a partial migration of potassium from the main channel to the inner KC site. This migration – induced by the necessity of KD to restore its coordination requirements after the loss of the previously coordinated water molecules – ends when the KC site is full. The further decrease in the occupancy of KD – between 244° and 707 °C – can be ascribed to the presence of some water in KD, which is lost above 244 °C. The main T-induced variations in the bond distances between extraframework cations and framework oxygen atoms (Table 5.1.4. Appendix A) are summarized as follows:

- KB-O3 distance increases as a consequence of the 6-ring deformation;
- KC-O5 distance increases, related to the increase of the O5–O5 diameter of the 8MR perpendicular to the c axis;

- KD-O4 and KD-O6 bonds shorten during water loss (100–244 °C). This induces a shift of O6 inside the main 12MR channel and a decrease in the T2-O6-T2 angle (Fig. 5.2.1.4). Moreover the O4–O4 distance decreases (Fig. 5.2.1.5) determining a decrease in the D6R thickness.

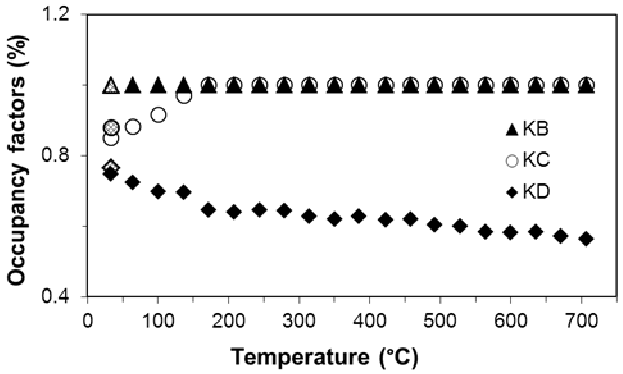

Figure 5.2.2.1. Plot of K sites occupancy factors vs. temperature. The grating symbols correspond to the rehydrated phase.

As already said the *som27* contains at RT 18 water molecules, distributed over five partially occupied sites (**WF, WH, WI, WJ, WK**). They were located in the main channel, but with slightly different coordinates relative to BV. Figure 5.2.2.2. shows the clusters of water molecules and cation-water layers, which develop along the *c* axis. This hydrogen-bonds system is similar to that observed by Lee et al. in their Rb-GaSi L sample [3].

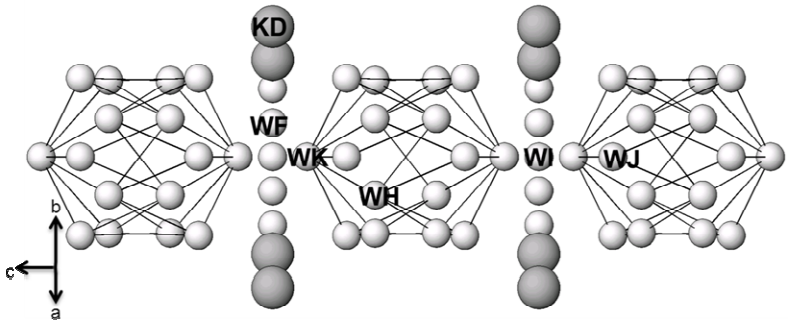

Figure 5.2.2.2. Sequence of water clusters and cation-water layers running along the *c* axis inside the 12MR channel. The distances W–W between 2.65 and 2.89 (Å) are drawn. Light grey: water sites; dark grey: KD site.

In Figures 5.2.2.3 a and b the variations of the water site occupancy factors and the total number of water molecules in the unit cell are shown as a function of temperature. Most of the water molecules are released above 101 °C, and at 244 °C the zeolite is completely dehydrated.

In particular:

- water **WI** – the most occupied site and the only water molecule bonded to potassium KD – is the last to be completely removed;
- water **WF** – initially not bonded either to the framework or to the cations – upon heating moves closer to **KD** and, as a consequence, it is one of the last water molecules to be released;
- water **WH** – initially coordinated to the oxygen atom O1 – drifts away during dehydration (Table 5.1.4. in Appendix A), hence allowing the relaxation of the 12MR aperture along the O1–O1 direction (Fig. 5.2.1.1. b);
- water **WJ**, on the contrary, moves closer to the framework oxygen O2 (Table 5.1.3, Appendix A) and its release is slower compared to WH. This could explain the almost constant value of the O2–O2 diameter of the 12MR aperture (Fig. 5.2.1.1. b);
- water **WK** – bonded only to other water sites – is the freest water molecule and its release begins already at 65 °C.

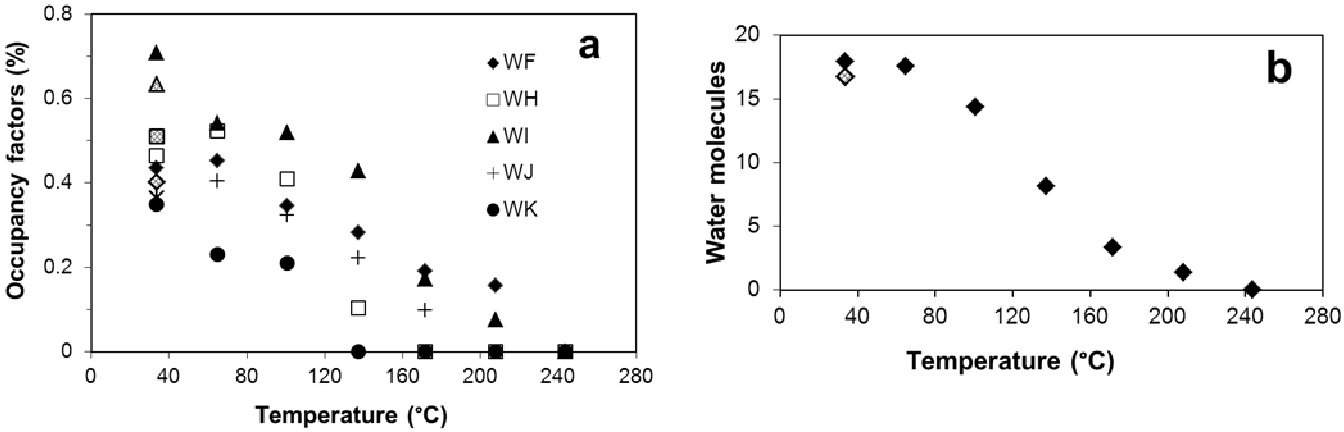

Figure 5.2.2.3. Occupancy factors of water sites in ZL (a) and total water content per unit cell (b) *vs*. temperature. The grating symbols correspond to the rehydrated phase.

The total number of water molecules – as calculated from the refined occupancies of all W sites (Table 5.1.3 in Appendix A and Fig. 5.2.2.3b) – agrees well with the results of the

thermal analyses (Figure. 5.2.2.4). On the contrary, the temperature corresponding to complete water loss shown by the DTG curve (about 230 °C) is slightly lower than that of the in situ XRPD experiment (244 °C). This effect can be reasonably explained by the different experimental set up adopted in the two measurements (powdered sample in a small platinum boat in the TG analysis and in a glass capillary in the XRPD experiment).

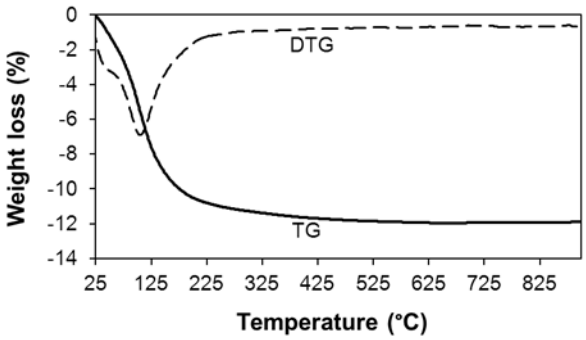

Figure 5.2.2.4. TG (continuous line) and DTG (dashed line) curves of ZL *som27*.

5.2.3. Re-hydration process

To study the re-hydration process, an XRPD pattern was collected on a small quantity of *som27* previously heated at 250 °C and left in air for about two months. The structural features of the rehydrated phase can be summarized as follows:

– the cell parameters are almost perfectly recovered (Table 5.1.2. in Appendix A and Fig. 5.2.1.);

– the original framework structure of the hydrated phase is almost completely regained (Figs. 5.2.1.1–5.2.1.6 and 5.2.3.1) although a slight hysteresis is observed;

– potassium cations regain the original distribution on KC and KD (Fig. 5.2.2.1.);

– WF and WJ sites do not return exactly to the original positions and, more importantly, the original water content is not completely regained (upon rehydration only 16.7 water molecules are found instead of the original 18). In particular, compared to the original zeolite L, the WK site is empty, WF and WI and WJ show a lower occupancy, while WH is slightly more occupied (Figs. 5.2.2.3 a and b).

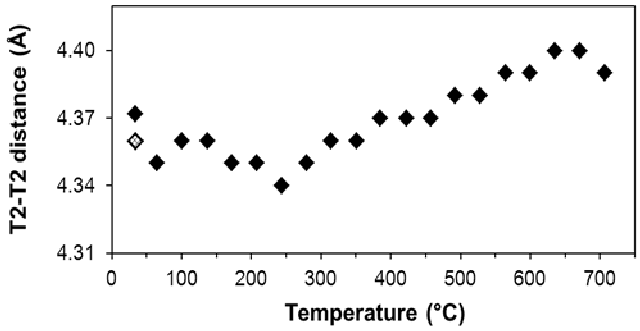

Figure 5.2.3.1. Variation of cancrinite cage thickness (T2–T2) *vs.* temperature. The grating symbols correspond to the rehydrated phase.

5.3. DISCUSSION AND CONCLUSIONS

On the basis of the results reported above, the thermal behavior of zeolite L can be summarized using three different steps, corresponding to the following temperature ranges:

1) Below 100 °C: the structure is essentially unmodified. The cell parameters do not change, dehydration is very limited and involves only the WK and WI site (whose occupancy factors start to decrease), and potassium starts to move from the KD to KC site. This last structural change could be induced by the initial removal and successive complete loss of the WI water molecule, initially coordinated to the KD site;
2) Between 101 and 244 °C: complete dehydration of the sample occurs, although without inducing notable structural deformations. The 6-membered rings become less di-trigonal and the 12MR apertures become more circular. These last deformations allow easier water diffusion and release and induce an increase of the a cell parameter. Moreover, the 8MR channel aperture perpendicular to the c axis also becomes more circular. The a axis increase is accompanied by a c parameter decrease, related to the more circular shape assumed by the 8MR windows which surround the 12MR channel. The driving force of this contraction can be recognized in the attraction of KD to O4. Overall, a small, even if rapid, cell volume increase is observed. The shift of potassium from KD toward KC continues up to 200 °C;
3) Above 244 °C: zeolite L is completely dehydrated. After complete water release, the a and c cell parameters invert their trends and undergo a decrease and increase of about 0.03 Å, respectively. As a whole a steady volume increase is observed (Table 5.1.2. in

Appendix A and Fig. 5.2.1). The relaxation of the framework along c could be favored by the loss of the WH and WJ water molecules, originally bonded to O1 and O2, and reflected in an increase in the cancrinite cage thickness (see T2–T2 distances in Fig. 5.2.3.1).

As reported above, the structure of potassium zeolite L dehydrated in vacuum at 400 °C was studied by neutron powder diffraction [4], obtaining results rather different from those obtained in the present study. In particular, upon dehydration, the following unit cell parameter variations were observed: +0.4%, -0.8% and -0.03% for *a*, *c* and *V*, respectively. If these data are compared with those obtained for the present sample heated at 422 °C (+0.3%, -0.1% and +0.5%) it is noted that the limited *c* contraction in the present sample is reflected in an overall volume increase.

This different behavior can be explained by the following factors which differentiate the two dehydration experiments:

– Newsam's sample ($K_9Al_9Si_{27}O_{72}$·17 H_2O) is richer in Al and K and poorer in water compared to the present sample. Moreover, the structure refinement showed that potassium is distributed over a different number of extraframework sites;

– The experiment performed by Newsam [4] was conducted with a different kinetics, heating the sample in vacuum very slowly (in several hours) compared to the conditions of our experiment (5 °/min) and maintaining it in vacuum at 400 °C for 16 h.

The second factor seems to be the crucial one. In fact, as already observed in literature [25], the kinetic conditions play a primary role in the dehydration process of zeolites. In particular, the different kinetics induces a different evolution of the extraframework system (both water molecules and extraframework cations) with a consequent influence on the deformation of the framework.

In general, after Cruciani [5], most zeolites exhibit a so called negative thermal expansion, while a positive one is observed in a number of neutral siliceous zeolites, like CIT-5, AlPO4-31 and the one-dimensional 12MR system ITQ-4 [6] In these materials expansion is mainly realized along the direction of the main large 12- or 14-ring channel, as observed in the ZL *som27*.

The SI index [5] of *som27* is equal to 5. This result is particular noteworthy due to the rather low Si/Al ratio (3.3) of this zeolite, which would suggest a lower thermal stability.

Finally, the inverse relationship between thermal stability and ionic potential of the extraframework ions – potassium in the present sample – was confirmed by the results of this study. Usually, in zeolites, most of the extraframework cations are coordinated by water molecules. Upon dehydration these cations move closer to the framework to form new bonds. This can induce strains on the framework, resulting in a structural deformation or even bond breaking. The ZL *som27* represents an exception, because only one of the three cation sites (KD) is bonded to a water molecule, while the coordination spheres of the other cations are formed only by framework oxygen atoms. Moreover, among the five water molecules, only two are at coordination distance from the framework oxygen atoms, while the others are only involved in water–water hydrogen bonds. These structural features explain why the dehydration process does not induce substantial structural modifications in the host framework and why zeolite L even undergoes a small unit cell volume increase upon heating.

The results show that ZL has a very high thermal stability and maintains a good crystallinity up to 814 °C. Following Baur [7], this framework can be classified as inflexible upon changes in both physical and chemical conditions. In particular, concerning the response to heating under the experimental conditions adopted in the present study, it is noteworthy that zeolite L undergoes a slight thermal expansion, which is a very unusual behavior for an alumino-silicate microporous material.

APPENDIX A

Table 5.1.1. Experimental and refinement parameters for zeolite L at RT, 101 °C, 244 °C, and 707 °C.

T (°C)	RT	101	244	707
Space Group	P6/m m m	P6/m m m	P6/m m m	P6/m m m
a (Å)	18.3367(2)	18.3320(1)	18.3968(2)	18.3769(1)
c (Å)	7.5176(1)	7.5205(1)	7.5019(1)	7.5317(1)
V (Å^3)	2189.06(5)	2188.66(4)	2198.72(4)	2202.79(4)
R_p (%)	1.4	1.3	1.1	1.1
R_{wp} (%)	1.9	1.9	1.6	1.6
R F2 (%)**	8	7.46	6.75	9.7
X^2	10.5	10.3	0.80	0.78
No. of variables	55	55	42	42
No. of observations	2889	2889	2889	2889
No. of reflections	673	673	673	673

Table 5.1.2. Unit cell parameters of zeolite L as a function of temperature

T(°C)	a (Å)	c (Å)	V(Å^3)
RT	18.3367(1)	7.5176(1)	2189.06(4)
65	18.3338(2)	7.5194(1)	2188.78(5)
101	18.3320(1)	7.5206(1)	2188.66(4)
137	18.3504(2)	7.5166(1)	2192.04(5)
172	18.3741(2)	7.5095(1)	2195.62(5)
208	18.3889(2)	7.5045(1)	2197.71(5)
244	18.3968(2)	7.5023(1)	2198.72(4)
280	18.3964(1)	7.5019(1)	2199.53(5)
315	18.3994(2)	7.5042(1)	2200.11(7)
351	18.3978(2)	7.5062(1)	2200.35(5)
385	18.3962(2)	7.5085(1)	2200.62(5)
422	18.3950(2)	7.5111(1)	2201.10(5)
458	18.3929(2)	7.5136(1)	2201.30(5)
492	18.3909(2)	7.5162(1)	2201.58(5)
528	18.3883(2)	7.5188(1)	2201.76(5)
565	18.3864(2)	7.5215(1)	2202.06(5)
600	18.3833(2)	7.5241(1)	2202.11(5)
635	18.3810(2)	7.5267(1)	2202.31(5)
671	18.3796(2)	7.5295(1)	2202.79(5)
707	18.3769(1)	7.5317(1)	2202.79(4)
742	18.3757(1)	7.5344(1)	2203.29(4)
778	18.3747(1)	7.5368(1)	2203.75(4)
814	18.3745(1)	7.5391(1)	2204.36(4)
RT(REV)	18.3445(2)	7.5174(1)	2190.85(5)

Table 5.13. Atomic coordinates, occupancy factors and thermal parameters for the structures at RT, 101°, 244°, and 707 °C.

Atom	x/a	y/b	z/c	Occ.	Uiso
		RT			
T1	0.0939(1)	0.3566(2)	0.5	1	0.0136(5)
T2	0.1646(2)	0.4978(1)	0.2093(2)	1	0.0136(5)
O1	0	0.2694(6)	0.5	1	0.0159(9)
O2	0.1616(2)	0.3233(5)	0.5	1	0.0159(9)
O3	0.2671(2)	0.5342(4)	0.2534(8)	1	0.0159(9)
O4	0.1019(3)	0.4127(3)	0.3241(5)	1	0.0159(9)
O5	0.4245(2)	0.8490(4)	0.2645(9)	1	0.0159(9)
O6	0.1452(4)	0.4762(4)	0	1	0.0159(9)
KB	0.3333	0.6666	0.5	1	0.022(7)
KC	0.5	0	0.5	0.850(5)	0.018(2)
KD	0.2989(3)	0	0	0.753(4)	0.084(2)
WF	0.111(1)	0	0	0.434(7)	0.138(8)
WH	0.1186(7)	0	0.384(1)	0.465(5)	0.138(8)
WI	0.2576(9)	0.1288(5)	0	0.70(1)	0.138(8)
WJ	0.165(1)	0.0830(7)	0.281(2)	0.399(5)	0.138(8)
WK	0	0	0.142(7)	0.35(1)	0.138(8)
		101 °C			
T1	0.0949(2)	0.3575(2)	0.5	1	0.015(6)
T2	0.1646(2)	0.4974(1)	0.2110(2)	1	0.015(6)
O1	0	0.2732(6	0.5	1	0.016(1)
O2	0.1630(2)	0.3261(5)	0.5	1	0.016(1)
O3	0.2655(2)	0.531114)	0.2586(9)	1	0.016(1)
O4	0.1026(3)	0.4145(3)	0.3233(5)	1	0.016(1)
O5	0.4241(2)	0.8483(4)	0.268(1)	1	0.016(1)
O6	0.1432(4)	0.4747(4)	0	1	0.016(1)
KB	0.3333	0.6666	0.5	1	0.039(2)
KC	0.5	0	0.5	0.916(6)	0.030(2)
KD	0.3002(4)	0	0	0.699(4)	0.094(4)
WF	0.118(1)	0	0	0.345(7)	0.141(1)
WH	0.1139(7)	0	0.357(1)	0.409(4)	0.141(1)
WI	0.255(1)	0.1276(6)	0	0.52(1)	0.141(1)
WJ	0.210(1)	0.1095(7)	0.204(4)	0.323(6)	0.141(1)
WK	0	0	0.094(1)		
		244 °C			
T1	0.0942(1)	0.3575(1)	0.5	1	0.021(5)
T2	0.1659(2)	0.4981(1)	0.2105(2)	1	0.021(5)
O1	0	0.2740(5)	0.5	1	0.027(1)
O2	0.1633(2)	0.3266(5)	0.5	1	0.027(1)
O3	0.2646(2)	0.5293(4)	0.2542(8)	1	0.027(1)
O4	0.1022(2)	0.4140(2)	0.3253(5)	1	0.027(1)
O5	0.4241(1)	0.8483(3)	0.2648(9)	1	0.027(1)
O6	0.1434(3)	0.4746(3)	0	1	0.027(1)
KB	0.3333	0.6666	0.5	1	0.035(2)
KC	0.5	0	0.5	1	0.050(2)
KD	0.3129(3)	0	0	0.644(3)	0.065(2)
		707 °C			
T1	0.0951(2)	0.3591(2)	0.5	1	0.035(5)
T2	0.1652(2)	0.4983(2)	0.2078(2)	1	0.035(5)
O1	0	0.2775(6)	0.5	1	0.044(1)
O2	0.1628(3)	0.3256(5)	0.5	1	0.044(1)
O3	0.2646(2)	0.5292(4)	0.2516(8)	1	0.044(1)
O4	0.1026(3)	0.4139(3)	0.3240(4)	1	0.044(1)
O5	0.4237(2)	0.8475(4)	0.2620(9)	1	0.044(1)
O6	0.1408(4)	0.4707(4)	0	1	0.044(1)
KB	0.3333	0.6666	0.5	1	0.085(3)
KC	0.5	0	0.5	1	0.094(2)
KD	0.3095(4)	0	0	0.573(3)	0.093(4)

Table 5.1.4. Framework and extraframework bond distances less than 3.2 Å for the structures at RT, 101°, 244°, and 707 °C. The too short distances can be justified by the not simultaneously presence of the involved atoms, due to their partial occupancy factors.

	RT	101 °C	244 °C	707 °C
T1-O1	1.654(5)	1.655(5)	1.648(5)	1.641(4)
O2	1.627(4)	1.616(4)	1.634(4)	1.636(3)
O4 [X2]	1.636(4)	1.639(4)	1.633(3)	1.629(3)
average	1.638	1.637	1.637	1.634
T2-O3	1.681(4)	1.669(4)	1.645(4)	1.653(4)
O4	1.647(5)	1.624(5)	1.636(5)	1.645(5)
O5	1.617(3)	1.624(3)	1.628(2)	1.616(3)
O6	1.616(2)	1.634(2)	1.633(2)	1.636(2)
average	1.640	1.638	1.636	1.638
KB-O3 [x6]	2.809(6)	2.830(6)	2.859(6)	2.879(6)
KC-O5 [x4]	2.985(6)	2.976(6)	2.994(6)	3.013(6)
KD-O4 [x4]	3.145(2)	3.151(2)	3.078(5)	3.094(4)
O6 [x2]	3.005(6)	2.948(6)	2.822(7)	2.800(5)
WI [x2]	2.819(4)	2.842(4)		
WF-WF[x2]	2.06(2)	2.19(2)		
WH [x2]	2.891(1)	2.688(1)		
WI [x2]	2.53(1)	2.53(1)		
WJ[x4]	2.502(2)	2.42(1)		
WK [x2]	2.32 (2)	2.30(2)		
WH-O1	2.93(1)	3.08(1)		
WF[x2]	2.891(1)	2.688 (1)		
WH[x2]	2.16(1)	2.08(1)		
WH	1.71(2)	2.10(3)		
WH[x2]	2.75(2)	2.96 (2)		
WJ[x2]	1.540(6)	1.540(6)		
WJ[x2]	2.83(1)	2.201(8)		
WK	2.83(1)	2.89(1)		
WI-KD [x2]	2.819(4)	2.842(4)		
WF[x2]	2.53(1)	2.53(1)		
WJ[x2]	2.562(7)	1.693(7)		
WJ-O2	2.98(1)	2.87(2)		
WF[x2]	2.51(2)	2.38(2)		
WH[x2]	1.56(1)	2.18(2)		
WH[x2]	2.84(2)			
WI	2.562(7)	1.693(7)		
WJ[x2]	2.66(1)	3.12(4)		
WK	2.86(1)			
WK-WF[x6]	2.31(2)	2.29(2)		
WH[x6]	2.84(2)	2.91(6)		
WJ[x6]	2.86(1)			
WK	2.10(9)	1.37(2)		

References

[1] Artioli G., Kvick A. (1990) *Eur. J. Mineral*., 2, 749–759

[2] Baerlocher Ch., McCusker L.B., Olson D.H. (2007) Atlas of Zeolite Framework Types, 6th ed., Elsevier, Amsterdam,

[3] Lee Y., Kim S.J., Ahn D.C., Shin N.S. (2007) *Chem. Mater*., 19, 2277–2282

[4] Newsam J.M. (1989) *J. Phys. Chem.*, 93, 7689–7694

[5] Cruciani, G. (2006) *J. Phys. Chem. Solids*, 67, 1973–1994

[6] Lightfoot P., Woodcock D.A., Maple M.J., Villaescusa L.A., Wright P.A., J. (2001) *Mater.Chem.*,11, 212-216

[7] Baur W.H. (1992), *J. Solid State Chem.*, 97, 243–247

6.1. ZL/FL COMPOSITES

6.1.1 Synthesis of ZL/FL composites

FL was inserted into the channels of ZL by using gas-phase adsorption. Four ZL/FL samples (hereafter reported as ZL/0.5FL, ZL/1.0FL, ZL/1.5FL and ZL/2.25FL) were synthesized with nominal loadings of 0.5, 1.0, 1.5 and 2.25 molecules p.u.c, following the experimental set up reported in [1].

Zeolite L was preliminary dehydrated at 200°C for 4 h under vacuum (10^{-4} mbar) on the basis of the results of the dehydration and rehydration study reported in [2]. Dehydrated ZL was mixed, in inert atmosphere, with FL powder - in ratios corresponding to the desired loadings - and placed in a rotating oven. The mixture was kept at 120 °C for 24 h in order to assure the encapsulation of the dye and its homogenous distribution in the zeolite channels.

6.1.2. TGA-MSEGA

Water and fluorenone contents in the ZL/FL composites were determined by TGA-MSEGA. During the thermal analysis coupled with MSEGA the intensity changes of 8 species (m/z = 16 (CH_4), 18 (H_2O), 28 (CO), 30 (CH_3CH_3), 44 and 45 (CO_2) 78 (C_6H_6) and 180 ($C_{13}H_8O$)) were followed as a function of temperature.

Figure 6.1.2.1 shows the TG (a) and DTG curves (b) as a function of temperature for the as-synthesized ZL, pure crystalline FL and ZL/FL composites.

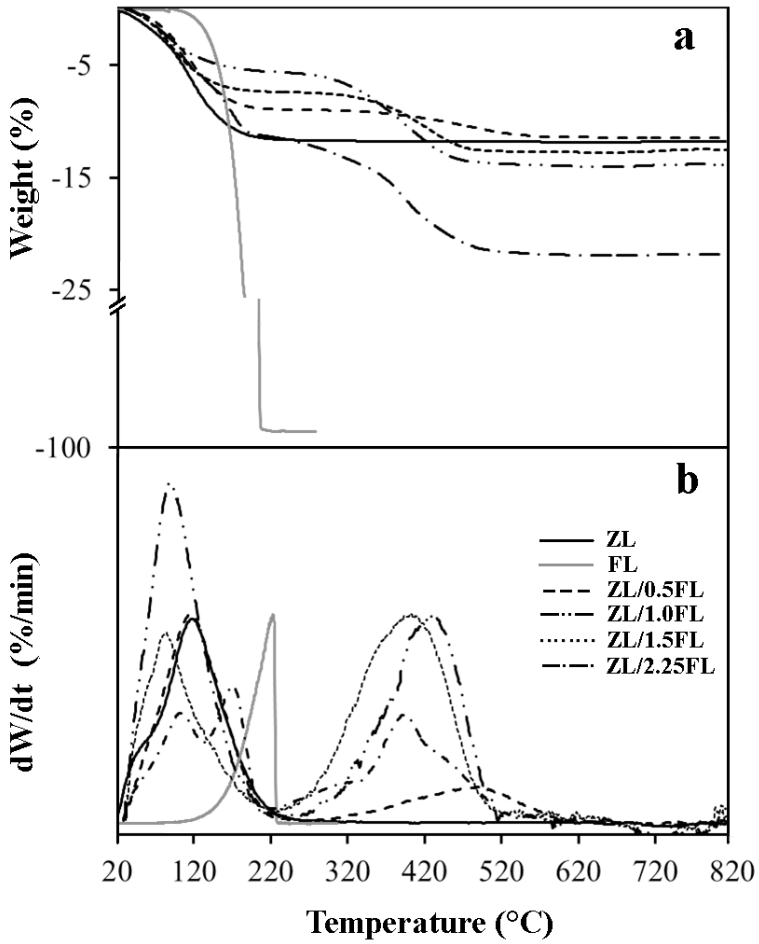

Figure 6.1.2.1. TGA (a) and DTG curves (b) ZL (black solid curve), crystalline dye FL (grey solid curve) and the ZL/0.5FL(dashed black line), ZL/1.0FL (dashed-double dot black line), ZL/1.5FL (dotted black line) and ZL/2.25FL(dashed-dot black line) composites.

As shown in Figure 6.1.2.1 and Table 6.1.2.1, in the four composites the water release occurs at about 100°C and the weight losses are 8.7%, 7.3%,5.5 % and 5.4% in ZL/0.5FL, ZL/1.0FL, ZL/1.5FL and ZL/2.25FL, respectively. The water loss temperature slightly decreases when the water amount in the composite decreases as a consequence of the FL penetration. The fluorenone release in the composites occurs as in crystalline FL in one step, but at higher temperature in the range (250 - 550°C). This indicates that FL is not simply physisorbed on the zeolite surface, but is encapsulated into the zeolite channels. It is worth noting that the release temperature decreases with increasing the FL loading thus indicating an influence of loading on the host-guest FL-ZL interactions.

Table 6.1.2.1. Temperature of water and fluorenone release, weight loss and number of molecules (water and fluorenone) determined by TGA-MSEGA, compared with those obtained by the structure refinement for the ZL/FL composites.

Sample	Water loss T (°C)	Water wt. %	Water molecules (TGA)	Water molecules (structure refinement)	FL loss T(°C)	FL wt.%	FL molecules	FL molecules (structure refinement)
ZL	110	11.9	18	18	-	-	-	---
ZL/0.5FL	106	8.7	13.6	14.7	500	2.8	0.43	0.49
ZL/1.0FL	104	7.3	11.5	9.7	440	5.6	0.88	0.98
ZL/1.5FL	101	5.5	8.8	7.0	403	8.7	1.43	1.5
ZL/2.25FL	102	5.4	8.8	--	400	9.5	1.5	--

The sample ZL/2.25FL shows a further weight loss at 170°C, absent in the TG curve of all the other composites. This can be interpreted as the result of the removal of a portion of FL not confined in zeolite porosities but present as crystalline phase. This fact is confirmed by the XRPD pattern collected on this sample, showing reflections pertaining to the fluorenone phase (Figure 6.1.2.2.).

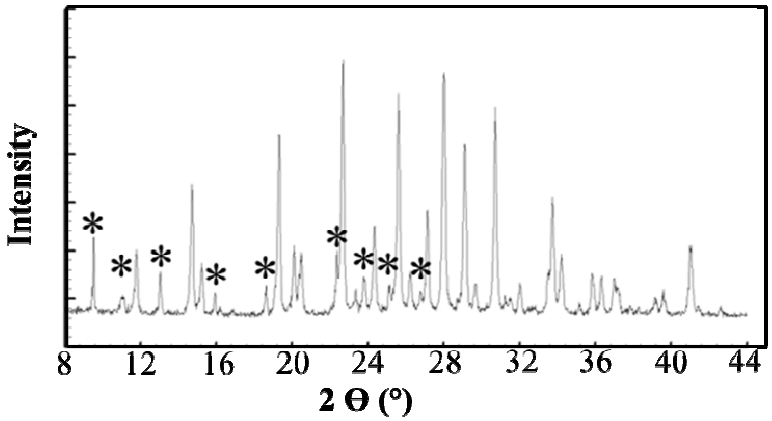

Figure 6.1.2.2. Portion of the XRPD pattern of ZL/2.25FL composite. The asterisks indicate the peaks of crystalline FL not adsorbed in ZL.

On the basis of the mass spectrometry results, we determined that, when confined in the zeolite L, FL is released as CO_2 and C_6H_6. The weight losses at high temperature corresponding to the encapsulated FL are, 2.8 %, 5.6 %, 8.7 % and 9.5 % (corresponding to

0.44, 0.9, 1.43 and 1.5 FL molecules) in ZL/0.5FL, ZL/1.0FL, ZL/1.5FL and ZL/2.25FL composites, respectively (Table 6.1.2.1, Appendix B). These results, and in particular the presence of only 1.5 molecules in the sample ZL/2.25FL, indicate that the maximum possible loading of the dye in zeolite L is 1.5 molecules p.u.c. Crystalline fluorenone detected in ZL/2.25FL composite corresponds to the exceeding dye crystallites external to the ZL channels; consequently, this sample was not further investigated. In all the investigated composites the amounts of water and FL are, as expected, inversely correlated, indicating that FL, entering the channels, replaces the water molecules.

6.1.3. ATR-IR ANALYSIS

In Figure 6.1.3.1 ATR-IR spectra (a: 3800-3000 cm^{-1}, b: 1750-1550 cm^{-1}) of the four ZL/FL composites (labeled "after") are compared with those collected on the mixtures of ZL and FL powders that did not undergo the gas phase adsorption (labeled "before"). The spectra of the pure phases (ZL, solid FL and FL solution in cyclohexane) are also reported for comparison. Among the IR signals, the vibration of carboxylic group of FL (at 1711 cm^{-1} in solid and 1716 cm^{-1} in cyclohexane solution) is expected to be particularly informative on the nature of the chemical environment around FL molecule, being easily red shifted if directly involved in interactions with positive charges (as in the case of FL grafting on K^+ ions). For what concerns the 3800 - 3000 cm^{-1} region, it is apparent that the broad band centered at about 3400 cm^{-1}, essentially related to the water present in the zeolite channels [3] has a lower intensity after the formation of the ZL/FL composites. This feature is particularly evident for the ZL/1.5FL material. The decrease in intensity of this band is accompanied, as expected, by the decrease of the band at 1640 cm^{-1}, associated to the H-O-H bending vibrations in water molecules. Interestingly, the lowering of the IR signals related to water is accompanied by the simultaneous decrease of the relative intensity of the peak at 1714 cm^{-1} and increase of that centered at 1693 cm^{-1} with respect to what observed in the spectra before the FL encapsulation. Such bands are associated to the C=O group in FL physisorbed outside the zeolite pores and to the C=O group interacting with positive charges, respectively [4] Moreover, the presence of an isosbestic point between the 1640 and the 1695 cm^{-1} peaks is a clear indication that the FL grafting in the pores (FL molecules coordinating K^+) limits the rehydration of the zeolite once the composite is obtained. It is also interesting to observe that, by simply mixing the two powders, only a small fraction of FL is in interaction with K^+

cations (likely present on the external surface of zeolite crystals) (Fig. 6, before), whereas the most part of the molecules is physisorbed or located in an almost apolar environment.

All IR features of FL result to be strongly increased in intensity after the grafting, as expected for the introduction of the molecule in a strong polarizing environment as the ZL pores. From these findings, it is evident that most of FL molecules enter into the zeolite channels forming the ZL/FL composites. It is important to stress how the ATR-IR technique reveals its suitability to quickly verify the grafting of dye molecules, bearing a functional group, as C=O, spectroscopically highly sensitive to the chemical environment.

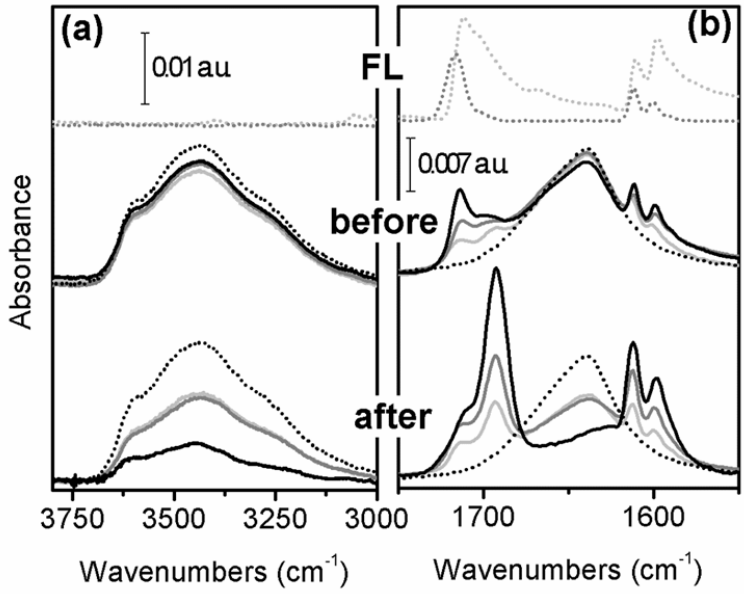

Figure 6.1.3.1. ATR-IR spectra as obtained in air for the samples ZL/0.5FL (solid light grey), ZL/1.0FL (solid grey) and ZL/1.5FL (solid black line) "before" FL adsorption (i.e. on the powder mixtures) and "after" FL adsorption (i.e. on the composites). ZL (dotted black line) and FL (dotted light grey line: solid fluorenone; dotted grey line: cyclohexane solution) spectra are also reported for comparison. (a) 3800-3000 cm^{-1}: O-H stretching region. (b) 1750-1550 cm^{-1}: C=O and C-H stretching and O-H bending region.

6.1.4. TRANSMISSION FT-IR

Transmission FT-IR spectra was carried out dehydrating a ZL/FL composite to verify if the water molecules play a role on the organization of the FL molecules and on the guest-guest and host guest interactions.

The Figure 6.1.4.1 shows as only the C-H stretching bands of FL are perturbed during the water removal, whereas all the other FL bands (1800-1200 cm^{-1} range, right part of Figure

6.1.4.1) are not shifted during the dehydration process. This result highlights as the water molecules do not strongly perturbate the fluorenone molecules in the ZL channels and that it is not involved in any host-guest interaction.

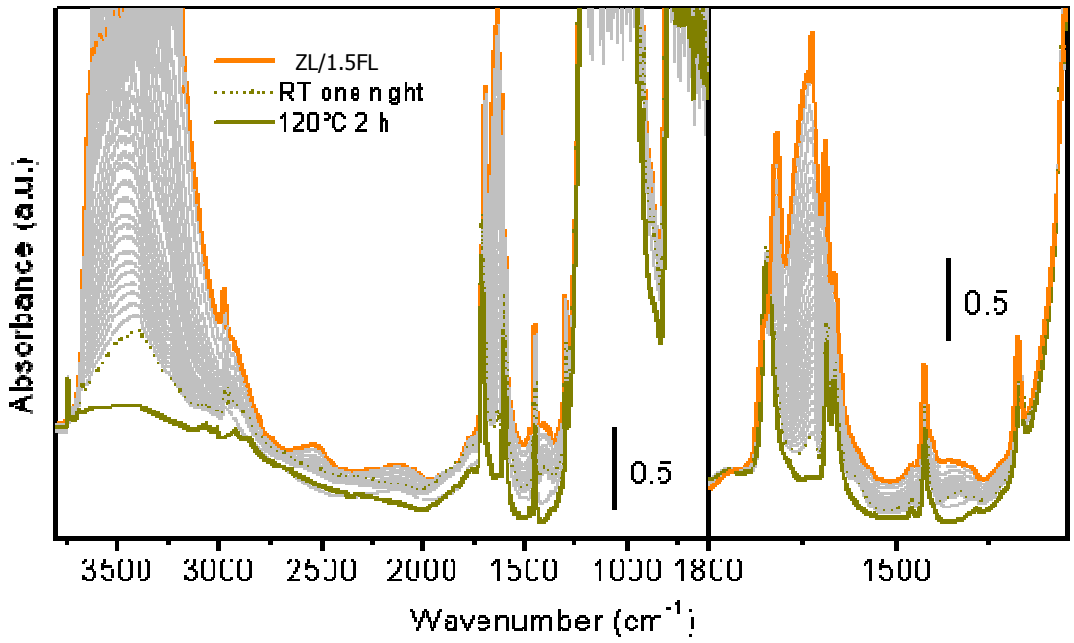

Figure 6.1.4.1 FT-IR spectra as obtained in air (orange line), and after treatment in vacuum at 120°C for 2 h (green line) for the samples ZL/1.5FL. Left: 3800-1800 cm^{-1}range; right: 1300-1800 cm^{-1} region.

6.1.5. STRUCTURE REFINEMENT

The comparison among the XRPD patterns collected on the as-synthesized ZL and on the ZL/FL composites shows differences in the intensity of some diffraction peaks, the most significant being related to low 2Θ angle region (Fig. 6.1.5.1). It is well known that in zeolites, the intensity of the low angle peaks of the diffraction pattern is related to the extraframework distribution. Thus, these changes are consistent with the FL penetration.

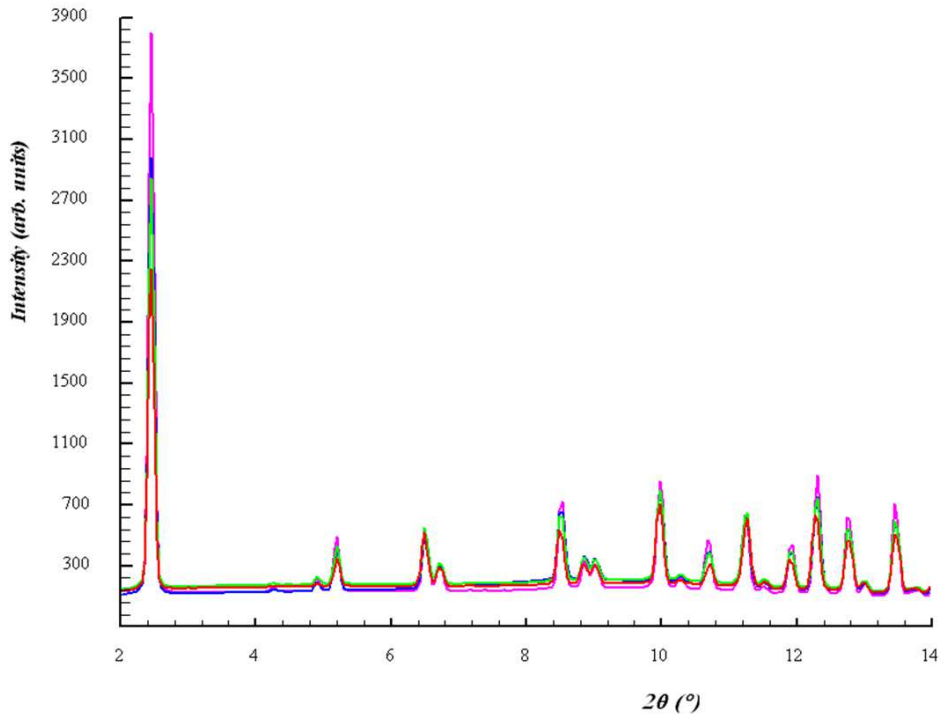

Figure 6.1.5.1. Comparison of the intensity of the patterns of the as-synthesized ZL (fuxia line) and the ZL/0.5FL(blue line), ZL/1.0FL (green line), ZL/1.5FL (red line) composites.

Only small changes in the cell parameters occurs, in particular a slight increase of *a* and a decrease of *c* parameters are observed in the composites with respect to the original material (Table 6.1.5., Appendix B).

Comparing the results of the structural refinements of the as-synthesized ZL with that of the three composites, slight deformations of both the channels running parallel to *c* axis can be observed, increasing the FL loading. In particular the 12MR channel becomes more circular, while the 8MR one assumes a more elliptical shape (Fig. 6.1.5.2 and Tables 6.1.5.2 and 6.1.5.3 in Appendix B). The combined effect of widening/contraction of the two channels justifies the minor variations in the unit cell parameters reported in Table 6.1.5.1 in Appendix B.

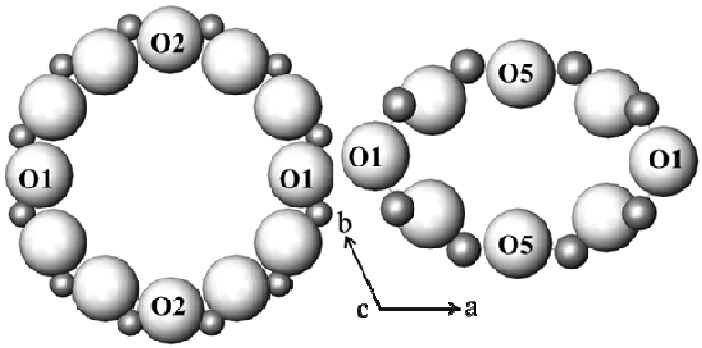

Sample	12MR		8MR //*c*	
	O1 O1	O2 O2	O1 O1	O5 O5
ZL	10.10	10.43	8.29	4.87
0.5ZL/FL	10.10	10.52	8.29	4.63
1.0ZL/FL	10.14	10.46	8.26	4.60
1.5ZL/ FL	10.21	10.47	8.21	4.57

Figure 6.1.5.2. Dimensions of the 12MR and 8MR channels parallel to [001] before (as-synthesized ZL) and after the adsorption of FL.

As regards the extraframework species, in all the studied samples we can observe a general disordered distribution of water and FL molecules on partially occupied, highly symmetric positions. The extraframework sites KD, WI and WJ undergo small coordinates changes, as a consequence of dye penetration, as discussed in the following sections.
The structural refinements of the ZL/0.5FL and ZL/1.0FL composites gave similar results and are hence described together in the following paragraph.

ZL/0.5 and ZL/1.0FL composites

The refinements revealed the presence of 0.49 and 0.98 FL molecules p.u.c in the ZL/0.5FL and ZL/1.0FL composites respectively, in good agreement with the indications of the TGA analysis (Table 6.1.2.1). These molecules are sited on the mirror planes parallel to *c* axis, statistically occupying one of the six equivalent positions generated by the presence of the 6-fold axis parallel to [001] (Tables 6.1.5.2 and 6.1.5.4 in Appendix B and Figs. 6.1.5.3 a, b).

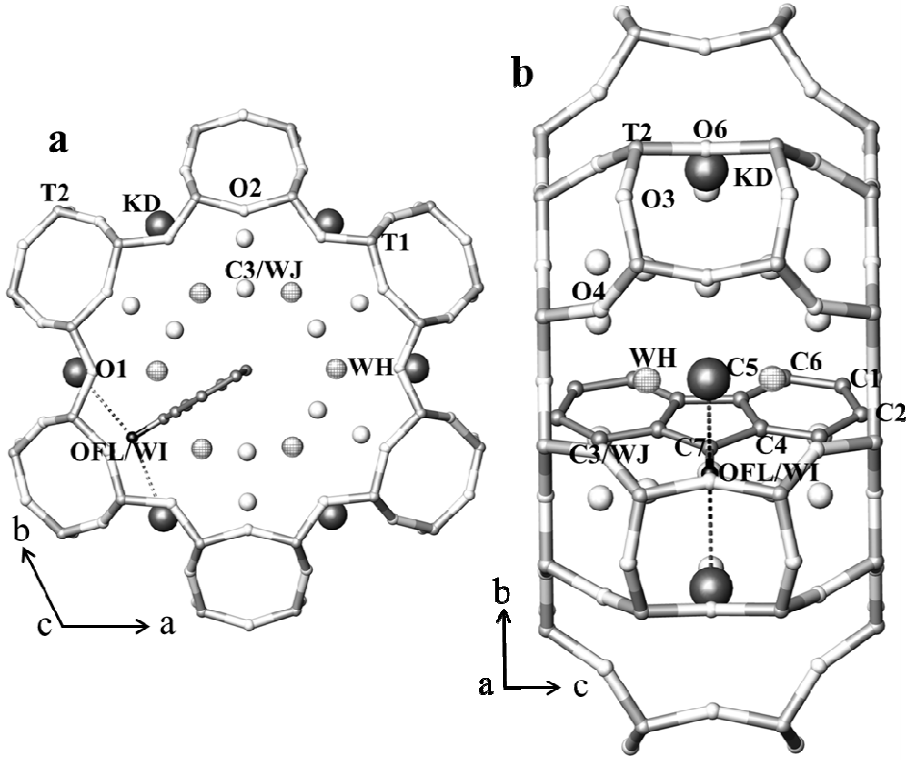

Figure 6.1.5.3. Projection along *c* axis (a) and *b* axis (b) of the ZL/0.5FL and ZL/1.0FL structure showing the arrangement of the FL and water molecules in the 12 MR channel. Only one of the six equivalent FL molecules is represented for sake of clarity. The grated sphere represents the water molecule WH, present only in the ZL/0.5FL sample.

In both composites, the oxygen of the carbonyl group (OFL) is oriented towards the two equivalent potassium atoms (KD), located along the walls of the 12MR channel. The distances between OFL and KD 2.81(6) and 2.86(7) for ZL/0.5FL and ZL/1.0FL, respectively) confirm that in both samples there is a strong interaction between these two atomic species, in keeping with the data of ATR-IR analysis (Fig. 6.1.3.1).

Along with the dye, water molecules were also located in the 12MR channel; specifically, 14.7 molecules/u.c. in the ZL/0.5FL composite (distributed over the three independent, partially occupied, sites WH, WJ and WI) and 9.6 molecules/u.c. in the ZL/1.0FL one (distributed over the two independent, partially occupied, sites WJ and WI) (Table 6.1.2.1, Appendix B). The OFL oxygen atom and C3 carbon occupy the same positions occupied by water molecules WI and WJ in the as-synthesized material. These sites, hereafter labeled OFL/WI and C3/WJ (Tables 6.1.5.2. and 6.1.5.3, Appendix B), showed occupancy factors

higher than those of the other carbon sites, hence suggesting a possible sharing by water molecules and FL atoms (Fig. 6.1.5.3). These results, in particular the higher amount of water in the less loaded sample, are in good agreement with those found by TGA and IR spectroscopy.

ZL/1.5FL composite

From the refinement of the ZL/1.5FL composite a total of 1.48 FL molecules per unit cell were located, distributed over partially occupied sites, in line with the TGA analysis (Table 6.1.2.1, Appendix B). However, the disordered distribution of water and FL molecules in the extraframework sites greatly contributes to make the determination of the FL positioning/orientation in ZL/1.5FL from electronic density maps a very challenging task. Nevertheless, exploratory structure refinement attempts were performed by forcing the ZL framework 6-fold symmetry, and two FL orientations were deduced. The first – FL in Table 6.1.5.2 in Appendix B– (accounting for 0.5 molecules per unit cell) corresponds to the orientation found for the FL molecule in the ZL/0.5FL and ZL/1.0FL composites. The second – FL' in Table 6.1.5.2 in Appendix B –features the FL molecular long axis parallel to *c* axis, but with some atoms outside the mirror plane parallel to [001] (accounting for 1.0 molecule per unit cell). On the basis of the size and geometry of FL molecule, and considering the bond distances among the dye molecules obtained by the refinement, the only possible distribution of fluorenone compatible with these symmetry constraints and orientations is that reported in Figure 6.1.5.4 a, b. In particular, if we consider two adjacent unit cells, one should be occupied by two equivalent nearly parallel FL' molecules (among the 12 symmetrically equivalent FL' molecules) while the other should contain one FL molecule (corresponding to 1.5 mol/u.c.). Also in this model every oxygen atom of the guest molecules is coordinated to two KD sites (see Table 6.1.5.4, Appendix B).

As already observed in the 0.5ZL/FL and 1.0ZL/FL composites, the refinement located the water molecules in the OFL/WI and C3/WJ sites (Tables 6.1.5.2 and 6.1.5.4, Appendix B). The FL'-water separations well below the values that should be expected from the corresponding van der Waals radii, e.g., the OFL' atom is at distances of 1.07 Å and 2.89 Å from WI and WJ, while C3' is at distances of 2.87 Å and 1.31 Å from WI and WJ. The reliability of this results is due to the partial occupancy of the dye and H_2O atoms and we can assure that the position of the water will vary from unit cell to unit cell and will depend on the

actual location of FL in a specific unit cell. Therefore, even though the R/F^2 value for this refinement may be considered rather good (8.7 %) in view of the high number of variables, the 6-fold symmetry constraint imposed in the refinement a main structural inconsistencies related to the too short C-C distance (2.56 Å) between the FL and FL' molecules placed in two adjacent cells remain in the final structural model. To solve this inconsistence and provide a realistic structural model of the FL packing inside the composite, density functional calculations were performed.

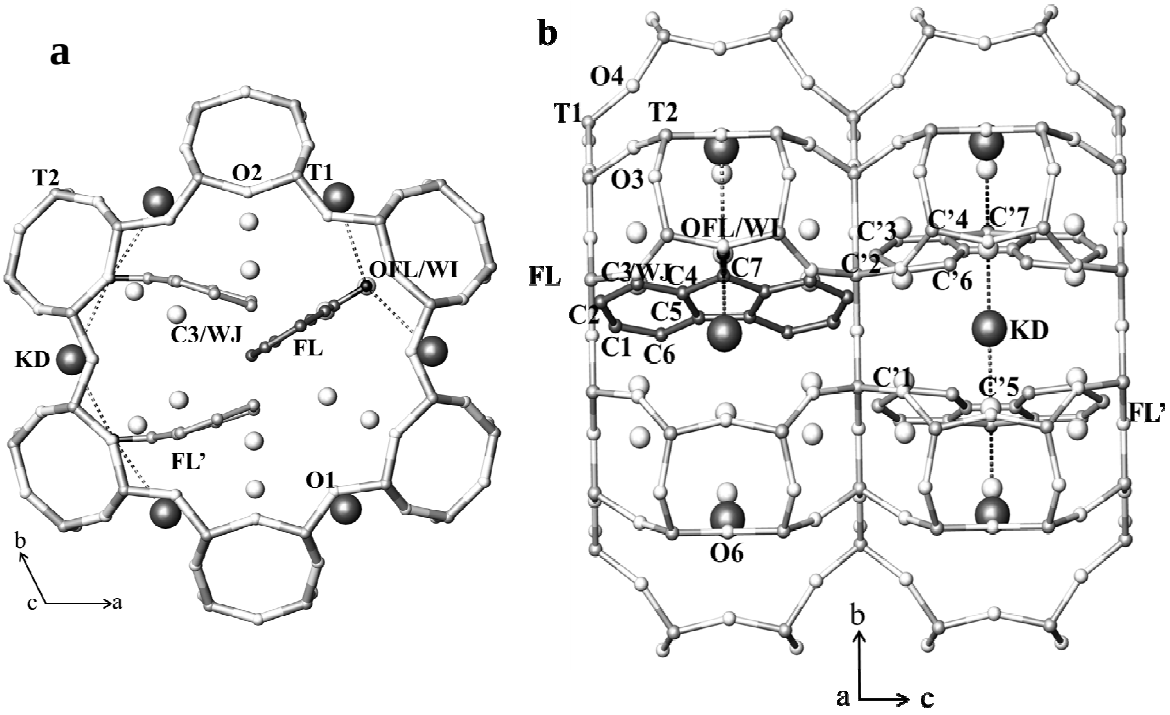

Figure 6.1.5.4. View of 12MR channel (a) and arrangement of the FL and water molecules along the same channel (b) in the ZL/1.5FL composite. Only one FL and two FL' molecules are represented for sake of clarity. Projection along *c* axis (a) and *b* axis (b) of the ZL/1.5FL structure showing the arrangement of the FL and water molecules in the 12 MR channel. In (b) two cells are represented to show the distribution of the three FL molecules.

6.1.6. MODELS AND CALCULATIONS

Calculations on the ZL/0.5FL composite (simulation cell stoichiometry: $K_{18}[Al_{18}Si_{54}O_{144}]$•1FL, with the PBE functional and periodic boundary conditions, were previously performed and thoroughly described in [5, 6].

In order to establish which arrangements of FL molecules is possible inside ZL channels, dry ZL/FL models were first considered. Local energy minima for the dry ZL/1.0FL and ZL/1.5FL models, characterized by simulation cell stoichiometries $K_{18}[Al_{18}Si_{54}O_{144}]\cdot 2FL$ and $K_{18}[Al_{18}Si_{54}O_{144}]\cdot 3FL$ respectively, were obtained by geometry optimization of different guess configurations. The guess configurations for the ZL/1.0FL and ZL/1.5FL systems were built by inserting two and three FL molecules per simulation cell, respectively (convergence criterion: $5.\times 10^{-4}$ au for forces on atoms). In the ZL/1.5FL model, one ZL unit cell contained 2 FL molecules and the adjacent one 1 FL molecule. In the case of the ZL/1.0FL system, two different models were considered: model (1-1), characterized by an occupancy of 1 FL molecule per ZL unit cell, and model (2-0), where one ZL unit cell contained 2 FL molecules and the adjacent one 0 FL molecules. The guess geometries of both the (1-1) and (2-0) models were built by positioning the FL molecules so that their C=O groups were either in a parallel ("sin") or antiparallel ("anti") configuration (see Figure 6.1.6.1., panels a-d). In all cases, the stabilization energy of the composites with respect to the isolated ZL and FL components was calculated with the formula:

$$\Delta E(\mathrm{ZL}\cdot \mathrm{nFL}) = E(\mathrm{ZL}\cdot \mathrm{nFL}) - E(\mathrm{ZL}) - n\times E(\mathrm{FL})$$

where E(ZL·nFL) is the energy of the optimized dry ZL/nFL model (n=2,3 for ZL/1.0FL and ZL/1.5FL, respectively), E(ZL) is the energy of the empty ZL, while E(FL) is the energy of an isolated FL molecule calculated in the same simulation cell.

In the case of the low FL-content system, *i.e.*, the ZL/0.5FL composite, an atomistic-level structural description was obtained from both 0 K energy minimization and room temperature first principles molecular dynamics (FPMD) trajectories, as discussed in ref. [5], to which we refer for further details.

Once obtained the minimum energy structure of the dry ZL/1.5FL system, corresponding to the maximum degree of FL loading, several hydrated models characterized by stoichiometry $K_{18}[Al_{18}Si_{54}O_{144}]\cdot 3FL\cdot 13H_2O$ were built by adding 13 water molecules in the simulation cell. Such a number of water molecules was chosen to match the experimentally determined unit cell water content (Table 6.1.2.1, Appendix B); nevertheless, ZL/1.5FL models containing 12

and 14 water molecules in the simulation cell were also considered. Stabilization energies of the hydrated ZL/1.5FL models with respect to the isolated components were calculated with the formula:

$$\Delta E(ZL\cdot 3FL\cdot xH_2O) = E(ZL\cdot 3FL\cdot xH_2O) - E(ZL) - 3\times E(FL) - x\times E(H_2O)$$

where $E(ZL\cdot 3FL\cdot xH_2O)$ is the energy of the optimized hydrated ZL/1.5FL model (x=12,13,14), $E(ZL)$ is the energies of the empty ZL, while $E(FL)$ and $E(H_2O)$ are respectively the energies of an isolated FL molecule and an isolated water molecule calculated with the same simulation cell parameters. The relative stabilities of the systems with 12 and 14 water molecules with respect to that containing 13 H_2O, were calculated with the formulas:

$$\Delta E(14/13) = E(ZL\cdot 3FL\cdot 14H_2O) - [E(ZL\cdot 3FL\cdot 13H_2O) + E(H_2O)]$$

$$\Delta E(12/13) = E(ZL\cdot 3FL\cdot 12H_2O) - [E(ZL\cdot 3FL\cdot 13H_2O) - E(H_2O)]).$$

Modeling of dry ZL/FL adducts

In order to try unraveling the structure of the FL organization in ZL nanochannels, let us first recall that the fluorenone molecular length, 8.9 Å along its longest axis, is greater than the ZL cell dimension along the channel (c = 7.52 Å). FL is however noticeably shorter than the maximum channel opening (~12 Å), indicating that this dye could have orientational freedom inside the zeolite and should not necessarily align with the ZL channel axis. Actually, by increasing the FL content, a modest shortening of the cell along the c axis is detected, suggesting that, at high FL loading, an organization of the FL molecules in single file should be rather improbable. As reported in [5, 6], at low loading (i.e. 0.5 FL p.u.c.) the calculated minimum energy structure for a dry ZL/0.5FL system is characterized by a FL molecule coordinated, via the carbonyl oxygen, to a K^+ cation and oriented with its long molecular axis forming an angle of about 30º with the ZL c axis.

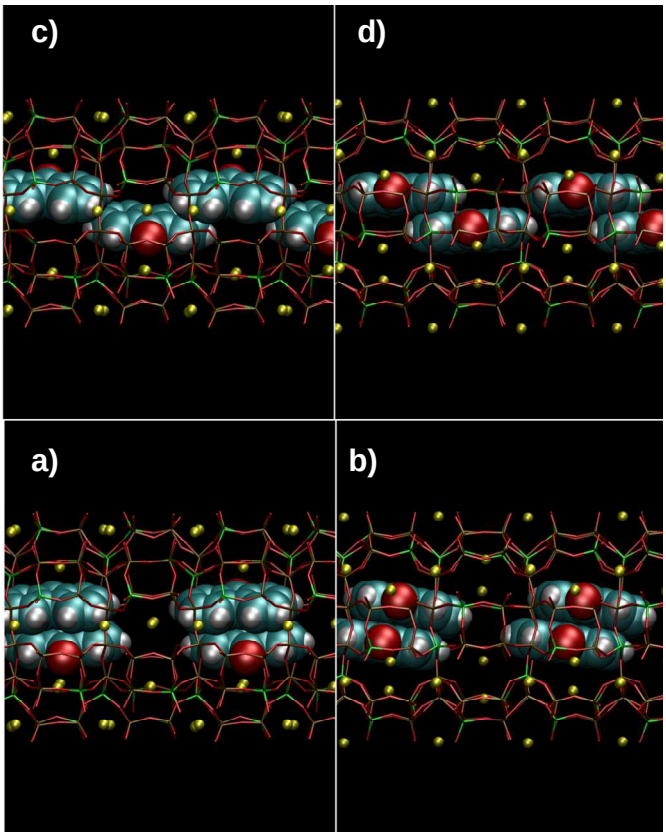

Figure 6.1.6.1. Graphical representation of minimum energy structures calculated for the ZL/1.0FL models. a): anti-(2-0) arrangement of the FL molecules; b): sin-(2-0) arrangement; c): anti-(1-1) arrangement; c): sin-(1-1) arrangement. ZL framework atoms represented as sticks (brown: Si, green: Al, red: O), K^+ as yellow spheres. FL atoms are in Wan-der-Waals representation (cyan: C, red: O, white: H).

The stabilization energy of this structure with respect to the isolated ZL and FL components amounts to -19.3 kcal mol^{-1}. Even though a geometry with FL long axis aligned with the channel direction is only 2.9 kcal mol^{-1} less stable than the minimum energy structure, at room temperature the FL most probable orientation is that with the molecular long axis at 30º with respect to the channel axis. Such angle decreases to 20º upon hydration, indicating that in humid conditions not only FL keeps contact with K^+ but also its average position and orientation inside the channel is only barely influenced [5,6]. Also, configurations with FL long axis perpendicular to the channel axis, where the FL carbonyl oxygen is far from the extraframework potassium cations, are much higher in energy than those aligned with the channel axis and become unstable at room temperature conditions, as evidenced by first-principles molecular dynamics [6].

Based on the above results and on host-guest structural properties, in the case of 1 FL per ZL unit cell the most probable supramolecular organization should feature the FL molecules approximately aligned with the channel axis and with their carbonyl oxygen directed towards the channel walls, where accessible K^+ ions are located. The geometry optimization of the several ZL/1.0FL models, mentioned above, indicates that the different optimized structures have comparable energies, separated by less than 1 kcal mol^{-1} (see Fig. 6.1.6.1). The most stable structure is an anti-(2-0) configuration, characterized by an antiparallel arrangement of the C=O groups (Fig. 6.1.6.1 a) and by a stabilization energy of -33.8 kcal mol-1 with respect to the isolated components. A sin-(2-0) arrangement (Fig. 6.1.6.1 b) is however nearly isoenergetic, being less stable than the minimum energy structure by only 1.2 kcal mol^{-1}. Also an anti-(1-1) structure, represented in Figure 6.1.6.1 c, is of comparable energy, being only 0.9 kcal mol-1 less stable than the anti-(2-0) one. On the other hand, the most stable among the sin-(1-1) arrangements (Fig. 6.1.6.1 d) is 8 kcal mol^{-1} higher in energy than the anti-(2-0). Since all these structures are characterized by distances between the FL carbonyl oxygen and K in line with the corresponding experimental values and compatible with a strong potassium-FL interaction, their different relative stabilities mainly derive from FL-FL interactions. Actually, the minimum energy structure for the ZL/1.0FL system is just the one characterized by the highest degree of FL packing, which maximizes the favorable Van der Waals interactions between the dye molecules.

Also for the maximum loading of 1.5 FL p.u.c. we have performed geometry optimization on different guess structures, all characterized by a (2-1) FL arrangement (see Fig. 6.1.6.2 a) The stabilization energy of the resulting minimum energy structure with respect to the isolated components amounts to -63.7 kcal mol^{-1}. Here the supramolecular organization consists of two FL molecules, FL1 and FL2, (in a sin configuration) located approximately inside one of the ZL unit cells with their long axes nearly parallel to each other and to the channel direction, while the third one, FL3, is positioned in the adjacent unit cell and oriented at about 45º with respect to the ZL channel axis. Indeed, the stronger intermolecular interactions and the severe structural constraints implied, by confinement in nanochannels at high packing conditions, force the FL molecules to organize just like a ladder with inclined rungs running along the ZL channel, as clearly evidenced in Figure 6.1.6.2. Indeed, the molecules are essentially planar and show only slight distortions from the ideal gas-phase FL structure, indicating that this ladderlike supramolecular architecture is achieved without any significant perturbation of the

FL molecular geometry. Moreover, the FL nanoladder still maintains some resemblance to the structure of the FL crystal [7], suggesting that, at high loading regimes, also guest-guest Van-der-Waals interactions may play a relevant role in governing the supramolecular organization of dye molecules in confined systems. As far as host-guest interactions are concerned, we notice that, in line with the above discussed experimental evidences, each FL is in close contact with the ZL K^+ cations via its carbonyl oxygen (see Fig. 6.1.6.2 a). More specifically, the distances of the three carbonyl oxygens from the K^+ cations amount to 2.539, 2.570, 2.676 Å respectively, indicating that, like in the case of lower FL-loading ZL/FL systems [5, 6], strong C=O/K^+ interactions lie at the origin of the organization of these dyes in ZL.

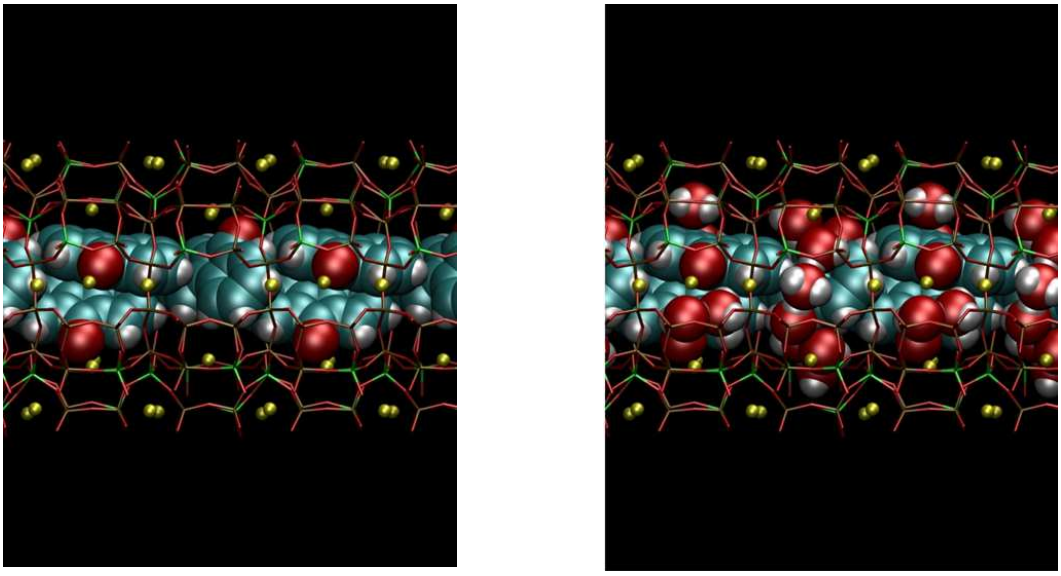

Figure 6.1.6.2. Graphical representation of the minimum energy structure calculated for the: a) dry ZL/1.5FL model; b) hydrated ZL/1.5FL model (with 13 H_2O in the simulation cell) Atom color codes as in Figure 6.1.6.1.

Hydrated system ZL/1.5FL

Several hydrated models of the ZL/1.5FL system were considered, characterized either by a different number of water molecules in the simulation cell (in the 12 – 14 range) or by a different starting arrangement of the FL and H_2O molecules. The minimum energy structure obtained by placing 13 water molecules in the simulation cell (the water content closest to the experimentally determined one) is shown in Figure 6.1.6.2 b. In this structure, 8 water molecules are located in the unit cell containing FL3 and the remaining 5 in that occupied by

the FL1 and FL2 molecules. In line with the results obtained on other dye-ZL composites [8], the water molecules are mainly clustered in the ZL channel region characterized by a lower local concentration of the dye and tend to adopt a quasi-tetrahedral organization mimicking that of water in the condensed phases, in order to maximize the number and strength of hydrogen bonds. Indeed, the high value of the stabilization energy calculated for this structure, -179.9 kcal mol^{-1}, indicates that water actively contributes to stabilize the dye molecules packing inside the zeolite nanochannels. As clearly evidenced in Figure 6.1.6.2 b, besides slight deformations related to the water co-presence, the arrangement of the FL molecules resembles quite closely the FL nanoladder found in the dry ZL/1.5FL composite. It can therefore be concluded that, at ambient temperature and pressure conditions, water molecules do not significantly perturb the FL supramolecular organization. This finding is nicely in line with the fact that FL molecules interact more strongly with the zeolite than water, as demonstrated in [5]. Due to the dominant FL-K^+ interaction, water molecules cannot displace the dye from the zeolite, but they seem incorporate FL molecules into their hydrogen bond network and finely tune their positioning and orientation inside the ZL channel through hydrogen bond interactions. Actually, the distances of the three carbonyl oxygens from the zeolite K^+ cations, amounting to 2.524, 2.590, 2.848 Å respectively, are very close to those of the dry ZL/1.5FL system, confirming that the presence of water has only very minor effects on FL/zeolite interactions and, as a consequence, does not significantly influence the supramolecular arrangement of closed-packed FL molecules. As far as the water content is concerned, we found that the system containing 13 H_2O is more stable of both the systems containing 12 or 14 water molecules, by 35.7 and 9.2 kcal/mol respectively. The greater energy stability of the 13 H_2O composite, with respect to the 12 H_2O one, can be easily rationalized on the basis of the higher number of hydrogen bond interactions. Nevertheless, the minimum energy structure obtained at higher water content (14 H_2O) is less stable than the 13 H_2O one because, as a result of the reduced available space inside the ZL channel, the geometry of the FL molecules exhibits larger distortions from the ideal planar FL structure. In conclusion, computational results nicely support the water content value determined experimentally for the high FL content composite and provide, for the first time, a reliable molecular-level picture of the arrangement of dye molecules in ZL nanochannels.

6.1.7. OPTICAL SPECTROSCOPY

The experimental UV-Vis absorption spectra for the ZL/FL composites are reported in Figure 6.1.7.1. The spectra obtained are in perfect agreement with the spectra reported in literature [1].

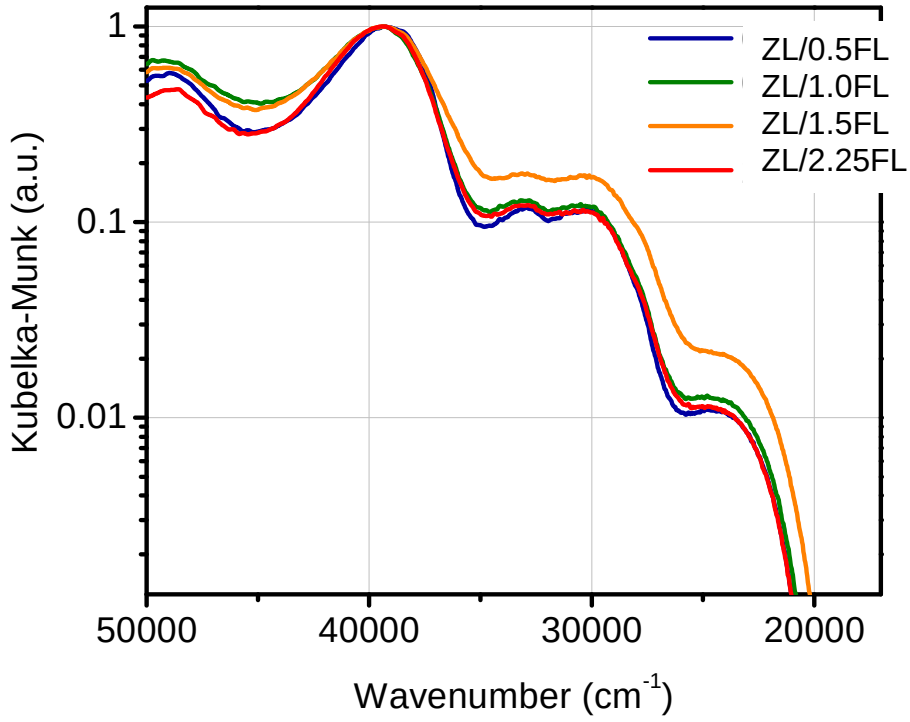

Figure 6.1.7.1 DR-UV-Vis absorption spectra for the ZL/FL diluted in ZL by mechanical mixing.

The normalization of the spectra allows to evidence as the shape and the band positions of the DR-UV-Vis spectra are identical and therefore independent on the FL loading. This result was unexpected given by the experimental and calculated ZL/FL structures reported above. Moreover, the spectrum of the ZL/2.25FL composite shows the same trend of the other composites and hence it is difficult, with this technique, to distinguish the dye incorporated in the zeolite from that only physysorbed on the surface, as have been clearly demonstrated by TG-MSEGA and XRPD analysis.

A larger effect of the different molecular organization is observed, on the contrary, in the emission spectra of the ZL/FL hybrid materials, reported in Figures 6.1.7.2 a, b.

All the composites were excited at 330 and 440 nm.

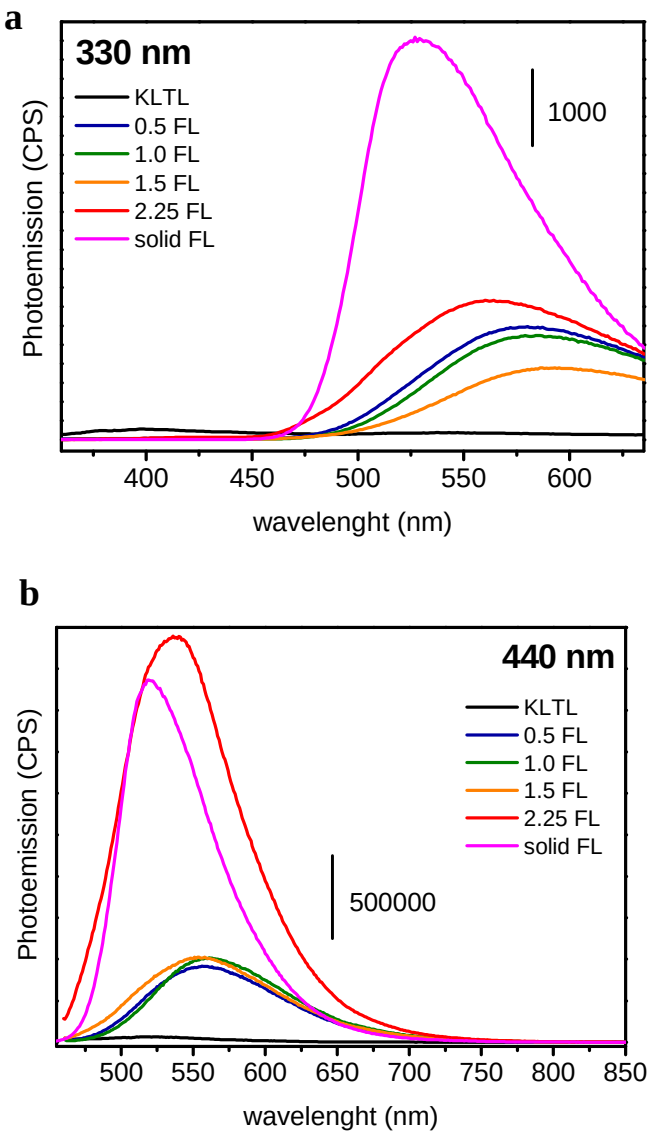

Figure 6.1.7.2 a) Photoluminescence at 330 nm of the pure FL, ZL and the ZL/FL composites; b) photoluminescence at 440 nm of the pure FL, ZL and the ZL/FL composites.

At 330 nm a single emission band at about 520 nm is observed for FL, the increase of the loading caused a red shift of the maximum in the composites while the emission intensity decrease from 0.5 to ZL/1.5FL composites. A red shift usually can be due to the interaction of the dye molecule with a cation or to self-absorption phenomenon [4].

In the emission spectra collected at 440 nm, again a single band is observed with a maximum in the composites at about 550 nm. In this case the red shift of the maximum is not so evident.

Otherwise from that reported for the absorption spectra, in Figure 6.1.7.2 b the ZL/2.25FL sample shows an high intensity and a blue shift of the maximum likely due to the presence of FL outside the ZL channels.

A very interesting result is that no intensity decrease in the ZL/1.5FL is observed, as could be expected as a consequence of the high amount and packing of the fluorenone molecules This effect could be justified by the presence of only FL molecules and hence, by the energy transfer between neighbor molecules of the same nature

6.1.8. CONCLUSIONS

All the techniques, adopted, revealed that the incorporation of different FL amount in ZL was successful. The results of thermogravimetric, IR, and X-ray diffraction analyses established that the maximum loading corresponds to 1.5 FL molecules per ZL unit cell. A thorough characterization of structural properties and energetics of this dye-zeolite systems has been accomplished by DFT-based modeling, which, besides supporting and strengthening experimental evidences, has proved once again its capability in providing information otherwise extremely difficult to access from the structural analysis. On the whole, the results here presented further highlight the relevance of the extraframework K^+ cations in stabilizing carbonyl-functionalized species inside ZL and in governing their organization.

APPENDIX B

Table 6.1.5.1. Experimental and refinement parameters for ZL and ZL/0.5FL, ZL/1.0FL and ZL/1.5FL composites.

Samples	**ZL**	**ZL/0.5FL**	**ZL/1.0FL**	**ZL/1.5FL**
Space Group	P6/m m m	P6/m m m	P6/m m m	P6/m m m
a (Å)	18.3795(4)	18.3860(6)	18.3940(6)	18.4211(7)
c (Å)	7.5281(2)	7.5228(3)	7.5203(3)	7.5117(4)
V (Å^3)	2202.4(1)	2202.4(1)	2203.5(1)	2207.5(2)
R_p (%)	2.8	3.0	2.9	3.1
R_{wp} (%)	3.8	4.2	4.2	4.3
R F2 (%)**	7.3	7.5	7.8	8.7
No. of variables	73	84	81	107
No. of observations	2211	1989	2211	1989
No. of reflections	944	726	946	729

Table 6.1.5.2. Atomic coordinates, occupancy factors and thermal displacement parameters for the structures of As synthetized ZL and ZL/0.5FL, ZL/1.0FL and ZL/1.5FL composites.

Atom	x/a	y/b	z/c	Occ.	Uiso
		ZL			
T1	0.0939(1)	0.3566(2)	0.5	1	0.0136(5)
T2	0.1646(2)	0.4978(1)	0.2093(2)	1	0.0136(5)
O1	0	0.2694(6)	0.5	1	0.0159(9)
O2	0.1616(2)	0.3233(5)	0.5	1	0.0159(9)
O3	0.2671(2)	0.5342(4)	0.2534(8)	1	0.0159(9)
O4	0.1019(3)	0.4127(3)	0.3241(5)	1	0.0159(9)
O5	0.4245(2)	0.8490(4)	0.2645(9)	1	0.0159(9)
O6	0.1452(4)	0.4762(4)	0	1	0.0159(9)
KB	0.33333	0.66667	0.5	1	0.016(3)
KC	0.5	0	0.5	1	0.037(3)
KD	0.3006(5)	0	0	0.804(2)	0.057(3)
WF	0.117(2)	0	0	0.42(1)	0.149(9)
WH	0.119(1)	0	0.371(2)	0.43(1)	0.149(9)
WI	0.257(1)	0.128(5)	0	0.88(1)	0.149(9)
WJ	0.162(1)	0.0814(7)	0.292(3)	0.44(1)	0.149(9)
WK	0	0	0.185(1)	0.25(2)	0.149(9)
		ZL/0.5FL			
T1	0.0933(3)	0.3583(3)	0.5	1	0.015(6)
T2	0.1660(2)	0.4994(2)	0.2107(4)	1	0.015(6)
O1	0	0.2746(8)	0.5	1	0.017(1)
O2	0.1653(4)	0.3308(9)	0.5	1	0.017(1)
O3	0.2641(3)	0.5284(7)	0.250(1)	1	0.017(1)
O4	0.1038(4)	0.4151(4)	0.3242(8)	1	0.017(1)
O5	0.4282(1)	0.8564(4)	0.266(1)	1	0.017(1)
O6	0.1457(7)	0.4777(6)	0	1	0.017(1)
KB	0.33333	0.66667	0.5	1	0.022(4)
KC	0.5	0	0.5	1	0.045(4)
KD	0.3020(6)	0	0	0.820(8)	0.067(4)
WH	0.158(3)	0	0.196(5)	0.313(7)	0.115(3)
C1	0.0251(4)	0.0125(2)	0.4060(7)	0.080(1)	0.175(5)
C2	0.1069(3)	0.0535(2)	0.4615(7)	0.080(1)	0.175(5)
C3/WJ	0.1694(3)	0.0847(1)	0.3337(1)	0.60(4)	0.175(5)
C4	0.1434(5)	0.0717(2)	0.1559(3)	0.080(1)	0.175(5)
C5	0.0594(4)	0.0297(2)	0.0957(2)	0.080(1)	0.175(5)
C6	0	0	0.3337(1)	0.50(3)	0.175(5)
C7	0.1978(4)	0.0989(2)	0	0.080(1)	0.175(5)
OFL/WI	0.2728(5)	0.1364(2)	0	0.89(1)	0.175(5)
		1.0ZL/ FL			
T1	0.0934(3)	0.3575(3)	0.5	1	0.012(5)
T2	0.1658(3)	0.4989(2)	0.2108(4)	1	0.012(5)
O1	0	0.2746(8)	0.5	1	0.016(1)
O2	0.1640(5)	0.3280(9)	0.5	1	0.016(1)
O3	0.2645(3)	0.5289(7)	0.248(2)	1	0.016(1)
O4	0.1022(5)	0.4168(4)	0.3298(8)	1	0.016(1)
O5	0.4263(2)	0.8525(4)	0.268(2)	1	0.016(1)
O6	0.1462(7)	0.4801(7)	0	1	0.016(1)
KB	0.33333	0.66667	0.5	1	0.016(2)
KC	0.5	0	0.5	1	0.034(2)
KD	0.3071(7)	0	0	0.871(9)	0.073(2)
C1	0.0287(3)	0.0143(2)	0.4079(6)	0.158(1)	0.197(5)
C2	0.1105(3)	0.0553(2)	0.4635(6)	0.158(1)	0.197(5)
C3/WJ	0.1707(2)	0.0854(1)	0.3306(1)	0.631(1)	0.197(5)
C4	0.1415(4)	0.0708(2)	0.1556(2)	0.158(1)	0.197(5)
C5	0.0575(4)	0.0287(2)	0.0957(2)	0.158(1)	0.197(5)
C6	0	0	0.2333(6)	1.00(4)	0.197(5)
C7	0.1961(4)	0.0980(2)	0	0.158(1)	0.197(5)
OFL/WI	0.2712(4)	0.1356(2)	0	0.81(2)	0.197(5)

		ZL/1.5FL			
T1	0.0943(4)	0.3587(3)	0.5	1	0.016(5)
T2	0.1667(3)	0.5004(3)	0.2100(4)	1	0.016(5)
O1	0	0.2770(8)	0.5	1	0.018(1)
O2	0.1640(5)	0.3281(9)	0.5	1	0.018(1)
O3	0.2650(4)	0.5299(7)	0.253(2)	1	0.018(1)
O4	0.1031(5)	0.4185(4)	0.3303(9)	1	0.018(1)
O5	0.4283(2)	0.8567(4)	0.269(2)	1	0.018(1)
O6	0.1457(8)	0.4791(7)	0	1	0.018(1)
KB	0.33333	0.66667	0.5	1	0.016(3)
KC	0.5	0	0.5	1	0.032(3)
KD	0.3127(6)	0	0	0.845(9)	0.085(3)
		FL			
C1	0.0312(3)	0.0156(8)	0.4095(5)	0.080(1)	0.17(4)
C2	0.1134(4)	0.0567(2)	0.4634(5)	0.080(1)	0.17(4)
C3/WJ	0.1718(6)	0.0859(3)	0.3268(4)	0.43(4)	0.17(4)
C4	0.1409(4)	0.0704(6)	0.1550(2)	0.080(1)	0.17(4)
C5	0.0570(6)	0.0285(3)	0.0960(6)	0.080(1)	0.17(4)
C6	0	0	0.2362(2)	0.50(3)	0.17(4)
C7	0.1959(4)	0.0979(5)	0	0.08(1)	0.17(4)
OFL/WI	0.2709(3)	0.1355(4)	0	0.58 (1)	0.17(4)
		FL'			
C'1	0.0999(6)	0.0499(5)	0.3306(4)	0.164(1)	0.17(4)
C'2	0.1261(9)	0.1261(9)	0.4237(7)	0.164(1)	0.17(4)
C'3	0.2033(2)	0.0513(5)	0.3430(4)	0.082(1)	0.17(4)
C'4	0.2085(5)	0.1460(5)	0.1615(6)	0.082(1)	0.17(4)
C'5	0.1322(3)	0	0.0928(2)	0.164(1)	0.17(4)
C'6	0.1130(5)	0.0565(6)	0.1471(3)	0.164(1)	0.17(4)
C'7	0.258(1)	0.0978(3)	0	0.082(1)	0.17(4)
O'FL	0.325(1)	0.1625(4)	0	0.164(1)	0.17(4)

Table 6.1.5.3. Framework bond distances for ZL and ZL/0.5 FL, ZL/1.0 FL and ZL/1.5 FL composites and extraframework bond distances < 3.2 Å for ZL.

	ZL	ZL/0.5FL	ZL/1.0FL	ZL/1.5FL
T1-O1	1.635(4)	1.632(4)	1.630(3)	1.633(4)
O2	1.632(4)	1.637(3)	1.638(3)	1.642(4)
O4 [X2]	1.635(3)	1.634(3)	1.636(2)	1.639(3)
average	**1.634**	**1.634**	**1.635**	**1.638**
T2-O3	1.643(4)	1.633(3)	1.636(3)	1.640(4)
O4	1.642(4)	1.636(3)	1.640(3)	1.643(4)
O5	1.624(4)	1.631(5)	1.630(6)	1.634(6)
O6	1.624(3)	1.632(3)	1.624(3)	1.625(3)
average	**1.633**	**1.633**	**1.633**	**1.640**
KB-O3 [x6]	2.884(9)			
KC-O5 [x4]	2.985(8)			
KD-O4 [x4]	3.146(6)			
O6 [x2]	3.033(5)			
WI [x2]	2.848(6)			
WF-WF [x2]	2.13(3)			
WH [x2]	2.81(2)			
WI [x2]	2.47(2)			
WJ [x4]	2.56(2)			
WK [x2]	2.60(3)			
WH-O1	2.98(1)			
WF	2.81(2)			
WH[x2]	2.20(2)			
WH[x2]	2.91(3)			
WH	1.91(4)			
WJ[x2]	1.425(8)			
WJ[x2]	2.83(2)			
WK	2.60(2)			
WI-WF[x2]	2.47(2)			
WJ[x2]	2.675(9)			
WJ-O2	3.06(1)			
WF[x2]	2.56(2)			
WH[x2]	1.425(8)			
WH[x2]	2.83(2)			
WI	2.675(9)			
WJ [x2]	2.59(2)			
WJ	3.12(5)			
WK	2.69(2)			
WK-WF [x6]	2.60(3)			
WH [x6]	2.60(2)			
WJ [x6]	2.69(2)			
WK	2.85(2)			

Table 6.1.5.4. Extraframework bond distances < 3.2 Å for ZL/0.5FL, ZL/1.0FL and ZL/1.5FL composites.

	ZL/0.5FL	ZL/1.0FL		ZL/1.5FL
KB-O3 [x6]	2.89(1)	2.90(1)		2.86(1)
KC-O5 [x4]	2.89(1)	2.93(1)		2.87(1)
KD-O4 [x4]	3.158(4)	3.166(4)		3.140(4)
O6 [x2]	3.012(6)	2.983(7)		2.893(7)
OFL/WI[x2]	2.809(6)	2.864(7)	**O'FL[x2]**	2.887(5)
WH [x2]	3.008(8)	--	**OFL/WI[x2]**	2.957(8)
WH-O1	2.832(4)	--	**C7'[x2]**	2.466(9)
C2 [x2]	2.64(4)		**C4'[x2]**	2.948(9)
C2 [x2]	3.11(4)	--	**OFL/WI-C6'[x2]**	2.56(3)
C5 [x2]	2.29(4)	--	**C4'[x4]**	1.64(1)
C5 [x2]	3.18(4)	--	**C4[x2]**	2.20(3)
C5 [x2]	3.07(4)	--	**C5'[x4]**	2.45(3)
C4 [x2]	3.01(4)	--	**OFL'**	1.07(4)
C4 [x2]	1.53(3)	--	**C3'[x4]**	2.87(1)
WH [x2]	2.94(4)	---	**C7'[x2]**	0.78(7)
WH	2.89(8)	--	**C3/WJ[x2]**	2.81(1)
OFL[x2]	2.74(3)	--	**C7**	1.21(4)
C3/WJ[x2]	1.83(3)	--	**C'7**	0.60(4)
C1[x2]	3.07(4)	--	**C3/WJ-O2**	3.12(6)
C7[x2]	2.15(3)		**C3'[x2]**	1.31(4)
OFL/WI -C4 [x2]	2.37(1)	--	**C3'[x2]**	2.52(2)
C5[x2]	3.15(2)	--	**C3'[x2]**	2.82(4)
WH[x4]	2.73(1)	--	**C1[x2]**	2.95(5)
C3[x2]	3.00(1)	2.96(2)	**C1**	2.47(6)
C7	1.19(2)	1.20(2)	**C2'**	2.02(5)
WJ/C3-O2	2.85(2)	2.84(1)	**C2' [x2]**	2.95(5)
C4	1.39(2)	1.39(3)	**C'2**	2.83(5)
C4[x2]	2.85(2)	2.84(3)	**C2[x2]**	3.04(5)
C2[x2]	2.58(2)	2.59(3)	**C2**	2.02(6)
C2[x2]	2.96(2)	3.03(2)	**C2**	2.50(6)
C2[x2]	3.19(2)	3.20(2)	**C1'[x2]**	2.58(4)
C2	2.37(2)	2.34(3)	**C1'[x2]**	1.45(5)
C2	3.02(2)	3.00(3)	**C4'[x2]**	2.60(1)
C5[x2]	2.96(2)	2.98(4)	**C4'[x2]**	1.65(6)
C5	2.50(2)	2.52(3)	**C4[x2]**	2.66(3)
OFL/WI	3.17(2)	2.95(3)	**C4**	1.39(6)
C3/WJ[x2]	2.70(1)	2.71(3)	**C5'[x2]**	2.83(6)
C3/WJ	2.50(2)	2.55(3)	**C5[x2]**	2.72(5)
C5	2.50(2)	2.52(3)	**C5**	2.19(5)
C5[x2]	2.96(2)	2.97(3)	**C5**	3.14(6)
C1[x2]	2.55(2)	2.59(4)	**C5**	2.84(5)
C1[x2]	2.82(2)	2.84(3)	**C6'[x2]**	2.57(4)
C1	1.38(2)	1.39(3)	**C6'**	1.68(5)
C1	1.83(2)	1.82(3)	**C7'[x2]**	2.24(5)
C7	2.55(2)	2.52(2)	**O'FL**	2.89(5)
WH	1.82(2)	--		
C6	2.81(2)	2.82(3)		

6.2. ZL/TB-DXP COMPOSITES

6.2.1. Synthesis of ZL/tB-DXP composites

The loading of the neutral dye tB-DXP was performed at the Department of Chemistry at the University of Fribourg, following their ratified procedure descripted in ref [10].
In a typical experiment, 100 mg of ZL and 4.9 mg of tB-DXP (p = 0.7) [11] were weighed into a 25 mL round-bottom flask. Dichloromethane was then added, and the mixture was sonicated for 2 min to dissolve the dye and ensure a good dispersion of the zeolite. The solvent was then evaporated on a rotary evaporator (40 °C, 600 mbar), thus leading to a homogeneous coating of the zeolite surface with tB-DXP. The coated zeolite was removed from the flask and transferred into an agate mortar, where it was ground. The powder was then put into a small glass ampule and dried on a vacuum line for 24 h at a pressure of 2×10^{-2} mbar. The ampule was then sealed off under vacuum and put into a rotating oven. The gas phase insertion process took place over 4 days at 260 °C. Once this process was completed, the ampule was removed from the heating source and cooled to RT. The ampule was then opened and the colored powder was washed three times with 20 mL of dichloromethane until the supernatant was colorless.
Several samples at different nominal loadings were prepared and preliminary UV-Vis spectra [10] indicated that the maximum loading corresponds to p= 0.5 [11].
This high loaded composite was investigated as reported in the following sections and was the most suitable for XRPD structure refinement.

6.2.2. TGA-MSEGA

The effective tB-DXP and water content of the ZL/tB-DXP composite were determined by TGA-MSEGA. During the analysis the intensity changes of 7 species (m/z = 16 (CH_4), 18 (H_2O), 28 (CO), 30 (CH_3CH_3, NO), 44 and 45 (CO_2) 78 (C_6H_6), 76 (N2O3)) were followed as function of temperature.
Figure 6.2.2.1 shows the TG (a) and DTG curves (b) as a function of temperature for the as-synthesized ZL, pure crystalline tB-DXP and ZL/tB-DXP composite.

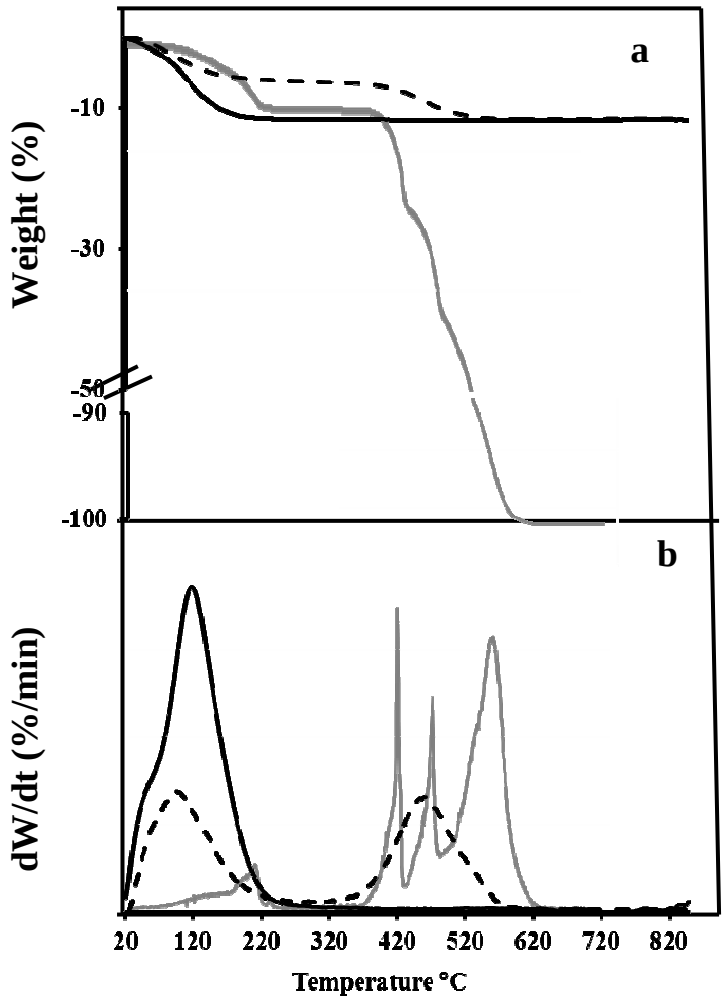

Figure 6.2.2.1. TGA (a) and DTG curves (b) for ZL (black solid curve), crystalline dye tB-DXP (grey solid curve) and the ZL/tB-DXP (dashed black line), composite.

As shown in Figure 6.2.2.1 and Table 6.2.2.1, in the composite the water loss temperature slightly decreases respect to ZL, as a consequence of the tB-DXP penetration, the weight loss is 5.9 % about, corresponding to 9.4 water molecules p.u.c. The tB-DXP release in the composite occurs in one step in the temperature range (320-570°C) similar to that of the pure dye, corresponding to a weight loss of 5.8 % equal to 0.23, molecules of tB-DXP molecules p.u.c. tB-DXP inside the zeolite is released as CH_3CH_3, CO_2 as revealed by the mass spectrometry

Table 6.2.2.1. Temperature of water and tB-DXP weight loss and number of molecules, determined by TGA-MSEGA, compared with those obtained by the Rietveld refinement for the ZL/tB-DXP composites.

Sample	Water loss T (°C)	Water wt. %	Water molecules (TGA)	Water molecules (structure refinement)	tB-DXP loss T(°C)	tB-DXP wt.%	tB-DXP molecules	tB-DXP molecules (structure refinement)
ZL	110	11.9	18	18	-	-	-	---
ZL/tB-DXP	105	5.9	9.4	8.5	470	5.8	0.23	0.25

6.2.3. TRANSMISSION FT-IR

An FT-IR in situ investigation was carried out on the dehydration process of the ZL/tB-DXP composite to verify the role of the water molecules on the organization of the tB-DXP molecules and on the host-guest interactions that make stable this composite. The material was keep at RT under vacuum one night (dashed-dot orange line in Fig. 6.2.4.1) and then further degassed at 80 (dashed orange line), 120 (dotted orange line) and 200°C (solid orange line) in order to release all the water present in the zeolite channels**.**

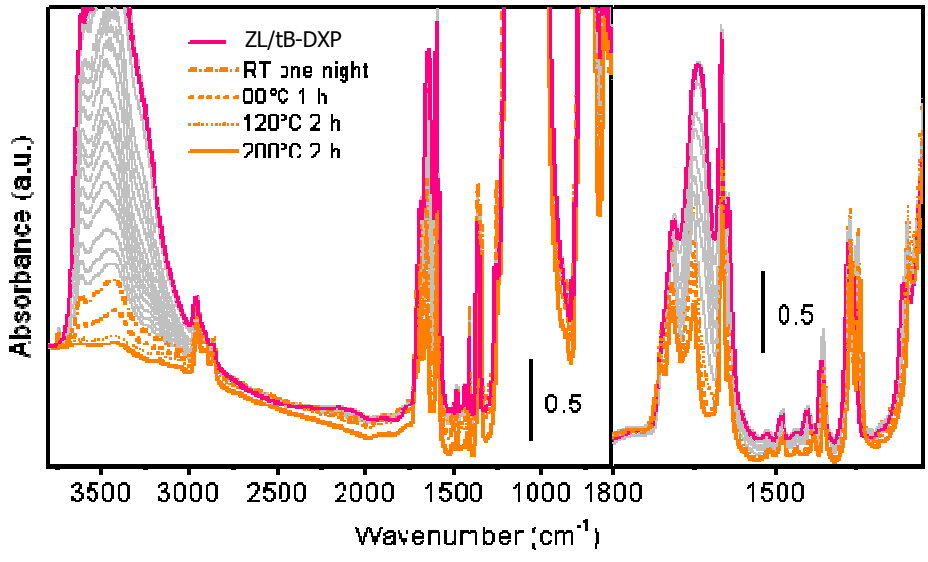

Figure 6.2.3.1. FT-IR spectra as obtained in air (pink line), and after treatment in vacuum at 200°C for 2 h (orange line) for the samples ZL/tB-DXP. Left 3800-1800 cm-1range; right 1300-1800 cm-1 region.

The comparison between the spectrum of the composite and that obtained after degassing for one night, pink and solid orange lines respectively in Figure 6.2.3.1 suggests some kind of interaction between the dye and the water molecules inside the channel. In fact we can see that the C-H stretching bands (at about 3000 cm^{-1}) and all the dye vibrational signals (1800-1200 cm^{-1}) are strongly perturbed during the water removal.

6.2.4. ATR-IR ANALYSIS

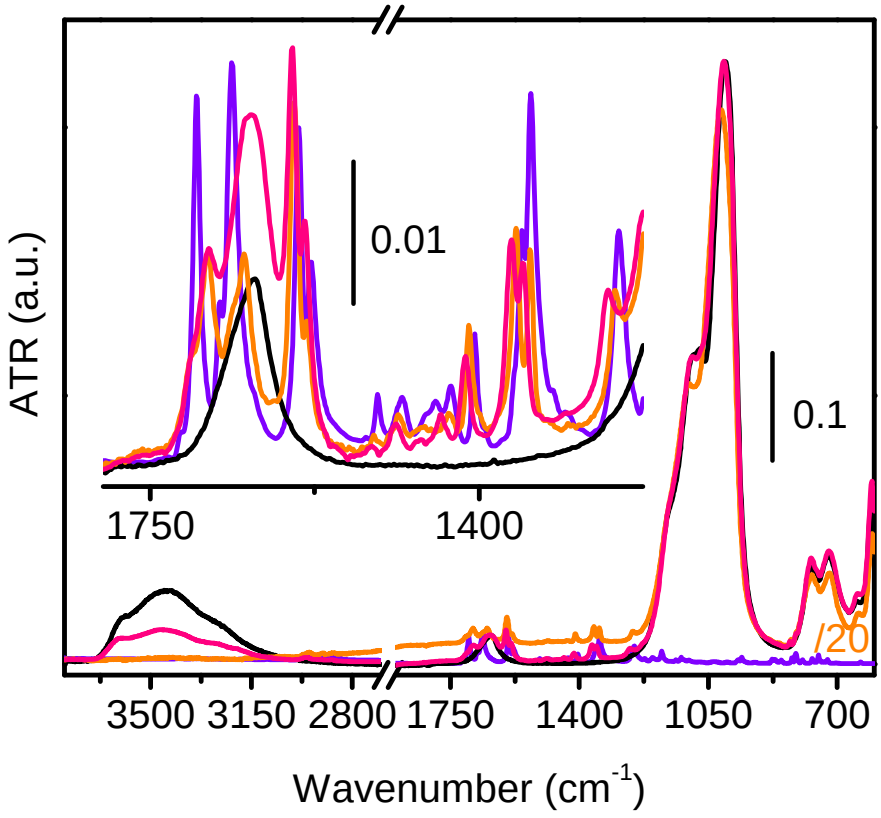

Figure 6.2.4.1 ATR-IR spectra collected in the 3800-650 cm^{-1} range for the pure dye tB-DXP (violet line), ZL/tB-DXP (pink line) and after the treatment in vacuum at 200°C for 2 h (orange line). ZL (black) is also reported for comparison.. The inset reports the zoom of the 1750-1550 region.

The ATR-IR spectra (Fig. 6.2.4.1) of the hydrated and dehydrated ZL/tB-DXP composite form are compared with that collected on the ZL and the pure dye.

The decrease in intensity of the band centered at 3450 cm^{-1} is related to the lower water content in the ZL/tB-DXP (pink line). For what concerns the bands of the dye, all of them results to be shifted after the formation of the composite: in particular peaks at around cm^{-1}, 1701, 1677 and 1662 cm^{-1} are blue shifted whereas all other signal are red shifted. This is a strong indication that the whole molecular structure of tB-DXP is perturbed by the interaction with the hosting material.

The comparison of the peaks of the dye in the hydrated and dehydrated form of the composite indicates that the removal of water causes a decrease in the shift of the vibrational models of the dye suggesting less strong interactions between the dye and ZL and a possible role of the water molecules**.**

This fact is also evidenced by a change of the color of the composite, from magenta to orange in the dehydrated form that causes differences also in the absorption properties as we will see in the paragraph 6.2.6.

6.2.5.STRUCTURE REFINEMENT

In Figure 6.2.5.1 the comparison between the XRPD patterns collected on ZL and the ZL/tB-DXP composite is shown. The most significant differences are in the intensity of the diffraction peaks in the low 2Θ angle region, which is correlated to dye encapsulation.

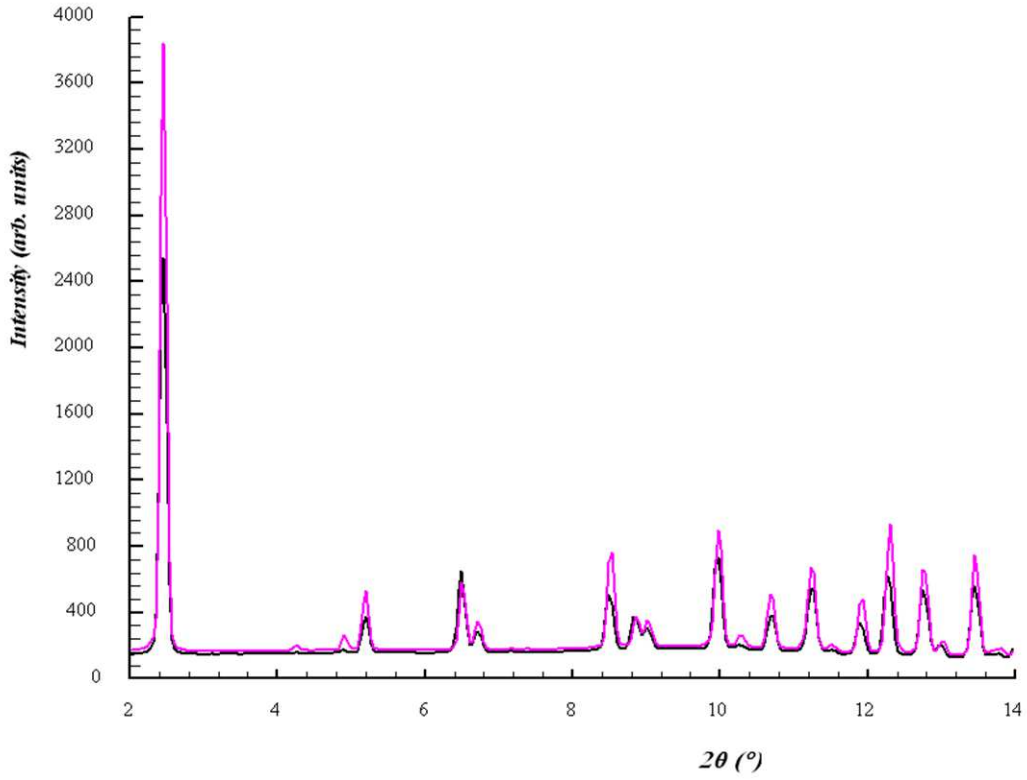

Figure 6.2.5.1. Comparison of the intensity of the patterns of the ZL (fuxia line) and the ZL/tB-DXP composite (black line).

A further XRPD pattern (CuKα), collected in a short range of low 2theta range for 20 hours of the composite, (Fig. 6.2.5.2) did not reveal superstructure reflections as could have been expected by an ordered distribution of a molecule like tB-DXP whose length is about three times the *c* axis of zeolite L.

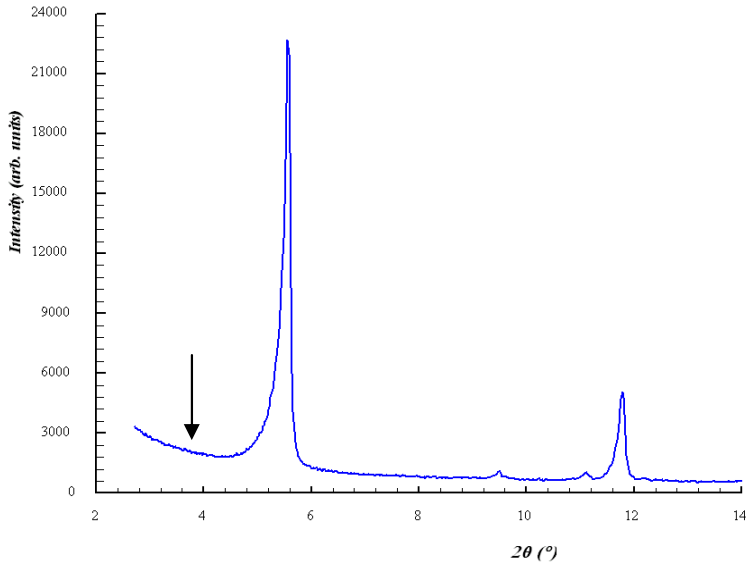

Figure 6.2.5.2. XRPD pattern of the composite collected with conventional diffractometer in the 2.5-14 2Θ range (the arrow indicates the position of the superstructure reflection following the Bragg law).

The structure refinement of the ZL/tB-DXP composite revealed a clear increase of *a* and a decrease of *c* parameters with respect to the original material (Table 6.2.5.1, Appendix C). These minor variations in the unit cell parameters can be justify by the slight deformations of both the channels (12MR and 8MR) running parallel to *c* axis (see Fig. 6.2.5.2).

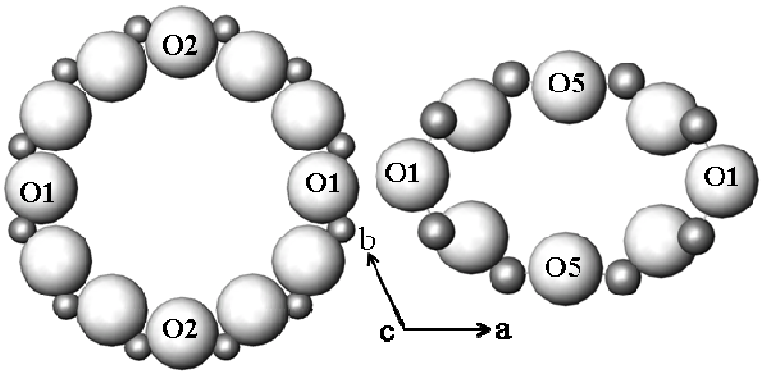

Sample	12MR		8MR //c	
	O1 O1	O2 O2	O1 O1	O5 O5
ZL	10.10	10.43	8.29	4.87
ZL/tB-DXP	10.08	10.41	8.34	4.68

Figure 6.2.5.2. Dimensions of the 12MR and 8MR channels parallel to [001] of ZL and ZL/tB-DXP.

Because the width of tB-DXP molecule (7.0 · 22~ Å) is close to the pore opening of the large 12-membered ring channel of ZL (7.4 x 7.7 Å) it fits tightly into the channel. This tight fit along with the length of the molecule limit rotational disorder within the channel. The tB-DXP molecule localization was obtained by analysing the difference Fourier map focusing on the large 12-membered ring channel. The refinements revealed the presence of 0.25 molecules per unit cell, in good agreement with the indications of the TGA analysis (Table 6.2.2.1 in Appendix C). Three symmetrically equivalent, partially occupied, sites were found for the atoms of tB-DXP. These sites are placed at the center of the channel and lie on the mirror planes parallel to *c* axis (Figs. 6.2.5.3 a, b)

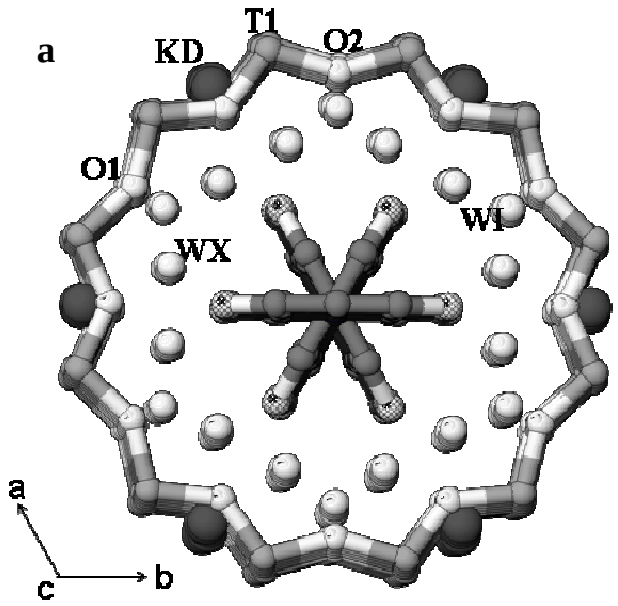

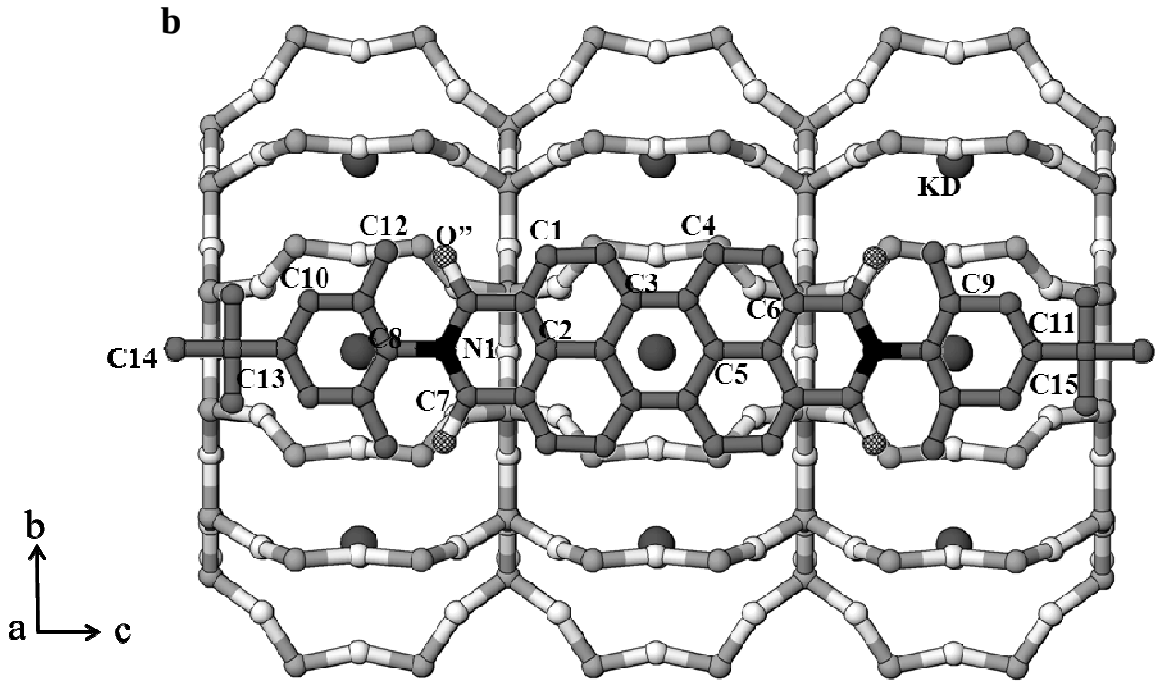

Figure 6.2.5.3. Projection of the ZL/tB-DXP composite structure along [001] (a). three unit cells along [100] (b). Only one dye molecule is shown for sake of clarity.

The distribution of water molecules differs from that of ZL. In particular 8.5 water molecules/u.c. in ZL/tB-DXP composite were found distributed over only two independent, partially occupied, sites. The first, named WI, correspond to that present in ZL and the second is a new site WX (see Table 6.2.5.2 6.2.5.4, Appendix C and Fig. 6.2.5.3 a).

Observing the Table 6.2.5.4 in Appendix B, two different kinds of interaction can be invoked in the stability of the ZL/tB-DXP composite. The first one involve the C1—O1 distance (2.95 Å) (Table 6.2.4.4, Appendix C) that is in line with the literature data, where C--O distances of 2.8–3.3 Å [12, 13, 14] are reported, indicating a CH--O hydrogen bondg between the dye molecules and the ZL framework. The second interaction is represented by the carbon atom C12 with the water molecule WI in turn bonded to the KD sites (Table 6.2.5.4, Appendix C), thus suggesting a weak interaction of the dye with the K^+ cation.

An important point that has to be remembered is that the t- butyl functional end-substituents group of the molecule, have a greater degree of freedom than the perylene core, in fact they can rotate respect to rigid central part of the molecule contributing to increase the disorder of this final part of the molecule. This can give rise to different distributions of the molecule

within the channels of the zeolite. Various models of the tB-DXP distribution based on our structural data are shown in Figure 6.2.5.4. The internal surface of the ZL 12MR channels exhibits preferred positions (WI—K^+ and O1) for bonding tB-DXP molecule. As a consequence ZL channel cannot be filled by continuous stackings of tB-DXP along *c*, as if the tB-DXP molecules separation would be dictated only by van der Waals contacts. On the contrary, at least an empty cell between two consecutive molecules is required.

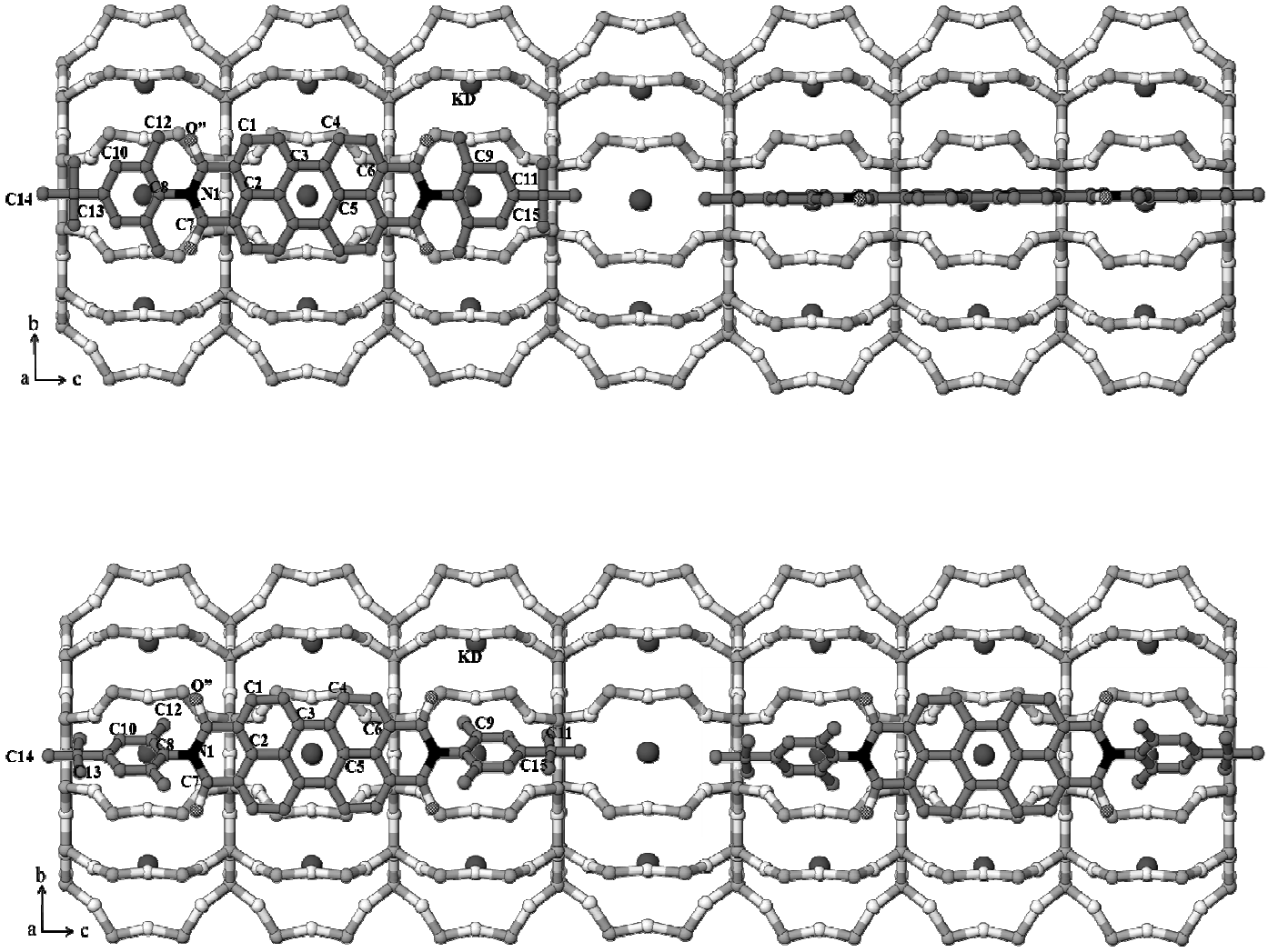

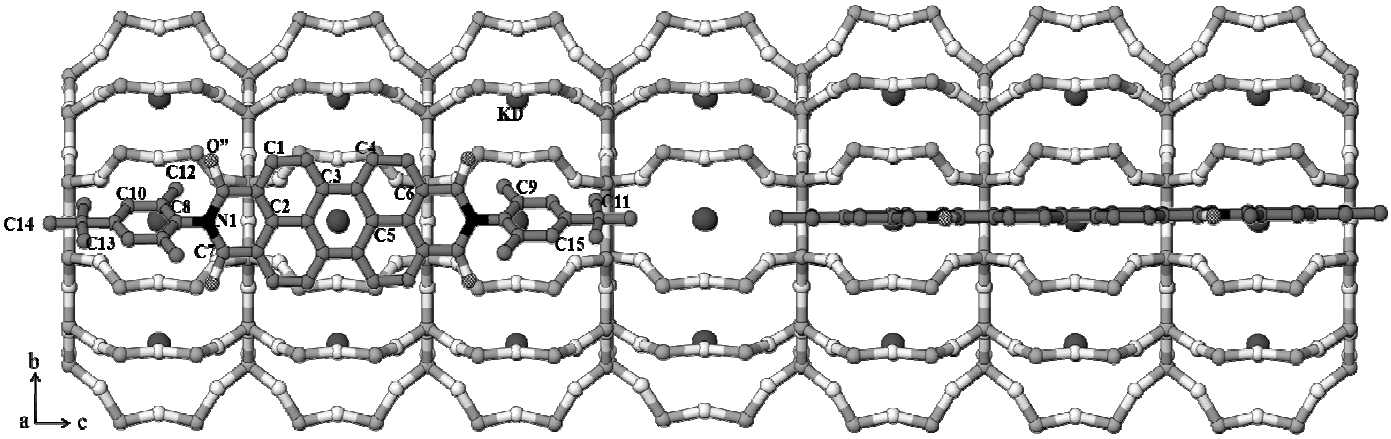

Figure 6.2.5.4. Models of the arrangement of the tB-DXP, viewed along the ZL 12MR channel. For sake of clarity only one of the three symmetrical equivalent molecules is represented in each dwaw and the water molecules are omitted.

6.2.6. OPTICAL SPECTROSCOPY

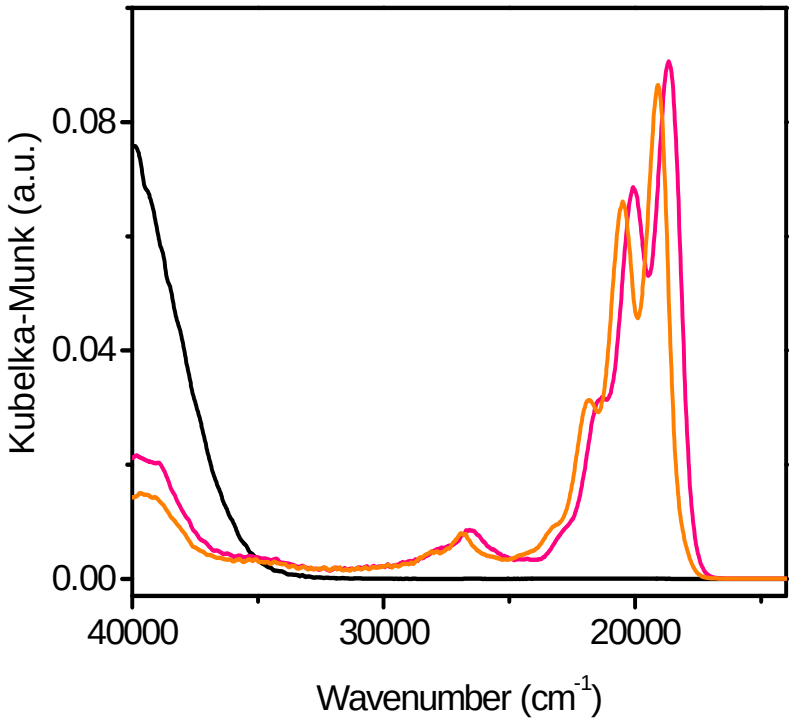

Figure 6.2.6.1. DR-UV-Vis spectrum of ZL /tb-DXP in air (pink line) and after treatment in vacuum at 200°C for 1 h (orange line). The samples have been diluted 1:20 in weight in teflon.

As anticipated in the 6.2.3 paragraph, a change of the color of the composite, from magenta to orange in the dehydrated form was observed. The corresponding DR-UV-Vis spectra reported in Figure 6.2.6.1 shows clearly that the whole absorption spectrum of the composite undergoes a blue shift as the result of the water removal.

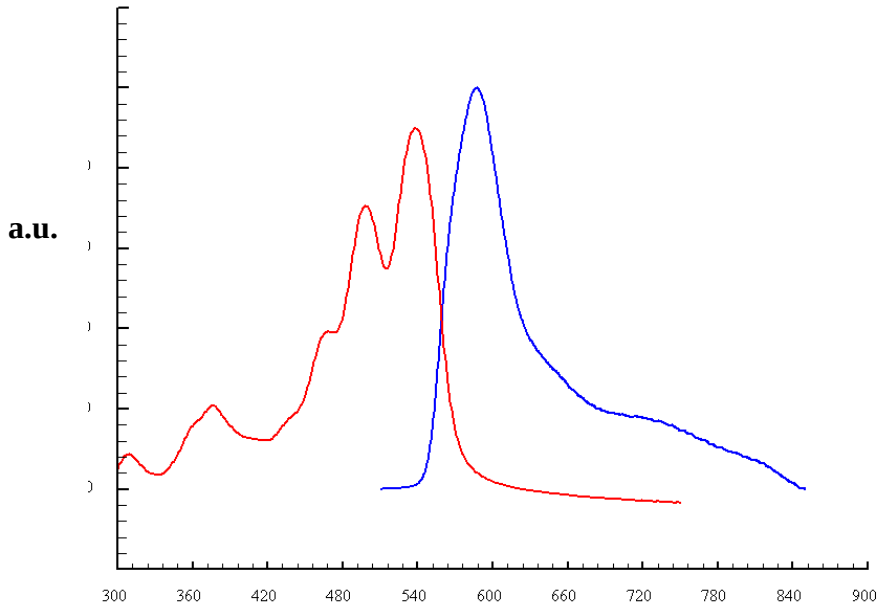

Figure 6.2.6.1 Superimposition of the absorption (red line) and florescence spectra (blue line) of the hydrated ZL/tB-DXP composites.

The Figure 6.2.6.1. shows the absorption and emission spectra of the hydrated form of the studied ZL/tB-DXP composite: as one can see the shape of the two spectra are very different from each other. In fact while the absorption spectrum of tB-DXP, in the zeolite, retains its original form, (Fig.4.1.2.2.4), the fluorescence spectrum shows important changes, form that could hardly be identified to originate from tB-DXP.

Differently from what one might think, this change in the emission spectrum is not caused by interactions of the dye with the host, aggregation or self-quenching of the dye in the channels, but by another mechanism, called extra-particle self-absorption [10]. At this point is important to stress that, notwithstanding the high loading of the tB-DXP, the formation of aggregates inside the zeolite is still negligible.

This is an unexpected result that confirm the goodness of the synthesis method of an antenna system, that have to contain a large concentration of donors, for example tB-DXP, with only few acceptor molecules.

6.2.7. CONCLUSIONS

Also in this case a multi-technique approach was used to investigate the properties of the ZL/tB-DXP composite and revealed the successful encapsulation of the dye, with a maximum possible loading equal to 0.23 molecules p.u.c.

Infrared measurement has revealed that the dye vibrational signals are strongly perturbed during the water removal suggesting the presence of some interaction between the dye and the water molecules inside the ZL channel. In fact, the structural refinement showed that the dye interacts with the zeolitic framework through C--O bond and that the carbonyl group of the dye is not in direct interaction with the potassium, as seen for the fluorenone, but their interaction is mediated by water.

Another important aspect that have to be highlighted is that the t-butyl end- substituents in the molecule really act as spacers, facilitating a packing without the formation of aggregates.

APPENDIX C

Table 6.2.5.1. Experimental and refinement parameters for ZL and ZL/tB-DXP composite.

Samples	**ZL**	**ZL/tB-DXP**
Space Group	P6/m m m	P6/m m m
a (Å)	18.3795(4)	18.4262(5)
c (Å)	7.5281(2)	7.5211(3)
V (Å^3)	2202.4(1)	2211.4(1)
R_p (%)	2.8	3.6
R_{wp} (%)	3.8	5.0
R F2 (%)**	7.3	9.4
No. of variables	73	65
No. of servations	2211	2225
No. of reflections	944	948

Table 6.2.5.2. Atomic coordinates, occupancy factors and thermal displacement parameters for the structures of ZL and ZL/tB-DXP composite.

Atom	x/a	y/b	z/c	Occ.	Uiso
			ZL		
T1	0.0939(1)	0.3566(2)	0.5	1	0.0136(5)
T2	0.1646(2)	0.4978(1)	0.2093(2)	1	0.0136(5)
O1	0	0.2694(6)	0.5	1	0.0159(9)
O2	0.1616(2)	0.3233(5)	0.5	1	0.0159(9)
O3	0.2671(2)	0.5342(4)	0.2534(8)	1	0.0159(9)
O4	0.1019(3)	0.4127(3)	0.3241(5)	1	0.0159(9)
O5	0.4245(2)	0.8490(4)	0.2645(9)	1	0.0159(9)
O6	0.1452(4)	0.4762(4)	0	1	0.0159(9)
KB	0.33333	0.66667	0.5	1	0.016(3)
KC	0.5	0	0.5	1	0.037(3)
KD	0.3006(5)	0	0	0.804(2)	0.057(3)
WF	0.117(2)	0	0	0.42(1)	0.149(9)
WH	0.119(1)	0	0.371(2)	0.43(1)	0.149(9)
WI	0.257(1)	0.128(5)	0	0.88(1)	0.149(9)
WJ	0.162(1)	0.0814(7)	0.292(3)	0.44(1)	0.149(9)
WK	0	0	0.185(1)	0.25(2)	0.149(9)
			ZL/tB-DXP		
T1	0.0930(3)	0.3569(3)	0.5	1	0.0153(8)
T2	0.1666(3)	0.4993(2)	0.2115(4)	1	0.0153(8)
O1	0	0.2737(9)	0.5	1	0.016(1)
O2	0.1633(4)	0.3266(9)	0.5	1	0.016(1)
O3	0.2623(3)	0.5247(7)	0.261(1)	1	0.016(1)
O4	0.1021(5)	0.4149(5)	0.3279(9)	1	0.016(1)
O5	0.4266(2)	0.8533(6)	0.280(1)	1	0.016(1)
O6	0.1433(6)	0.4769(6)	0	1	0.016(1)
KB	0.33333	0.66667	0.5	1	0.018(4)
KC	0.5	0	0.5	1	0.034(4)
KD	0.3069(6)	0	0	0.767(7)	0.044(4)
C1	0.129	0	0.38	0.0864	0.0825
C2	0	0	0.380069	0.2492	0.0825
C3	0.069586	0	0.093006	0.0863	0.0825
C4	0.1321	0	0.188	0.0864	0.0825
C5	0	0	0.188607	0.2485	0.0825
C6	0.065244	0	0.4733	0.0864	0.0825
C7	0.0665	0	0.66	0.0864	0.0825
N1	0	0	0.75	0.2492	0.0825
C8	0	0	0.93	0.2492	0.0825
C9	0.06752	0	0.99	0.0864	0.0825
C10	0.06752	0	1.198	0.0864	0.0825
C11	0	0	1.465	0.2492	0.0825
O''	0.132	0	0.73	0.0864	0.0825
C12	0.135	0	0.93	0.0863	0.0825
C13	0.074	0	1.45	0.2491	0.0825
C14	0	0	1.64	0.2491	0.0825
C15	0	0	0.72	0.2491	0.0825
WX	0.214(1)	0.053(1)	0	0.477(8)	0.14(4)
WI	0.274(2)	0.137(1)	0	0.45(1)	0.08(2)

Table 6.2.5.3. Framework bond distances for ZL and ZL/tB-DXP composite and extraframework distances < 3.2 Å for ZL sample.

	ZL	ZL/tB-DXP
T1-O1	1.635(4)	1.630(7)
O2	1.632(4)	1.650(6)
O4 [X2]	1.635(3)	1.632(6)
average	**1.634**	**1.636**
T2-O3	1.643(4)	1.627(6)
O4	1.642(4)	1.659(7)
O5	1.624(4)	1.661(6)
O6	1.624(3)	1.646(4)
average	**1.633**	**1.648**
KB-O3 [x6]	2.884(9)	
KC-O5 [x4]	2.985(8)	
KD-O4 [x4]	3.146(6)	
O6 [x2]	3.033(5)	
WI [x2]	2.848(6)	
WF-WF [x2]	2.13(3)	
WH [x2]	2.81(2)	
WI [x2]	2.47(2)	
WJ [x4]	2.56(2)	
WK [x2]	2.60(3)	
WH-O1	2.98(1)	
WF	2.81(2)	
WH[x2]	2.20(2)	
WH[x2]	2.91(3)	
WH	1.91(4)	
WJ[x2]	1.425(8)	
WJ[x2]	2.83(2)	
WK	2.60(2)	
WI-WF[x2]	2.47(2)	
WJ[x2]	2.675(9)	
WJ-O2	3.06(1)	
WF[x2]	2.56(2)	
WH[x2]	1.425(8)	
WH[x2]	2.83(2)	
WI	2.675(9)	
WJ [x2]	2.59(2)	
WJ	3.12(5)	
WK	2.69(2)	
WK-WF [x6]	2.60(3)	
WH [x6]	2.60(2)	
WJ [x6]	2.69(2)	
WK	2.85(2)	

Table 6.2.5.4. Extraframework bond distances < 3.2 Å for ZL/tB-DXP composite.

	ZL/tB-DXP
KB-O3 [x6]	2.88(1)
KC-O5 [x4]	2.88(1)
KD-O4 [x4]	3.130(9)
O6 [x2]	2.89(1)
WX[x2]	2.36(9)
WI[x2]	2.895(6)
C12[x2]	3.224(9)
WX-KD	2.36
C1 [x2]	3.172
WX	1.69(13)
WX	1.99(9)
C3[x2]	2.44(5)
C3[x2]	2.91
C4[x2]	1.94(5)
C4[x2]	2.93
WI	1.34(7)
WI	3.01(6)
C9[x2]	2.37(5)
C9[x2]	2.85
C12[x2]	2.62(5)
C12[x2]	1.39
O''-O1	3.12(1)
WX[x2]	2.42(6)
WI-KD[x2]	2.89
WX	1.34(7)
WX[x2]	3.02(6)
C4[x4]	2.89
C12x4]	2.6
C1-O1	2.95(1)

6.3. ZL/Th COMPOSITES

6.3.1. Synthesis of ZL/Th composites

Thionine incorporation was carried out at the Department of Chemistry at the University of Fribourg, by ion exchange [14, 15]. An amount of 60 mg of ZL powder was treated in $3.3.10^{-4}$ M aqueous thionine acetate solution ($C_{12}H_9N_3S \bullet C_2H_4O_2$, Aldrich, 90%) at 80 °C for 3 days in a sealed ampoule. After ion exchange, the blue colored powder was extensively washed, three times with distilled water and three times with ethanol, to remove possible adsorbed molecules on the ZL surface. Following this procedure two composites with different Th loading were synthetized with p= 0.2 and p= 0.5 [11].

6.3.2. TGA-MSEGA

Thionine-loaded ZL and the water content were determined by TGA. During the analysis the intensity changes of 8 species (m/z = 18 (H_2O), 44 (CO_2), 45 (CO_2) 45.88 (NO_2), 51.87 (C_4H_4), 63.84(SO_2), 75.75 (N_2O_3), 78 (C_6H_6)) were followed as a function of temperature.

Figure 6.3.2.1 shows the TG (a) and DTG curves (b) for the ZL, pure Th, and the two composites.

In both samples the Th release occurred in one wide step in the 320-550°C range and,

on the basis of the mass spectrometry results, we observed that Th is released as CO_2 m/z=44 and 45, NO_2 and SO_2. The weight losses corresponding to the encapsulated thionine are 1.5% and 2.7 %, resulting in 0.15 and 0.27 p.u.c. Th molecules in the two composites hereafter labelled as ZL/0.15Th and ZL/0.27Th (Table 6.3.2.1). These results are perfectly in agreement with the data reported in [15] where the same value for the maximum exchange degree of thionine inside a potassium zeolite L is reported.

Therefore we can assume that 0.27 molecules per unit cell represent the maximum thionine loading in the ZL channels.

In the two samples (Fig. 6.3.2.1 and Table 6.3.2.1), as a consequence of the water displacement due to the dye penetration, the weight losses relative to water are 10 % and 9.5% for ZL/0.15Th and ZL/0.27Th composites respectively corresponding to 15.7 an 14.9 molecules per u.c.

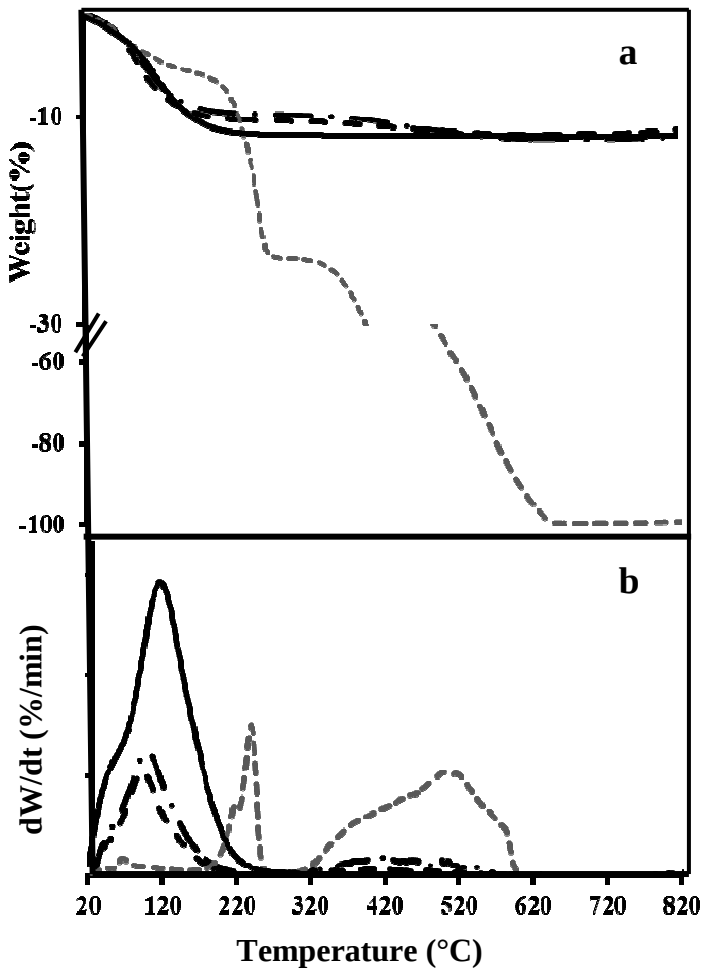

Figure 6.3.2.1. TGA (a) and DTG curves (b) for ZL (black solid curve), crystalline dye thionine (dashed grey curve), ZL/0.15Th (dashed black line) and ZL/0.27Th (dashed-dotted black line) composites.

Table 6.3.2.1. Temperature of water and thionine weight loss and number of molecules (water and Th), determined by TGA-MSEGA, compared with those obtained by the structure refinement for the ZL/Th composites.

Sample	Water loss T (°C)	Water wt. %	Water molecules (TGA)	Water molecules (structure refinement)	Th loss T(°C)	Th wt.%	Th molecules
ZL	110	11.9	18	18	-	-	-
ZL/0.15Th	102	10.0	15.7	15.9	320-590	1.5	0.15
ZL/0.27Th	100	9.5	14.9	14.8	320-590	2.7	0.27

6.3.3. ATR-IR ANALYSIS

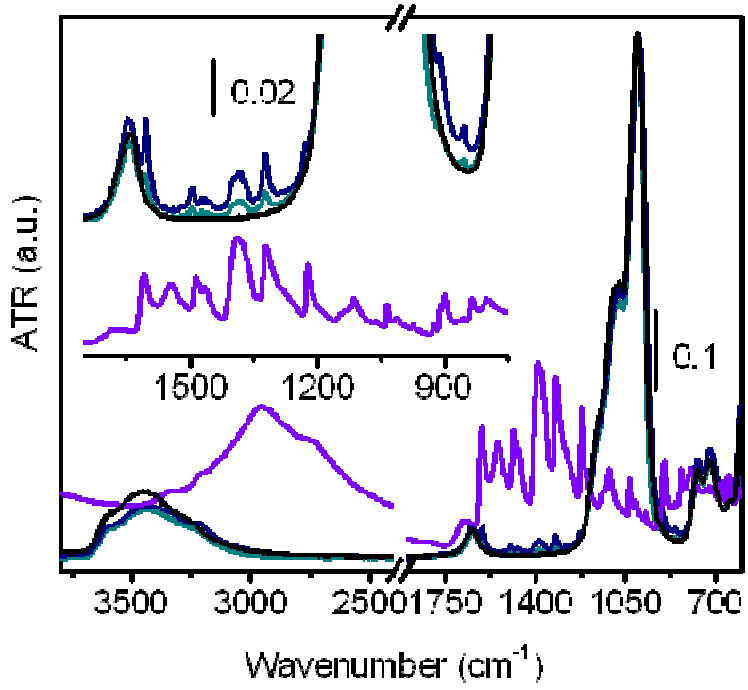

Figure 6.3.3.1 ATR-IR spectra, collected in air, in the 3800-600 cm^{-1} range for the pure dye thionine (violet), ZL/0.15Th (green), ZL/0.27Th (blue), and ZL (black). The inset shows the zoom of the 1750-1550 cm^{-1} region.

The ATR spectra of the two ZL/Th composites show a blue shift of all thionine peaks after the encapsulation into the ZL channels (Fig. 6.3.3.1).

In particular it is evident the shift of C-C stretching- at 1610 in the pure dye- to 1604 cm^{-1} in the ZL/Th composites. The same behavior was reported for the methylene blue dye (MB) on titanates, upon drying, as a consequence of the interaction of π- orbitals of the organic compound with the oxide surface [16]. This result could hence be interpreted with the thionine dye interaction with the zeolite framework, but further investigation on dehydrated ZL/Th system should be performed to confirm this hypothesis. Another evident feature is that the peaks intensity, increase with the thionine loading.

6.3.4. STRUCTURE REFINEMENT

The comparison among the XRPD patterns collected on the ZL and on the ZL/0.15Th and ZL/0.27Th composites, reported in Figure 6.3.4.2, evidences the differences in the intensity of the diffraction peaks at low 2Θ angle region due to the dye incorporation.

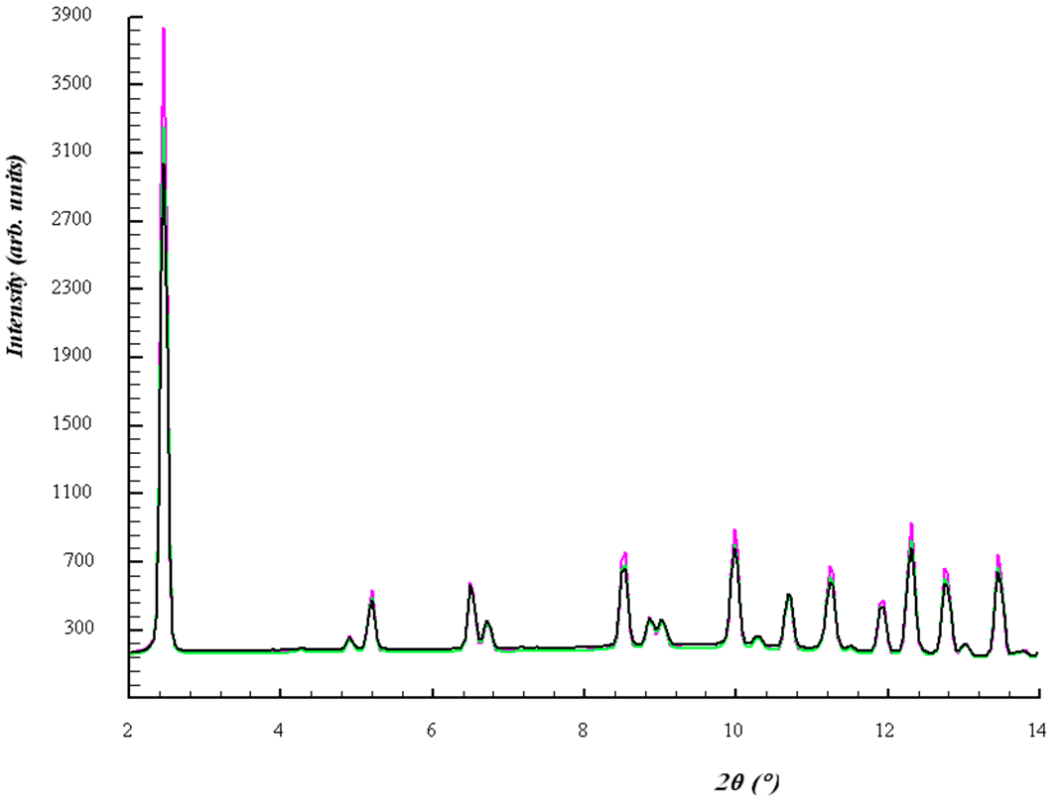

Figure 6.3.4.2. Comparison of the patterns of the ZL (fuxia line), the ZL/0.15Th (green line) and the ZL/0.27Th (black line) composites.

A further XRPD pattern (CuKα), collected in a short range of low 2theta for 20 hours (Fig. 6.3.4.3) did not reveal superstructure reflections as could have been expected by an ordered distribution of a molecule like Th whose length is twice the ZL *c* parameters.

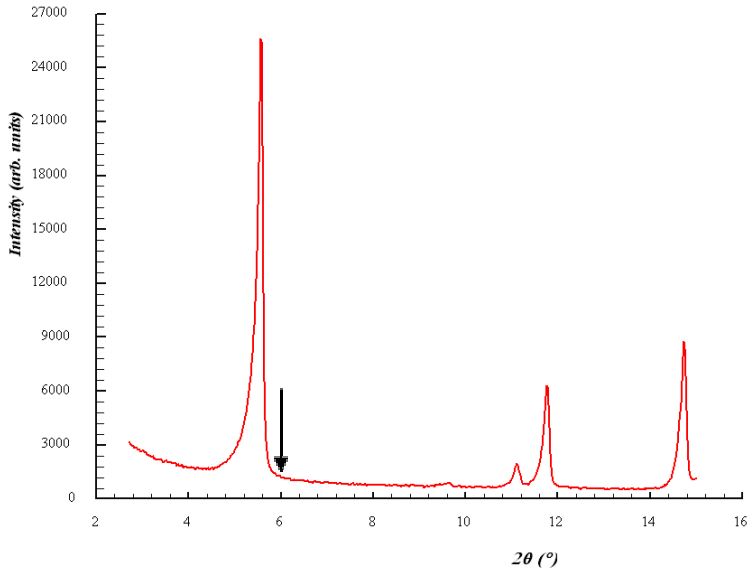

Figure 6.3.4.3. XRPD pattern collected with a conventional diffractometer of the ZL/0.27Th composite in the 2.5- 14 2Θ range. The arrow indicates the position of the superstructure reflection.

For both ZL/0.15Th and ZL/0.27Th materials the structural refinement was performed in the ZL P6/mmm space group. The unit cell of the composites show a slight increase of *a* and a decrease of *c* parameters because of the incorporation of the dye (Table 6.3.4.1, Appendix D). These changes can be explained by slight distortions in the 12MR ring (see Figure 6.4.3.4 for details). As can be seen, the ring shape becames slightly elliptical in the presence of thionine when compared with that found in ZL.

The most remarkable change appears related to the O1–O1 distance, which decreases as a consequence of the strain imposed by the water molecule W2.

In both the composites the Fourier maps showed disorder around the 6-fold axis. For this reason, the complete geometry of thionine molecules inside the zeolite channel was not fully understood. Only the thiazine ring (containing the sulfur and nitrogen atoms) was located. Six equivalent, partially occupied sites, of the heterocyclic ring were found oriented parallel to the 12MR channel axis. In Figures 6.3.4.5 and 6.3.4.6 only one of the six possible orientation of

the thiazine ring for sake of clarity and the organization of the water molecule in both the composites are represented

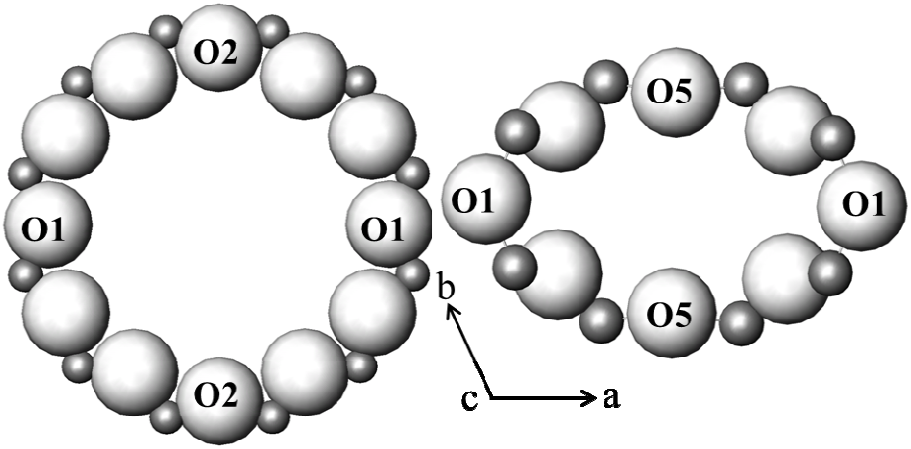

Sample	12MR		8MR //*c*	
	O1-O1	O2-O2	O1-O1	O5-O5
ZL	10.10	10.43	8.29	4.87
ZL/Th20	10.08	10.41	8.38	4.96
ZL/Th50	10.00	10.44	8.42	4.98

Figure 6.3.4.4. Dimensions of the 12MR and 8MR channels parallel to [001] of ZL and ZL/Th composites

The occupancy factors and the thermal displacement parameters of the thiazine ring atoms were constrained to be the same. Hence it is impossible estimate the amount of thionine molecule trapped in the zeolite porosities from the structural analysis.

Concerning the water content in the composites, only two partially occupied water positions (sites WI and W2) were found in the 12 MR channel. In particular 15.9 molecules/u.c. in ZL/0.15Th composite and 14.8 molecules/u.c in ZL/0.27Th one were found, in good agreement with the TGA results (Tables 6.3.2.1. and 6.3.4.3, Appendix D). This evidence that the extraframework distribution is highly influenced by the incorporated thionine if compared with the extraframework water sites of the as synthetized ZL.

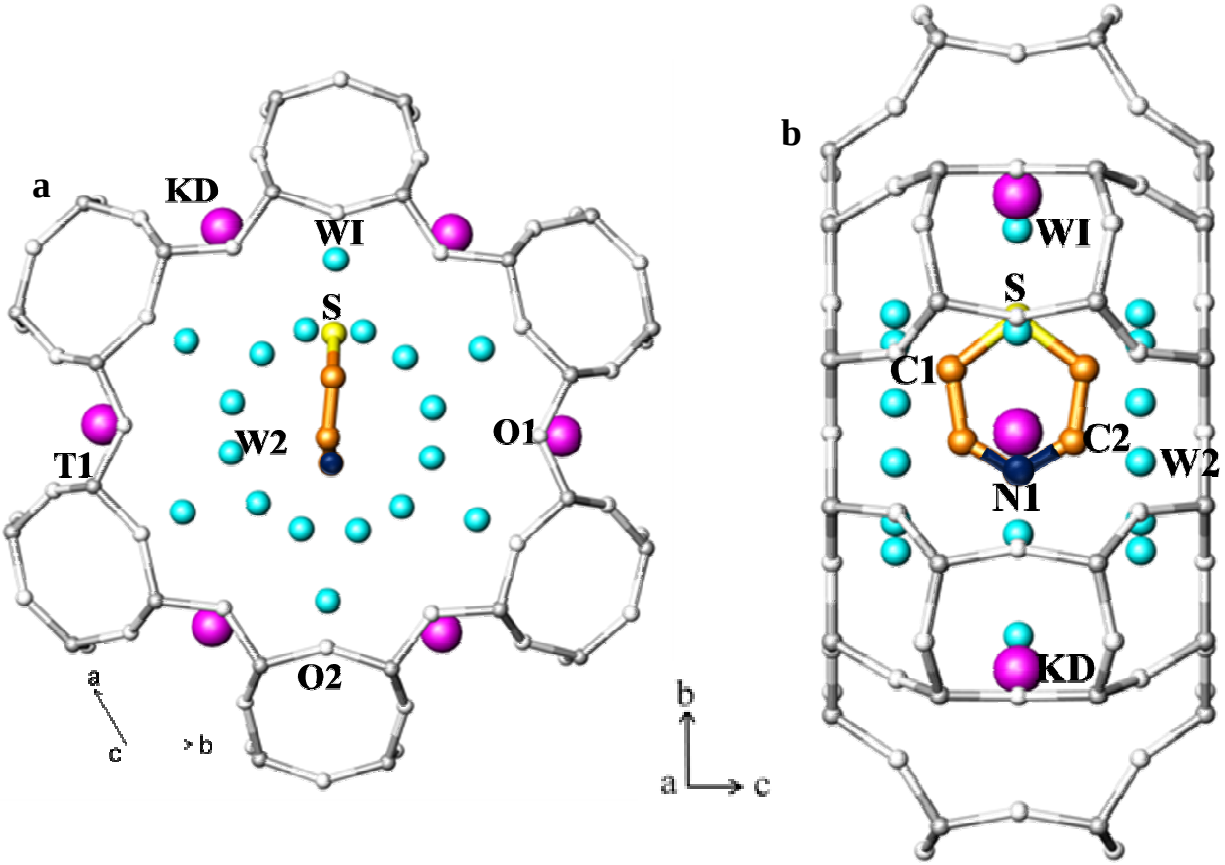

Figure 6.3.4.5. View of 12MR channel (a) and arrangement of Th and water molecules viewed along [001] (b) in ZL/0.15Th composite. Only one thiazine ring is represented for sake of clarity**.**

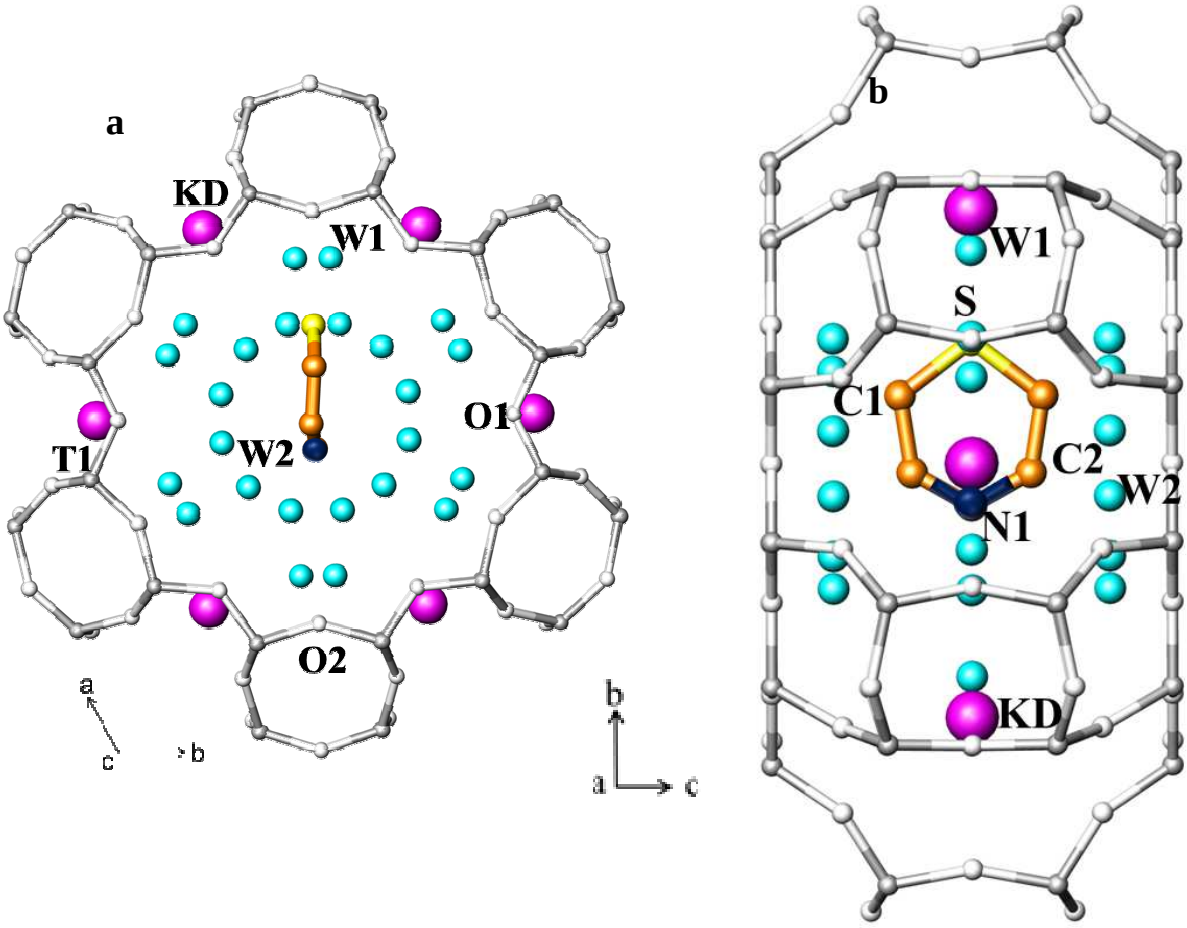

Figure 6.3.4.6. View of 12MR channel (a) and arrangement of Th and water molecules viewed along [001] (b) in ZL/0.27Th composite. Only one thiazine ring is represented for sake of clarity.

The Table 6.3.4.4 (Appendix D), reporting the extraframework bond distances, reveals the presence of short distances between the carbon, sulfur and nitrogen atoms and the water molecules site in W2. W2, in turn, is bonded to the O1 an O2 oxygen atoms belonging to the 12 MR, suggesting water-mediated thionine-ZL interactions [17].

6.3.5 OPTICAL PROPERTIES

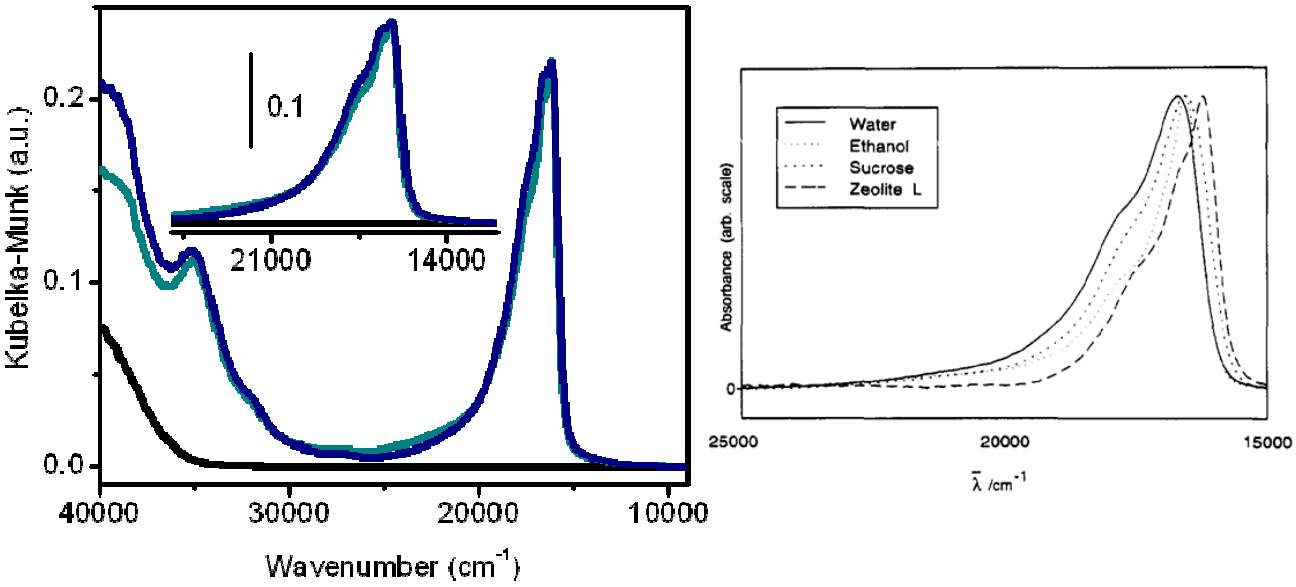

Figure 6.3.5.1 Left: UV-Vis absorption spectra for the ZL/0.14Th (green) and ZL/0.27Th (blue) composites and ZL (black). Right: absorption spectra of 10-5 M thionine solution in different solvents and encapsulated in ZL as reported in [15].

The absorption spectra of the ZL/Th composites shown in Figure 6.3.5.1 are in line with that reported in literature [15,18,19] and show that they have the same shape of the spectrum of the pure thionine dissolved in ethanol. Moreover, it is evident that the loading does not affect the peak intensity revealing, in both cases the presence of only monomeric thionine inside the ZL channels and that the formation on the ZL surface at the maximum loading (ZL/0.27Th) is negligible. In fact, as mentioned in the chapter 4.1.2. the thionine ,once trapped in the zeolite [20], is in a more constrictive surrounding with a consequent loss of conformational freedom inside the channel [10,19].

6.3.6. CONCLUSIONS

Even in the case of the ZL/Th composites a multidisciplinary approach was essential to verify the insertion of the Th in the channels of zeolite.

The thermogravimetric analysis showed that the two samples have different thionina contents and that the sample ZL/0.27Th presents the maximum Th loading for ZL, equal to 0.27 molecules, confirming the data of literature.

The ATR-IR spectroscopy revealed a blue shift of all the Th peaks once trapped in the zeolite, with respect to the pure dye. This effect could be interpreted as due to an interaction of Th with the zeolite framework. The structure refinement indicated high disorder around the 6-fold axis, within the 12MR channel, that led to the localization of the thiazine ring. The presence of short distances between the thiazine ring and a water molecules site bonded to the framework oxygen of the 12 MR suggested a water-mediated thionine-ZL interaction. As reported in literature, the absorption data collected on the two composites show the presence of only monomeric thionine caged the ZL channel excluding the formation of aggregates on the zeolite surface.

APPENDIX D

Table 6.3.4.1. Experimental and refinement parameters for zeolite L as-synthesized and ZL/0.15Th and ZL/0.27Th composites.

Samples	**ZL**	**ZL/0.15Th**	**ZL/0.27Th**
Space Group	P6/m m m	P6/m m m	P6/m m m
a (Å)	18.3795(4)	18.3807(4)	18.3833(8)
c (Å)	7.5281(2)	7.5285(2)	7.5277(4)
V ($Å^3$)	2202.4(1)	2202.8(1)	2203.1(1)
R_p (%)	2.8	3.4	3.2
R_{wp} (%)	3.8	4.8	4.6
R F2 (%)**	7.3	7.5	7.6
No. of variables	73	69	69
No. of observations	2211	2210	2210
No. of reflections	944	944	945

Table 6.3.4.2. Atomic coordinates, occupancy factors and thermal displacement parameters for the structures of as synthetized ZL, ZL/0.15Th and ZL/0.27Th composites.

Atom	x/a	y/b	z/c	Occ.	Uiso
			ZL		
T1	0.0939(1)	0.3566(2)	0.5	1	0.0136(5)
T2	0.1646(2)	0.4978(1)	0.2093(2)	1	0.0136(5)
O1	0	0.2694(6)	0.5	1	0.0159(9)
O2	0.1616(2)	0.3233(5)	0.5	1	0.0159(9)
O3	0.2671(2)	0.5342(4)	0.2534(8)	1	0.0159(9)
O4	0.1019(3)	0.4127(3)	0.3241(5)	1	0.0159(9)
O5	0.4245(2)	0.8490(4)	0.2645(9)	1	0.0159(9)
O6	0.1452(4)	0.4762(4)	0	1	0.0159(9)
KB	0.33333	0.66667	0.5	1	0.016(3)
KC	0.5	0	0.5	1	0.037(3)
KD	0.3006(5)	0	0	0.804(2)	0.057(3)
WF	0.117(2)	0	0	0.42(1)	0.149(9)
WH	0.119(1)	0	0.371(2)	0.43(1)	0.149(9)
WI	0.257(1)	0.128(5)	0	0.88(1)	0.149(9)
WJ	0.162(1)	0.0814(7)	0.292(3)	0.44(1)	0.149(9)
WK	0	0	0.185(1)	0.25(2)	0.149(9)
			ZL/0.15Th		
T1	0.0928(2)	0.3560(2)	0.5	1	0.011(6)
T2	0.1651(2)	0.4968(1)	0.2111(2)	1	0.011(6)
O1	0	0.27195(58)	0.5	1	0.013(3)
O2	0.1634(3)	0.3269(7)	0.5	1	0.013(3)
O3	0.2638(2)	0.5277(5)	0.254(1)	1	0.013(3)
O4	0.1010(3)	0.4121(3)	0.3244(6)	1	0.013(3)
O5	0.4221(1)	0.8442(3)	0.272(1)	1	0.013(3)
O6	0.1461(5)	0.4789(5)	0	1	0.013(3)
KB	0.33333	0.66667	0.5	1	0.017(3)
KC	0.5	0	0.5	0.92(9)	0.018(2)
KD	0.3033(8)	0	0	0.78(7)	0.064(4)
S	0.4789(5)	0.4789(5)	0	0.089(2)	0.12(1)
C1	0.08008(4)	0.04002(2)	0.17820(9)	0.089(2)	0.12(1)
C2	0.01093(3)	0.01093(3)	0.14781(8)	0.089(2)	0.12(1)
N1	0.05016(8)	0.02509(4)	0	0.089(2)	0.12(1)
W2	0.1123(30)	0.1498(21)	0.6721(33)	0.47(1)	0.25(2)
WI	0.128(1)	0.872(1)	0	0.74(2)	0.08(3)
			ZL/0.27Th		
T1	0.0924(3)	0.3556(2)	0.5	1	0.010(1)
T2	0.1647(2)	0.4964(1)	0.2116(3)	1	0.010(1)
O1	0	0.2709(6)	0.5	1	0.013(2)
O2	0.1639(3)	0.3279(7)	0.5	1	0.013(2)
O3	0.2634(2)	0.5269(5)	0.250(1)	1	0.013(2)
O4	0.1009(3)	0.4109(3)	0.3228(6)	1	0.013(2)
O5	0.4217(1)	0.8434(3)	0.271(1)	1	0.013(2)
O6	0.1469(6)	0.4791(5)	0	1	0.013(2)
KB	0.33333	0.66667	0.5	1	0.012(2)
KC	0.5	0	0.5	0.92(2)	0.016(2)
KD	0.3004(7)	0	0	0.77(1)	0.053(4)
S	0.14500(8)	0.07249(4)	0	0.095(3)	0.12(3)
C1	0.08031(4)	0.04014(2)	0.17800(9)	0.095(3)	0.12(3)
C2	0.01072(2)	0.01072(2)	0.14812(7)	0.095(3)	0.12(3)
N1	0.04972(8)	0.02487(4)	0	0.095(3)	0.12(3)
W1	0.150(4)	0.8982(32)	0	0.45(1)	0.14(2)
W2	0.109(1)	0.147(1)	0.654(2)	0.38(4)	0.23(3)

Table 6.3.4.3. Framework bond distances for ZL, ZL/0.15Th and ZL/0.27Th composites and extraframework distances < 3.2 Å for ZL sample.

	ZL	ZL/0.15Th	ZL/0.27Th
T1-O1	1.635(4)	1.631(3)	1.632(7)
O2	1.632(4)	1.632(3)	1.630(7)
O4 [X2]	1.635(3)	1.637(2)	1.637(7)
average	**1.634**	**1.634**	**1.634**
			1.635(7)
T2-O3	1.643(4)	1.639(3)	
O4	1.642(4)	1.644(3)	1.644(6)
O5	1.624(4)	1.647(4)	1.649(7)
O6	1.624(3)	1.625(2)	1.625(1)
average	**1.633**	**1.639**	**1.638**

KB-O3 [x6]	2.884(9)
KC-O5 [x4]	2.985(8)
KD-O4 [x4]	3.146(6)
O6 [x2]	3.033(5)
WI [x2]	2.848(6)
WF-WF [x2]	2.13(3)
WH [x2]	2.81(2)
WI [x2]	2.47(2)
WJ [x4]	2.56(2)
WK [x2]	2.60(3)
WH-O1	2.98(1)
WF	2.81(2)
WH[x2]	2.20(2)
WH[x2]	2.91(3)
WH	1.91(4)
WJ[x2]	1.425(8)
WJ[x2]	2.83(2)
WK	2.60(2)
WI-WF[x2]	2.47(2)
WJ[x2]	2.675(9)
WJ-O2	3.06(1)
WF[x2]	2.56(2)
WH[x2]	1.425(8)
WH[x2]	2.83(2)
WI	2.675(9)
WJ [x2]	2.59(2)
WJ	3.12(5)
WK	2.69(2)
WK-WF [x6]	2.60(3)
WH [x6]	2.60(2)
WJ [x6]	2.69(2)
WK	2.85(2)

Table 6.3.4.4. Extraframework bond distances < 3.2 Å for ZL/0.15Th and ZL/0.27Th composites.

	ZL/0.15Th	ZL/0.27Th
KB-O3 [x6]	2.882(8)	2.91(1)
KC-O5 [x4]	3.016(8)	3.02(1)
KD-O4 [x4]	3.141(6)	3.12(1)
O6 [x2]	3.042(8)	3.05(1)
W1[x2]		2.45(1)
W3	2.88(2)	
S- W1[x2]	---	1.75(3)
W2[x4]	2.97(2)	2.67(2)
W2[x4]	3.05(3)	3.16(2)
WI	1.77(3)	---
C1-W1[x2]	----	3.06(2)
WI	3.10(3)	----
W2[x2]	2.74(3)	2.75(3)
W2[x2]	2.12(3)	2.17(3)
W2[x2]	1.72(3)	1.77(4)
C2-W2[x2]	3.00 (2)	3.02(2)
W2[x2]	2.88(2)	2.92(2)
W2[x2]	2.71(2)	2.73(2)
W2 [x2]	2.78 (2)	2.69(2)
W2 [x2]	2.95(2)	2.81(2)
W2 [x2]	2.65(2)	2.97(2)
N1- W2[x4]	3.01(3)	3.09(3)
W2[x4]	3.16(5)	3.13(2)
W1-W1	----	0.88(4)
W2[x2]	----	3.08(3)
WI-KD	2.88(2)	----
W2[x4]	3.07(2)	----
W2-O1	2.95(1)	2.93(2)
O2	3.18(2)	3.16(2)
W1	3.06(4)	3.08(4)
W2[x2]	2.48(2)	2.43(3)
W2	1.37(2)	1.33(4)
W2	1.19(2)	1.22(4)
W2	2.59(2)	2.33(2)
W2	2.85(3)	2.63(2)
W2	2.93(3)	2.67(2)

References

[1] Devaux A., Minkowski C., and Calzaferri G. (2004) *Chem. Eur. J.*,10, 2391-2408

[2] Gigli L., Arletti R., Quartieri S., Di Renzo F., Vezzalini G. (2013) *Microporous and Mesoporous Materials*, 177, 8–16

[3] Pazé C., Bordiga S., Lamberti C., Salvalaggio M., and Zecchina A., Bellussi G., (1997) *J. Phys. Chem. B,* 101 (24), 4740–4751

[4] Zecchina A., Scarano D., Bordiga S., Spoto G., Lamberti C. (2001) *Adv. Catal*., 46, 265-397

[5] Fois E., Tabacchi G., Calzaferri G. ,J. (2010) *Phys. Chem. C*, 114, 10572 – 10579

[6] Zhou X., Wesolowski T. A., Tabacchi G., Fois E., Calzaferri G., Devaux A. (2013) *Phys. Chem. Chem. Phys*., 15, 159−167

[7] Luss H. R. , Smith D.L. (1972) *Acta Cryst*., B28, 884-889

[8] Fois,E., Tabacchi G., Calzaferri G. (2012) *J. Phys. Chem. C*, 116,16748-16799

[9] Fois E., Tabacchi G., Devaux A., Belser P., Brühwiler D., Calzaferri G. (2013) *Langmuir*, 29, 9188– 9198

[10] Devaux A., Calzaferri G., Miletto I, Cao P., Belser P., Brühwiler D., Khorev O., Häner R., Kunzmann A. (2013) *J. Phys. Chem. C,* 117, 23034-23047

[11] Brühwiler D., Calzaferri G., Torres T., Ramm J. H., Gartmann N., Dieu L.-Q., Lopez-Duarte I., Martinez-Diaz M. V. (2009) *Journal of Materials Chemistry*, 19, 8040 – 8067

[12] Hennessy B., Megelski S., Marcolli C., Shklover V., Ba¨rlocher C., Calzaferri G., (1999) *J. Phys. Chem.* B, 103, 3340-3351

[13] Van Koningsveld H., Tuinstra F., Van Bekkum H., Jansen J.C. (1989) *Acta Cryst. B*, 45, 423-431

[14] Simoncic P., Armbruster T. (2005) *Microporous and Mesoporous Materials*, 81, 87–95

[15] Calzaferri, G., Gfeller N. (1992) *J. Phys. Chem.*, 96, 3428-3435

[16] Horvath E., Rebernik Ribi P., Hashemi F., Forro L., Magrez A. (2012) *J. Mater. Chem.*, 22, 8778–8784

[17] Steiner,T. (1995) *Acta Crystallogr., Sect. D,* 51, 93-97

[18] Mackay R.A. (2005) *Physicochem.Eng.Aspect,* 254, 115-123

[19] Ding J.Y. Shih P.Y., Yin C.K. (2004) *Materials Chemistry and Physics,* 84, 263–272

[20] Ramamurthy, V., Sanderson, D.R., Eaton, D.F. (1993) *J. Am. Chem. Soc*., 115, 10438-10439

CONCLUSIONS

The work here presented corresponds to the first step towards the creation of very innovative devices and nano devices based on hybrid materials and host/guest systems. In particular, the aim of this thesis was to unravel and understand, at molecular level, the guest-guest and host-guest interactions that govern their optical properties.

We adopted an systematic integrated experimental-theoretical characterization strategy, based on the use of in-situ and ex-situ X-ray powder diffraction, with both conventional and synchrotron source and Rietveld refinement, vibrational spectroscopies (ATR-IR, FT-IR), UV-Vis and luminescence experiments, along with molecular dynamics simulations.

The main results can be summarized as follows:

ZL/FL composites: The TG-MSEGA analysis showed that the fluorenone release occurs at higher temperature with respect to pure FL, indicating that FL is not simply physisorbed on the zeolite surface, but it is encapsulated into the zeolite channels. The weight losses of the encapsulated FL correspond to 0.44, 0.9, 1.43 and 1.5 FL molecules per unit cell in ZL/0.5FL, ZL/1.0FL, ZL/1.5FL and ZL/2.25FL composites, respectively so indicating that the maximum possible loading is 1.5 molecules.

The ATR-IR and FTIR results reveal and the presence of red shift of the IR signals of the C=O band due to its direct interaction with the potassium atoms in the ZL channels. Another important aspect, highlighted by the FTIR transmission spectroscopy, is the high stability of these composites in presence of water molecules, which do not affect the organization of the fluorenone molecule. The distribution of fluorenone molecules within the ZL channel was obtained combining the structure refinement and the Molecular Dynamic simulations results. The results of the Rietveld refinements of all the studied samples showed a general disordered distribution of water and FL molecules on partially occupied, highly symmetric positions. The K-O=C motif showed in the ATR-IR spectroscopy has been evidences by the diffraction data , through the short bond distances between the two atomic species.

The DFT-based modeling besides supporting and strengthening experimental evidences, proved once again its capability in providing information otherwise extremely difficult to access from the experiments. In fact, the high symmetry of the zeolite affects the

experimental model obtaining an array of the FL molecules more symmetrical respect to that found in the calculated models.

ZL/tB-DXP composite: The successful encapsulation of the tB-DXP was demonstrated by all the techniques employed.

The TGA-MSGA reveals that the maximum loading of tB-DXP is equal to 0.23 molecules per u.c.

The ATR-IR and FT-IR measurements, evidence that all the dye vibrational signals (1800-1200 cm^{-1}) are strongly perturbed during the water removal suggesting some kind of interaction between the dye and the water molecules inside the ZL channel. The diffraction localized a total amount of 0.25 dye molecules per unit cell oriented parallel to the 12MR channel axis.

Moreover the refinement showed that the dye interacts with the zeolitic framework through C--O bond and that the carbonyl group of the dye is not in direct interaction with the potassium, as seen for the fluorenone but their interaction is mediated by water.

Another important aspect highlighted by the Uv-Vis and emission measurement is that the tB-DXP is an interesting and convenient molecule due to the tendency to not show signs of the formation of J aggregates even at high loading because the bulky *t*- butyl end- substituents groups always keep the molecules at sufficient distances from each other inside the ZL channels.

ZL/Th composites: The thermogravimetric analysis performed on the two composites showed that the maximum possible Th loading for the zeolite L, equal to 0.27 molecules, confirming the data of literature.

The ATR-IR spectroscopy revealed through a blue shift of all the Th peaks in the composites with respect to the pure dye, which could suggest an interaction of Th with the zeolite framework.

The structure refinement indicated high molecular disorder around the 6-fold axis within the 12MR channel thus allowing the localization of only the thiazine ring. The presence of short distances between the thiazine ring and a water molecules site, bonded to the framework oxygen of the 12 MR, suggests a water- mediated thionine-ZL interactions

The absorption spectra collected on both the composites, confirm the presence of only monomeric thionine caged in the ZL channel excluding the formation of aggregates on the zeolite surface.

In conclusion, this work dealt, for the first time, with the organization of very high concentrated dye molecules inside ZL channels. In a broader perspective, the fundamental-level understanding of the interplay of host-guest/guest-guest interactions, which underlies supramolecular organization at high packing conditions, holds the promise to disclose alternative routes for the design of dye-ZL composites as building blocks for innovative optical devices.

APPENDIX I. FÖRSTER RESONANT ENERGY TRANSFER (FRET)

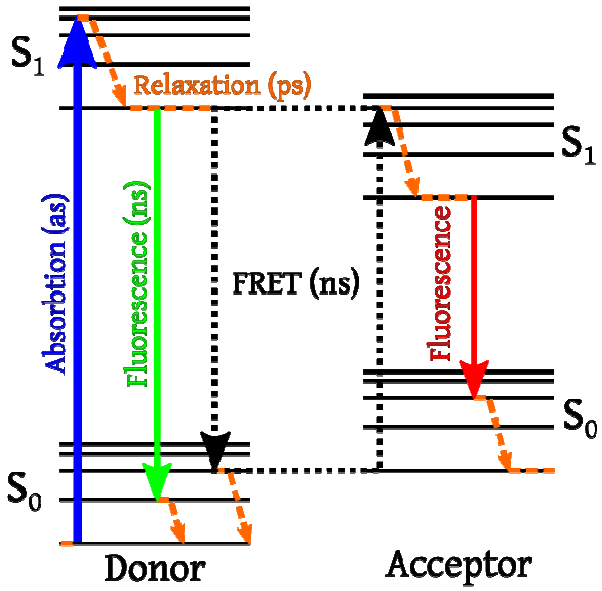

Figure AI.1 Energy diagram of the FRET process

The theory of resonance energy transfer was originally developed by Theodor Förster and, in honor of his contribution, has recently been named after him [1].

The fundamental mechanism of FRET (Figure AI.1) involves a donor fluorophore in an excited electronic state (D*), which may transfer its excitation energy to a nearby acceptor fluorophore (A) in a non-radiative way, through long-range dipole-dipole interactions [2-3]. The Förster mechanism involves no orbital overlap between the donor and acceptor molecules, and no electron transfer occurs;

$$(D^* \ldots A_i) \xrightarrow{K_{EnT}^{(i)}} (D \ldots A_i^*).$$

Resonance energy transfer can be considered analogous to the behavior of coupled oscillators.

In such a system, the “optical electrons” associated with individual component molecules (or chromophoric units) preserve essentially their individual characteristic.

The donor D and the acceptor A can be the same kind of molecules or different.

Förster observed that the rate constant K_{EnT} for the transfer from one electronic configuration to the other can be expressed as a product of three terms:

$$K_{EnT} \propto G \cdot DA \cdot S$$

The geometrical expression G describes the dependence of the rate constant on the distance and angle between the electronic transition dipole moments (ETDMs) of the donor and the acceptor. The term DA specifies the chromophores involved, by taking into account the resonance condition as well as the photophysical properties of the donor; while the factor S takes into account the environment of the pair.

Some prerequisites have to be satisfied to let the FRET occurs:

1) dipole orientation,
2) sufficient fluorescence lifetime,
3) the donor emission spectrum has to overlap the excitation spectrum of the acceptor (J_{DA}) (Figure AI.2),
4) the quantum yield of the donor and the extinction coefficient of the acceptor
5) the distances between the donor and the acceptor (Figure AI.3)

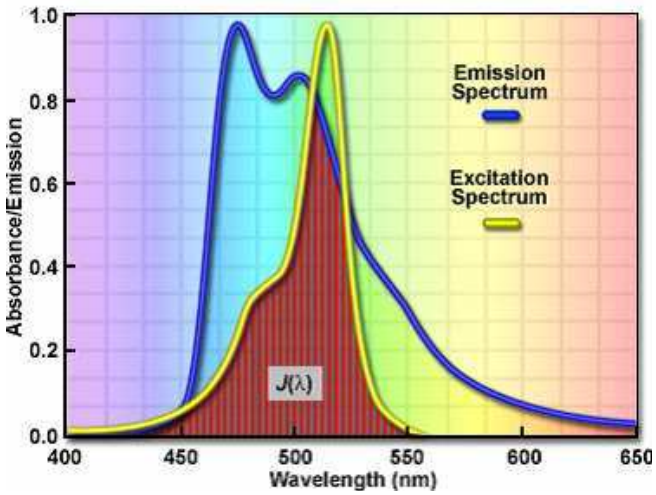

Figure AI.2. An example of overlap between the donor's emission and acceptor's excitation spectra

Concerning the latter aspect, the Förster theory shows that FRET efficiency (E_{FRET}) (equation 1) varies as the inverse sixth power of the distance between the two molecules (r_{DA}):

$$E_{FRET} = \frac{1}{1 + \left(\frac{r_{DA}}{R_0}\right)^6} \quad [1]$$

R_0 is the characteristic distance where the FRET efficiency is 50 percent, which can be calculated for any pair of fluorescent molecules (this variable is also termed the Förster radius). The FRET efficiency of a theoretical fluorophore pair therefore depends on the distance between the donor and the acceptor as shown in Figure AI.3.

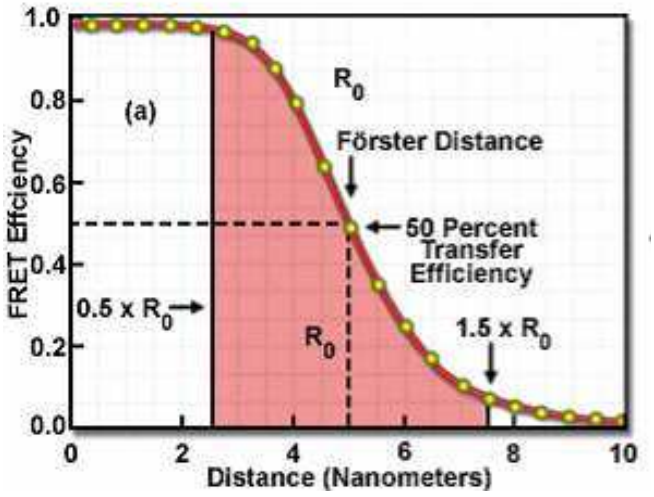

Figure AI.3. FRET efficiency *vs* Distance for an example where R_0 is considered to be 5 nm

Because of the inverse sixth power dependence of the distance between the two molecules, the curve has a very sharp decline. For distances less than R_0, the FRET efficiency is close to maximal, whereas for distances greater than R_0, the efficiency rapidly approaches zero. R_0 can be calculated for any pair of fluorescent molecules using the equation 2 with the well-established input parameters:

$$R_0 = \sqrt[6]{\mathrm{J_{DA}}\ \frac{9\ln(10)\,\phi_D\,\kappa^2}{128\,\pi^5 n^4\,N_A}} \qquad [2]$$

where J_{DA} is the overlap integral between the emission spectrum of the donor and the excitation spectrum of the acceptor, Φ_D is the fluorescence quantum yield of the donor and the parameter k^2 describes the relative orientation of the transition dipole moments of the donor and the acceptor (Fig. AI.4)

$$\kappa^2 = (\cos\theta_T - 3\cos\theta_D \cos\theta_A)^2$$

$$\kappa^2 = (sin\theta_D \, sin\theta_A \, cos\phi - 2 \, cos\theta_D \, cos\theta_A)^2$$

.

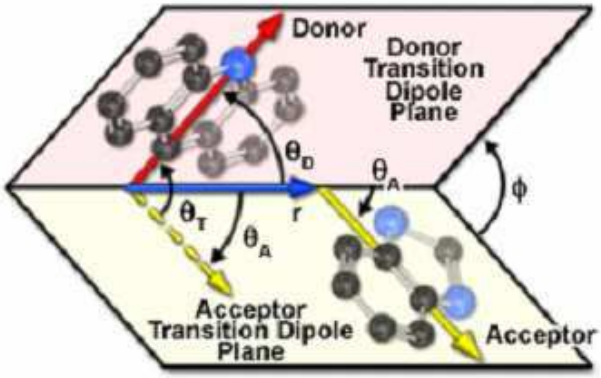

Figure AI.4. Relative orientation of the donor and the acceptor's dipole moments and calculation of the orientation factor.

The orientation angle variable k^2 simply indicates that the FRET coupling depends on the angle between the two fluorophores, in the same manner as the position of a radio antenna can affect its reception. If the donor and acceptor are aligned parallel to each other, the FRET efficiency will be higher than if they are oriented perpendicular. This degree of alignment defines k^2. Although k^2 can vary between zero and 4, it is usually assumed to be 2/3, which is the average value integrated over all possible angles.

References

[1] Calzaferri, G., Devaux, A., Ramamurthy, V., Inoue, Y.,. John Wiley & Sons (Editors): New York, 2011; Chapter 9, 285−387.

[2] Förster T. (1948), *Ann. Physik*, 437, 55-75

[3] Andrews, D. L., Bradshaw, D. S. (2004) *Eur. J. Phys*, 25, 845-858.

APPENDIX II. X-RAY POWDER DIFFRACTION USING SYNCHROTRON RADIATION

The diffraction techniques have been and are still a point of reference for the structural characterization of zeolites. Recent developments achieved in the application of X-ray powder diffraction (XRPD) - using areal detectors or synchrotron radiation- and the development of efficient data analysis methods, such as Rietveld refinements have had a strong impact in the structural studies. One of the problems of the diffraction techniques is that, for many crystalline solids it is difficult to grow a single crystal of sufficient size and quality to allow analysis by this method,. However high-quality polycrystalline samples are often easier to obtain, leading to the choice of powder diffraction to determine crystal structures.

For a typical X-ray powder diffraction experiment, the scattering intensity I_h is obtained by integrating the diffraction profile of every reflection. Integrated intensities give important information about the crystal structure because they are proportional to structure factor $|F_{(h)}|^2$, which is directly related to the arrangement of atoms within the unit cell and proportional to the amount of diffracting material in the powder sample.

The measurements made with synchrotron light are probably the best method to study complex structures such as dye-zeolite systems. The synchrotron radiation is the electromagnetic field emitted when relativistic accelerated charged particles (electrons or positrons), which are moving close to the speed of light, are forced to move along a circular path with the application of a static magnetic field perpendicular to the horizontal orbital plane (Fig. AII.1). The radiation is emitted in the direction of motion in a narrow cone tangential to the orbit of the electrons. The synchrotron radiation is therefore a very intense electromagnetic radiation with a broad emission band that can go from infrared to "hard" X-ray .

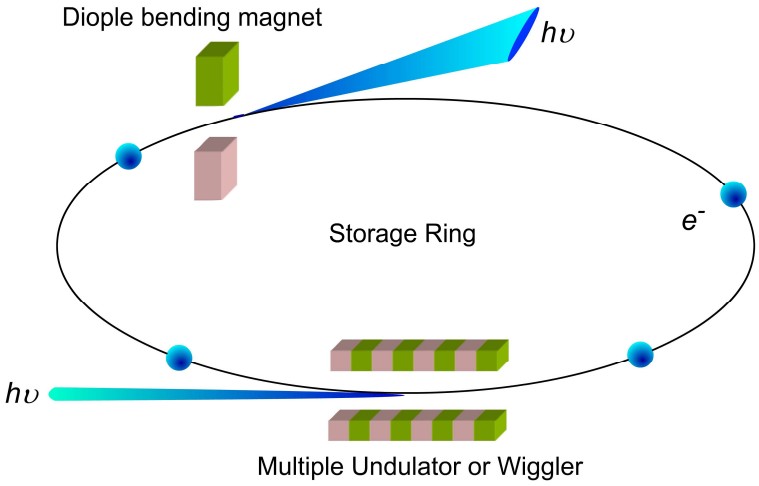

Figure AII.1. Radiation emission pattern of relativistic electron ($v/c \approx 1$) in circular motion.

Synchrotron light produced in this manner possesses a number of unique properties:

I. high brightness
II. small radiation axial divergence
III. variability in a continuous mode over a wide range of energy
IV. polarization of the outgoing beam.

The high intensity and the low divergence of the outgoing beam allow to obtain high resolution in powder diffraction experiments, increasing the amount of information derivable from a powders diffraction profile. The advantages offered by the use of synchrotron radiation are: a) the ability to monitor the occurrence of phase transitions even if there are small variations in dimensions and shape of the unit cell, b) the possibility to perform time resolved experiments in milliseconds, c) the diffracted intensities can be detected in a relatively short time with good signal/noise ratio.

The use of this technique to study systems such as dye-zeolite systems, object of this thesis, is of fundamental importance as the dye molecules consist often of light atoms such as carbon, nitrogen and oxygen; for this reason high resolution data can facilitate their localization inside the zeolite.

The combined use of high-intensity X-rays from synchrotron radiation and areal detector as the imaging-plate (IP) has made feasible the collection of data in very short time.

The IP detectors allow to simultaneously record the rays diffracted by a whole lattice plane, eliminating the problem of dead time counting of the gas detectors. Furthermore, the use of IP reduces the effect of peak broadening caused by the high intensity and the electronic noise.

The disadvantages are: the inability to directly observe the diffraction profile during the collection, the dead time for scanning and cleaning of the IP, the lower resolution respect to the experiments performed with single detectors combined with analyzers crystals or collimators.

For this thesis in particular, part of the data were collected using a ultimate large-area silicon pixel detector, named PILATUS3 M-Series hybrid pixel detector (Figure AII.2). It has many advantageous features such us:

- Direct detection of X-rays in single-photon-counting mode
- No read out noise
- No dark current
- Excellent point-spread function,

All these characteristics allow to improve the signal-to-noise ratio, reduce the overlap with scattering or other background intrinsic to the experiment. Moreover even after a long acquisition time, most pixels still have zero counts since no dark current accumulates and no noise is added during readout.

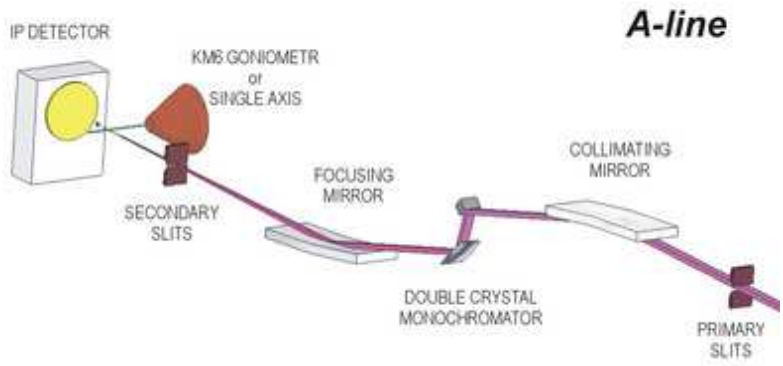

Figure AII.2 the instrumental set-up installed in the experimental hutch of the SNBL1 (BM01a) beamline at the ESRF laboratories.

AII-I RIETVELD METHOD

Through the Rietveld method is possible to perform the analysis of the measured profile trying to model and optimize simultaneously both the information relating to the sample (type and relative abundance of crystalline phases, structural models of all the phases, microstructural and textural parameters) and those related to the instrument used (wavelength, optical components, background instrumental, etc ...) [1-4]. This method is generally based on a nonlinear least squares minimization. It was introduced in the second half of the '60s by H. M. Rietveld and entered in the current terminology such as Rietveld method.

Specifically, the information that can be extracted from a profile are (Figure AII-I.1):

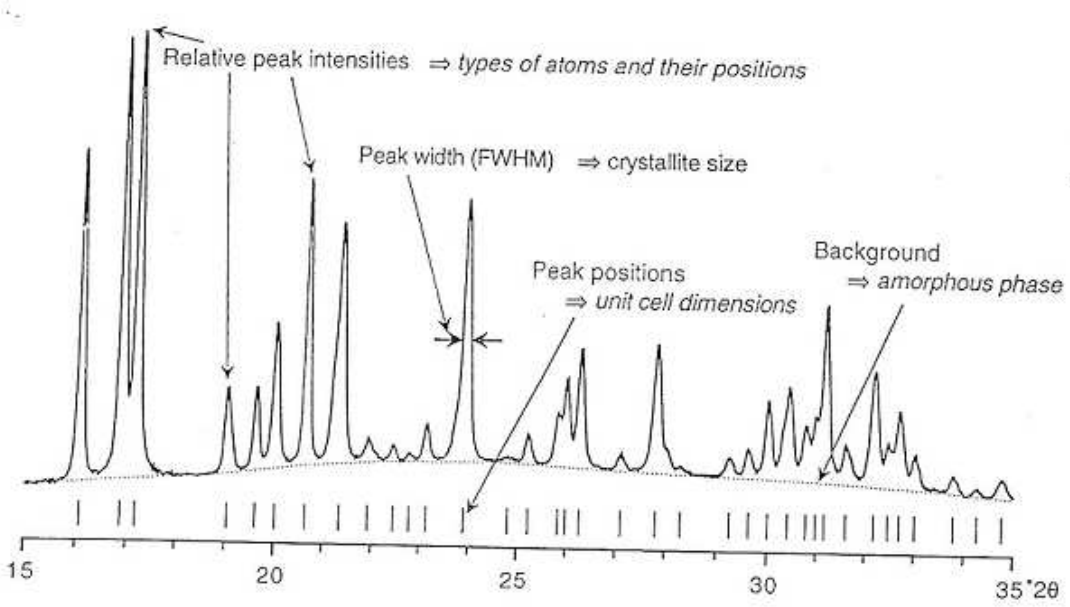

Figure AII-I.1. Main characteristics of a diffraction profile and information that can be derived from it [5].

1. The positions of the peaks in the reciprocal space; these depend only on the geometry of the unit cell, and then information on the cell parameters and space group are obtained.

This is because the value of 2θ Bragg is related to the interplanar distance d of the corresponding reflection from the Bragg equation $\lambda = 2d_{hkl}\text{sen}\theta_{hkl}$, where λ is the wavelength of the incident radiation and hkl are the Miller indices of the reflection.

2 . The relative intensities of the peaks. These are determined by the type and position of the atoms within the unit cell, thermal displacement and occupancy factors. Indeed I_{hkl}, the

intensity of each reflection, is proportional to the square of the structure factor F_{hkl} expressed by the summation extended to all the n atoms of the unit cell:

$$F_{hkl} = \Sigma_i \, X_i f_i \, e^{[\,2\pi i\,(\,HxI + kyi + LZI\,)\,]} \cdot e^{-Mi},$$

where:

fi = scattering factor, which identifies the type of atom ,

xi, yi and zi = atomic coordinates of each atom ,

Mi = parameter related to the thermal displacement factor,

Xi = site occupancy factor.

The intensities are also proportional to the amount of the diffracting material in the sample , allowing analysis not only qualitative but also quantitative of mixtures.

In fact, the diffractogram of a polyphasic mixture can be viewed as the superposition of the diffraction patterns of the individual phases that compose the mixture, collected in the same experimental conditions. The intensity of each phase is weighted on the modal fraction of each one.

3. The intensity distribution respect to the theoretical position of Bragg (profile shape of the peak). In particular, the peak width (full width half maximum- FWHM) depends from both instrumental effects and the intrinsic characteristics of the sample (size of the crystallites and lattice strain).

The extraction of these information allows to: i) identify and quantify the crystalline phases; ii) extract or refine the crystallographic structural model of the phases, iii) to determine microstructural and textural features of the crystalline phases.

This type of analysis, defined in general a full profile analysis, allows to simulate the observed profile describing and parameterizing all the experimental aspects and the sample features. The model parameters are then optimized by minimizing the differences between observed and calculated profile.

The refining variables are the following:

1) scale factor (for each phase and for each instrumental profile)

2) instrumental parameters

- Wavelength (λ);
- The coefficient of polarization (P)
- Angular calibration coefficient (zero shift)

- Coefficient function of the bottom instrumental
- Coefficient depending on the profile of the peaks
- Truncation factor (cut-off)

3) lattice parameters

4) structural parameters :

- Atomic coordinates (x , y, z) ,
- site occupancy factor (fractional occupancies)
- Atomic displacement parameters (U, B, and ß)
- Factor of anomalous diffusion

5) correction factors :

- Primary extinction
- Absorption or surface microabsorption
- Preferential orientation / texture
- Movement of the sample

In the Rietveld refinement all the measured points of the experimental profile are used as observed parameters.

The function actually minimized during the refinement is:

$$\mathbf{S_y = \sum^{N}_{i=1} [w_i(Y_{oi} - Y_{ci})^2]}$$

where:

S_y = residual function

Y_{oi} = observed intensity for the i-th step

Y_{ci} = calculated intensity for the i-th step

w_i = weight of each individual observation according to Poisson statistics.

The sum is extended to all the points of the diffraction pattern.

The intensity Y_{ci} diffracted at each angular step is calculated taking into account the contributions of the peak reflections overlap and the contribution of the background. The function Y_{ci} contains many variables and is very complex.

Each parameter that contributes to Y_{ci} is dependent by 2θ. In the case in which two parameters exhibit a similar dependence by 2θ can be useful to impose soft constraints, that are limits on the values that they can assume (e.g. bond distances).

References

[1] Rietveld,H.M. (1967). *Acta Crystallogr*., 22,151-2.;

[2] Rietveld,H.M. (1969). *J. Appl. Crystallogr*., 2,65-71;

[3] Young, R.A. (1993), *The Rietveld Method*, Oxford: University Press;

[4] Bish D.L., Post J.E., (1989) *American Mineralogist*, 78, 932-940;

[5] McCusker L.B., Baerlocher Ch., Grosse-Kunstleve R., Brenner S. and Wessels T. (2001) *Chimia*, 55, 497-504.

APPENDIX III. THERMAL ANALYSIS

According to the ICTA, International Confederation for Thermal Analysis, (ASTM 473-85), the definition of thermal analysis is "Group of techniques based on the measurement of a physical property of a substance in function of the temperature (or time) during a controlled temperature program (heating, cooling, isotherm)". The temperature program can have heating or cooling steps, or a constant temperature (isotherm), or a combination of those. It is very important define the temperature gradient b (b = dT / dt, where T = temperature in °C and t = time in min), i.e., as the temperature varies in function of the time. The results of the measurements produce the so-called "thermal analysis curve", and the features of this curve (such as peaks, discontinuities, slope changes) are related to the thermal events which occur in the sample.

The principal applications for these techniques are: i) the detection of chemical-physical transformations in the material during thermal treatment, ii) the evaluation of decomposition processes, iii) the determination of enthalpy and specific heat values and the study of reaction kinetics and mechanisms.

During a specific reaction, the heat exchanged between the system and the ambient is the variation of system enthalpy (CH). By convention, when CH<0, the heat moves from the system to the ambient and the reaction can be defined "exothermic", on the contrary when CH>0 the reaction can be defined "endothermic.

The most important exo/endothermic reactions are shown in Table AIII.1.

Table AIII.1: exo-endothermic reactions.

Endothermic reactions	**Exothermic reactions**
Melting	Adsorption
Dehydration	Crystallization
Polymorphic reactions	Oxidation
Sublimation	
Evaporation	
Structural modifications	

The methods widely used for initial characterization of the thermal behavior of zeolites are the thermogravimetric analysis (TGA, DTG) and differential thermal analysis (DTA). They are very useful as provide quickly a first information regarding the transformations of the

minerals in temperature (loss of H_2O, amount of volatile components, reactions of dehydroxylation, amorphization and recrystallization).

The thermogravimetric analysis (TGA) measures the sample weight change (Δm) during the heating process. Through the TGA curve it is possible to determine the quantity of the chemical species (water, templating, organic molecules of varied nature) lost during the heating but also their chemical nature because different chemical species are released the structure at different temperature. The DTG is the first derivative (dm/dT) of the previous measure that is automatically calculated during the measurement. Each reaction, that cause a weight loss, is shown in the TGA as a flex. Every slope change corresponds to a maximum in the DTG. The temperature at which the maximum in the DTG curve occurs is associated to the maximum speed of the loss reaction (Fig AIII.2).

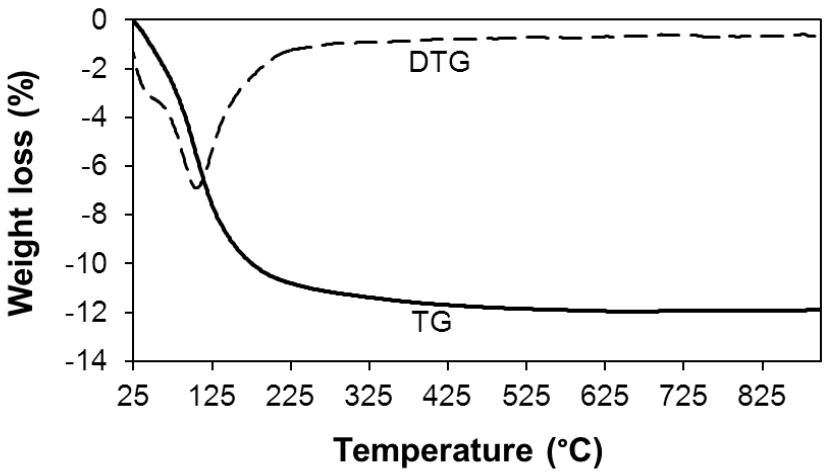

Figure AIII.2. TG and DTG curves of zeolite L.

The differential thermal analysis (DTA) consists of measuring the temperature difference between the sample and an inert reference (usually alumina) during heating. The inert reference is a material that during the thermal treatment increases its temperature (T_i) in function of the thermal gradient set, but does not undergo to any kind of transformations. The temperature of the sample material (T_s) is the same of the inert ($T = T_s - T_i = 0$) until a reaction occurs. In particular, if the temperature difference ($\Delta T<0$) an endothermic reaction is registered by the sample. When an exothermic reaction occurs, on the contrary, the difference of temperature between the inert material and the sample is positive ($\Delta T>0$).

A DTA graph, that is ΔT as a function of T, can show by endothermic and exothermic peaks in correspondence of the reaction temperatures (Fig. AIII.3).

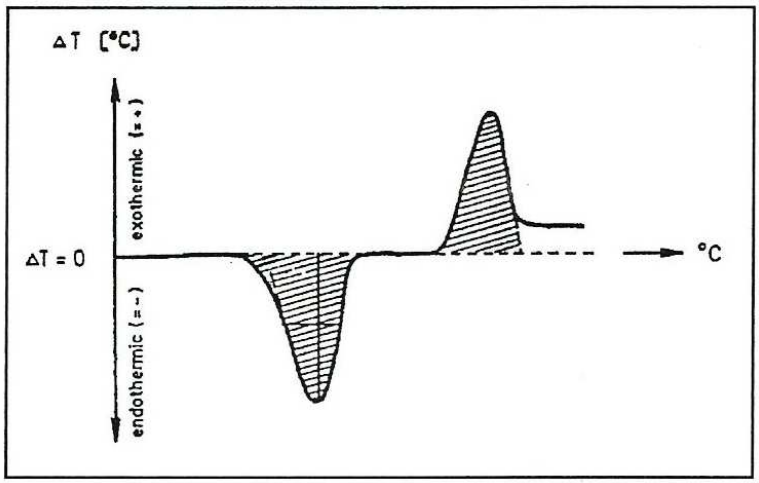

Figure AIII.3. Example of a DTA analysis.

For a given thermal gradient, a peak will be much more wide as much as the reaction is slow. On the contrary the intensity of the peak will be higher as much as the thermal gradient is great (i.e. high heating rate).

The position of the peaks provides information on the type of components present in the sample because every substance has its own characteristic reaction temperatures.

The area under the peak is proportional to the energy absorbed or developed by the reaction and reveals basically the amount of the components reagents.

Through DTA analysis is possible to determine the temperatures at which some reactions occur such as the dehydration/calcination and the amorphization and/or recrystallization, and then the thermal stability of a material.

Despite the fact that the thermal analyses are simple and immediate, they do not allow to obtain information about the structural changes induced by temperature and for this reason are often coupled to X-ray diffraction measurements.

As already mentioned in the aims, the dye molecules involved in this study are complex organic molecules that can have different decomposition features once encapsulated into the zeolites- due to their interaction with the framework- respect to the pure dye compounds. Moreover, it is important to distinguish between the dye molecule encapsulated within the zeolite porosities from that only physisorbed on the surface of the zeolite. For these reasons to

not have an unambiguous identification of the species responsible of the weight loss, in this work thermal analysis(TGA) has been combine with a Evolved gas mass spectrometry (MS EGA). This technique will be explain in the following paragraph.

AIII-I TGA-MS EGA

Evolved gas analysis (EGA) is the real-time analysis of the gas products released during TGA by a sample. This technique allows the passage of the evolved gas in a mass spectrometer (MS) through a specialized interface and heated transfer line (Fig. AIII-I.1).

When several compounds are evolved, the MS can track their evolution profiles and this is possible because mass spectra are substance-specific. The spectra can be used to characterize the substance or substance class through spectral interpretation and comparison with database reference spectra. Decomposition pathways can thereby be explain.

In general MS characterizes substances by identifying and measuring the intensity of molecular fragment ions of different mass-to-charge ratio (m/z).

The incoming gas molecules are first ionized in the ion source. The positive molecular ion and fragment ions formed are then separated according to their m/z value by a combination of magnetic and electrostatic fields.

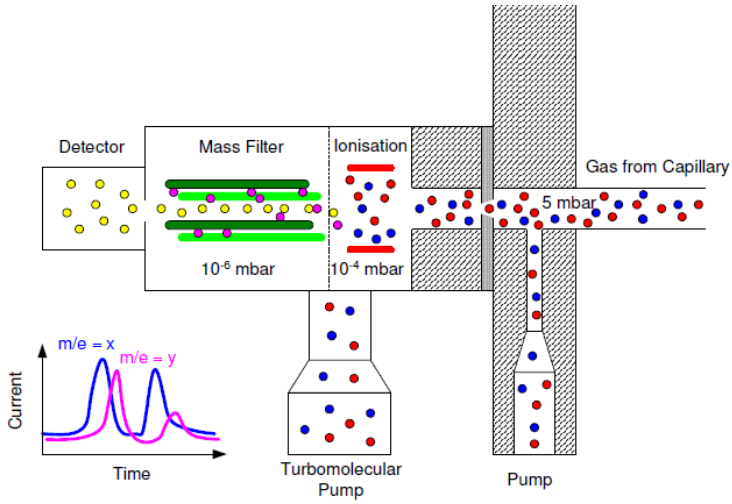

Figure AIII-I.1. General instrument set up of a TGA-MS-EGA.

APPENDIX IV. FT-IR SPECTROSCOPY -ATTENUATED TOTAL REFLECTANCE (ATR)

Infrared (IR) spectroscopy is an extremely reliable and well recognized fingerprinting method, to characterized and identified many substances.

One of the strengths of IR spectroscopy is its ability to obtain spectra from a very wide range of solids, liquids and gases. Traditionally IR spectrometers have been used to analyze solids, liquids and gases by means of transmitting the infrared radiation directly through the sample. Where the sample is in a liquid or solid form the intensity of the spectral features is determined by the thickness of the sample and typically this sample thickness cannot be more than a few tens of microns in order to allow a significant fraction of the light to be transmitted.

The technique of Attenuated Total Reflectance (ATR) (Figure AIV.1) has in recent years revolutionized solid and liquid sample analyses because it combats the most challenging aspects of infrared analyses, namely sample preparation.

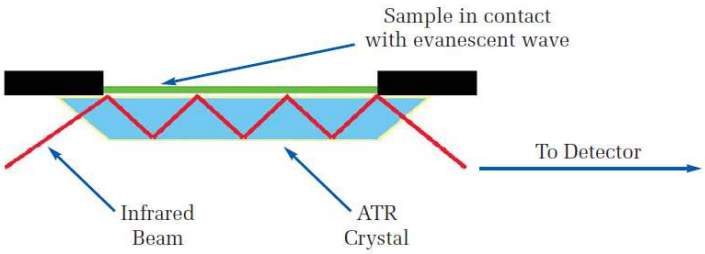

Figure AIV-1. Principles of ATR-IR.

An attenuated total reflection accessory operates by measuring the changes that occur in a totally internally reflected infrared beam when the beam comes into contact with a sample (Fig. AIV-1). An infrared beam is directed onto an optically dense crystal with a high refractive index at a certain angle. This internal reflectance creates an evanescent wave that extends beyond the surface of the crystal into the sample held in contact with the crystal. This evanescent wave protrudes only a few microns (0.5 μ - 5 μ) beyond the crystal surface and into the sample. Consequently, it is important that there is a good contact between the sample and the crystal surface. In regions of the infrared spectrum where the sample absorbs energy, the evanescent wave will be attenuated or altered. The attenuated energy from each evanescent wave is passed back to the IR beam, which then exits the opposite end of the

crystal and is passed to the detector in the IR spectrometer. The system then generates an infrared spectrum. For the technique to be successful, the following two requirements must be met:

i) the sample must be in direct contact with the ATR crystal, because of the evanescent wave;

ii) the refractive index of the crystal must be significantly greater than that of the sample in order to allow the internal reflectance to occur: if this requirement is not fulfilled the light will be transmitted rather than internally reflected in the crystal. Typically, ATR crystals can be of Zinc Selenide (ZnSe), Germanium or Diamond.

APPENDIX V. COMPUTATIONAL METHOD

Chemical events occurring in zeolite frameworks are strictly governed by a complex balance of guest-guest and host-guest interactions and are generally referred to as *intracage chemistry.* Modeling studies have become an extremely versatile and useful tool to study the complexity of zeolite chemistry and understanding the correlation between the macroscopic properties of the system and its behavior at the atomistic level. Moreover computer simulations may allow to clarify the interpretation of experimental result therefore integrated theoretical-experimental approaches are currently adopted to rationalize the chemical-physical properties of complex systems like zeolites.

A brief introduction of the general concepts on the simulation methods is provided in the next paragraph. [1]

AV-I Simulation techniques

Molecular simulation techniques adopted in the study of zeolites may be broadly classified in two main categories. The first group consists of approaches in which the electronic structure of the system is explicitly described in quantum mechanical terms, defined *first principles method.*

In general, a first principles calculation has as its main target, via the approximate solution of the time independent Schrödinger equation, the electronic structure that contains the information about the state of the given system. The Density-functional theory (DFT) based approach, which belongs to this first group, can be considered as the method of choice for studying zeolite chemical and structural properties. Such an approach is also widely adopted in studying zeolite based catalytic processes, due to its ability in describing breaking and formation of chemical bonds.

The second group of computational techniques is based on classical statistical mechanics and does not explicitly model the electronic structure of the system. Interatomic interactions are here described by effective potentials, which may be parameterized either from experimental or *ab initio* data. Among these methods, the most used for zeolite systems are the Monte Carlo (MC) and the Molecular Dynamics (MD) approaches [2-5]. At difference from first-principles approaches, the use of empirical potentials prevents classical MC and MD to simulate chemical reactions. However the lower computational cost of both methods, and the

possibility to easily deal with periodic systems allow for simulations including a much larger number of atoms than in the DFT approach. Therefore it is possible to model zeolites characterized by large unit cells and dynamic processes involving thousands of atoms such as adsorption and/or diffusion of extraframework species.

The choice of the computational technique is dictated by the specific problem under investigation. In fact while standard first principles are able to describe at a very high level of accuracy both structural and electronic properties of small zeolites, the classical approaches are most suitable when the interest is on the dynamical behavior of an a extended non reacting zeolite system. There are however cases where both methods are needed. These requirements can be satisfied by the first principles molecular dynamics approach introduced by Car and Parrinello in 1985 [6].

By using the Car-Parrinello (CP) approach it is possible to follow the time evolution of a system with first-principles level accuracy. The key feature of CP-MD method is the definition of a fictitious dynamical system in which the potential energy surface depends on both the nuclear and the electronic degrees of freedom. Therefore in the CP-MD method electrons are kept close to the ground state, preventing the need for a costly self-consistent iterative minimization at each time step.

Referenced cited

[1] Tabacchi G., Gamba A., Fois E., V. A. (2009), Basiuk and P. Ugliengo (Editors) pp. 65-87, American Scientific Publishers, USA

[2] Allen M. and Tildesley D. (1987), Claredon Press

[3] Frenkel D. and Smit B. (1996), Academic Press, San Diego

[4] Smit B. and Krishna R. (2001), Curr, Op. Solid State Mat. Sci. 5, 455-461

[5] Demontis P. and Suffritti B. G. (1997) *Chem. Rev.*, 97, 2845-2878

[6] Car, R.,Parrinello, M. (1985) *Phys. Rev. Lett.*, 55, 2471-2474

[7] (Perdew, J. P.; Burke, K.; Ernzerhof, M. (1996) *Phys. Rev. Lett*., 77, 3865-3868.

[8] Grimme, S. (2006) *J. Comput. Chem.*, 27, 1787-1799.

[9] Vanderbilt, D. (1990) *Phys. Rev. B*, 41, 7892-7895.

[10] Kleinman, L., Bylander, D.M. (1982) *Phys. Rev. Lett.*, 48, 1425-1428.

[11] Hamman, D. R., Schlüter, M., Chiang, C. *(*1979) *Phys. Rev. Lett.*, 43, 1494−1497.

[12] Troullier N., Martins, J. L. (1991) *Phys. Rev. B*, 43, 1993-2006

APPENDIX VI. UV/Vis SPECTROSCOPY: ABSORPTION AND EMISSION (FLUORESCENCE)

Important information on the functionality of these dye-zeolite systems are given by spectroscopic studies. In particular UV/vis absorption end emission (fluorescence) spectroscopies are two complementary techniques mainly used for investigate the efficiency of the energy transfer between the dye molecules hosted in the zeolite [1]. In the following the theory of these two techniques will be briefly explained.

AVI-I. UV/Vis Absorption spectroscopy

In general, when a molecule absorbs an incident photon of appropriate energy, the photon energy causes the transition from the ground state to an electronic excited state. This type of interaction is sensitive to the internal structure of the molecule, since the laws of quantum mechanics only allow the existence of a limited number of electronic excited states of any given chemical species. Each of these excited states has a defined energy and then molecules can therefore be identified by their absorption spectra. Their wavelength-dependent capacity for absorbing photons depends on the separation in energy of the electronic states. From the excited states, the molecule can relax to the electronic ground state by transforming the excess energy into vibrations of the nuclei or by transferring it through a non radiative mechanism to the molecule's surroundings, but it can of course also simply re-emit a photon.

The cornerstone of the absorption spectroscopy theory is the Beer-Lambert law (Fig. AVI-I.1). It states that: i) the proportion of light absorbed by a material is independent on the intensity of the incident radiation [2,3] and ii) that the absorption is proportional to the concentration of the sample.

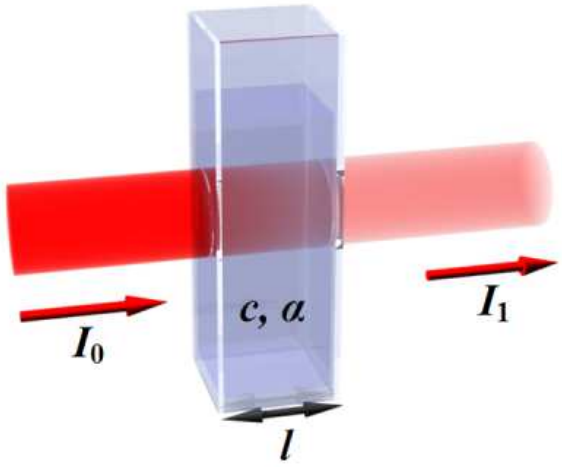

Figure AVI-I.1. Light transmission phenomenon.

The combination of these two states gives the expression:

$$A=\alpha*C*l$$

where **A** is the absorbance, α is the molar absorption coefficient, **C** is the concentration and **l** is the path length. The absorbance is measured experimentally and is given by:

$$A=\log I_0/ I_t$$

where $\mathbf{I_o}$ is the intensity of the incident light and $\mathbf{I_t}$ is the intensity of the light transmitted through the sample.

Figure AVI-I.2 shows the typical set up of a spectrophotometer working in transmission. It is composed by:

Light sources: a tungsten filament in the 320-2500 nm range (near infrared, NIR, and visible light) and arc (H_2 or vapors Hg) in the 190-340nm range (UV)

Monocromathors: Prisms (BEF2 or LiF UV quartz for the near UV, Vis glass.); lattices.

Detector: photocells or photomultipliers (accuracy of the intensity measures ± 0.2%)

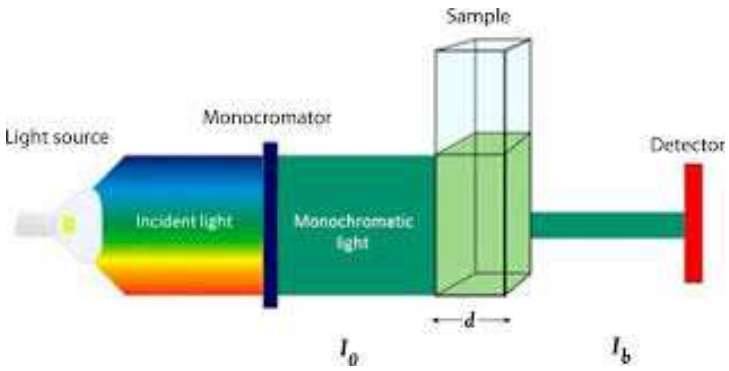

Figure AVI-I.2. General set up of a UV-Vis spectrophotometer in transmission mode.

However, the percentage of UV-Vis light transmitted through a powder is in general so low, to not allow to use this configuration to record the spectra. In case of solid powder samples, the most used is the diffuse reflectance UV-vis technique. This technique is highly sensitive, with a broad sample applicability and refers to the part of the incident beam reflected in all directions by the sample. In fact the reflected beam can be divided in (Fig. AVI-I.3):

i) Specular reflection: the radiation can be reflected off the top surface of the particle at an angle of reflection equal to the angle of incidence without penetrating into the particle. This part of the radiation is not informative and its contribution has to being minimize in order that the experimental conditions fulfill the hypotheses at the basis of the Kubelka-Munk equation (see below).

ii) Diffuse reflection: the incident radiation penetrate into one or more sample particles and subsequent scatter from the sample matrix. The resulting radiation may emerge at any angle relative to the incident radiation and since it has traveled through the particulates it now contains information about the absorption characteristics of the sample material.

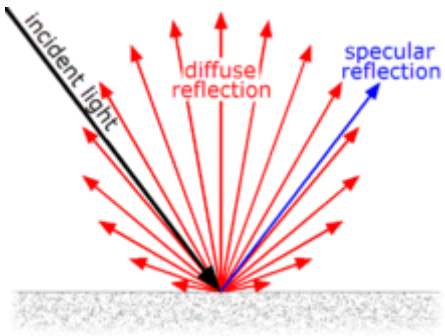

Figure AVI-I.3. Diffuse and specular reflection.

The diffuse reflectance is described by the theoretical model developed by Kubelka and Munk [4] This model takes into account both the contributions of absorption and diffusion (scattering) of the light. While the equation of Lambert-Beer considers only the absorption, the theory of Kubelka-Munk includes both the absorption and the diffusion contribute. The Kubelka-Munk equation is generally expressed as:

$$fKM(R_\infty) = [(1 - R_\infty)^2/2R_\infty] = k/s$$

where R_∞ is the absolute reflectance of the layer, *k* is the molar absorption coefficient, and *s* is the scattering coefficient.

AVI-II Fluorescence spectroscopy

The luminescence is a physical phenomenon typical of some materials, solid or liquid, which have the property of emitting light in response to absorption of energy. Molecules able to produce luminescence are called fluorophores.

The best-known form of luminescence is the photoluminescence (PL): emission of photons resulting in the exposure of the material to radiation. After the absorption of energy the molecule passes in the excited state and its relaxation leads to the photons emission, i.e fluorescence [5].

At room temperature it is supposed, therefore, that most of all molecules are in the lower electronic level; defined ground state.

A molecule, which is located in the ground state, has all the orbital occupied by two electrons with spin paired. When the molecule is in its excited state, there will be a promotion of an electron from an occupied orbital to an unoccupied orbital with a higher energy. In this configuration the two electrons, previously paired, are located in two different molecular orbitals and therefore the relationship between their spin is no longer governed by the Pauli exclusion principle: the electron in the higher molecular energy can have spin + ½ or - ½ regardless of the spin of the other electron. If the two electrons divided, in the excited state configuration, continue to have the spin paired, the molecule will be in an excited state called singlet (S_n). If, instead, an electron reverses its spin, the two electrons have the same spin, the molecule will be in the triplet excited state (T_n).(Figure AVI-II.1)

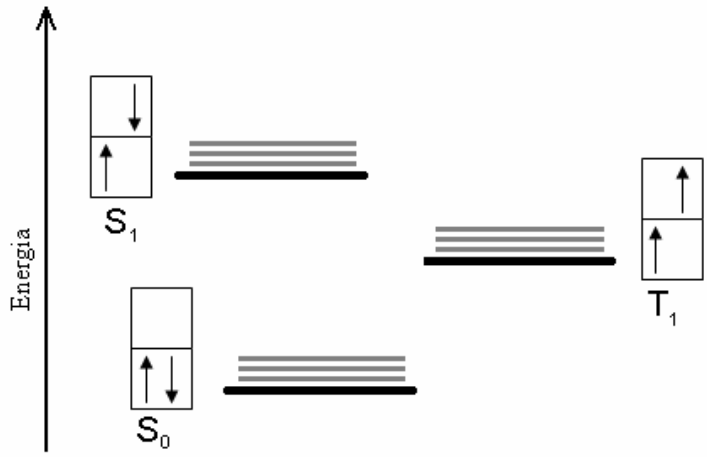

Figure AVI-II.1 Simplified representation of the electronic states

As one can see in Figure AVI-II.1, the triplet state will always have lower energies compared to the corresponding singlet state, as in the singlet state the two electrons have a finite probability of occupying the same region of space, while in the states of triplet this probability is zero. This implies that the Columbian repulsion energy in the triplet electronic state is smaller.

A molecule that is located in the excited state can return to the ground state through radiative processes (luminescence, or decay in quantized form) or with non-radiative processes (heat, i.e. decay in shape not quantized).

The radiative processes are also divided into two classes: fluorescence and phosphorescence. This division depends on the electronic nature of the excited state from which derive the emission.

The radiative and non-radiative processes are shown in the Jabłoński diagram [6], schematically shown in Figure AVI-II.2, where the solid lines indicate absorption or emission of light, wavy lines represent the non-radiative processes. The radiative relaxation is always in competition with the non-radiative processes.

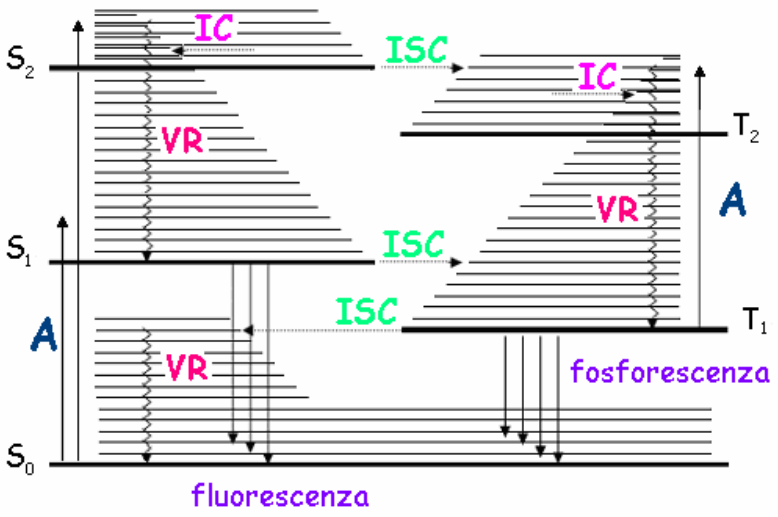

Figure AVI-II.2. Jabłoński diagram.

In the non radiative decays, the electronic energy is converted into other forms of internal energy, typically vibrational energy. This partial conversion allows to populate the isoenergetic vibrational levels of an electronic state of lower energy. If the decay occurs between states with the same multiplicity it is named *internal conversion* (IC, transition from S_2 to S_1 or S_1 to S_0). On the contrary if the decay leads to a switching between states with different multiplicity is denoted as *intersystem crossing* (ISC transition from S_1 to T_1, but also from T_1 to S_0). Furthermore, because of the intermolecular collisions, the molecules may have a vibrational relaxation (VR), which brings the system to lose vibrational energy, with consequent population of the lowest vibrational level within the same electronic state of the molecule.

Not all the electronic excited states generate emissions sufficiently intense to be observed. This happens because the emission from one electronic state (S_2) higher than the first excited electronic level (S_1) is permitted, but to be appreciable, it should be much faster than it is. Generally, a molecule which is in an excited state higher than the first, passes through the *internal conversion* to a isoenergetic vibrational level of the lower electronic state and subsequently by vibrational relaxation passes to the lower vibrational level. Practically, all the excited molecules fall quickly on the lowest vibrational level of the first electronic excited state[7].

From the fundamental vibrational level of the electronic excited state S1, the molecule can

return to any of the vibrational levels of the fundamental electronic state through fluorescence emission. Therefore, fluorescence emission is defined as the light that comes from the transition of a electron from an excited level to a ground state level, maintaining the spin, characterized by transitions from the level S_1 to S_0. [8]

During the study of fluorophores an important parameters that have to be evaluated is the quantum yield (Φ_F).

The quantum yield of fluorescence F may be written:

$$\phi_F = \frac{\text{Number of photons emitted}}{\text{Number of photons absorbed}}$$

The fluorescence quantum yield can also be expressed with the following equation, which takes into account all the processes in which the excited state of singlet may be involved or rather, the ratio of the radiative rate over the sum of the radiative and the non-radiative rate

$$\phi_F = \frac{k_r}{k_r + k_{nr} + k_{isc} + k_c}$$

where k_r is the radiative rate constant, k_{nr} is the non-radiative rate constant, k_{isc} is the rate constant for intersystem crossing, and k_c is the rate constant for chemical reaction.

Molecules with high radiative rates will therefore tend to be better emitters. This is the case of many laser dyes, which are also good fluorescent probes.

References

[1] Calzaferri, G., Devaux, A., Ramamurthy, V., Inoue, Y., (2011); John Wiley & Sons (Editors): New York,; Chapter 9, 285−387

[2] Beer L., Claude Jombert, Paris (1729)

[3] Ingle J. D. J. and Crouch S. R., Prentice Hall, New Jersey (1988)

[4] Kubelka P. and Munk F. Z. (1931) *Tech. Phys*., 12, 593-601

[5] Köhler, A., Wilson, J. S., Friend, R. H. (2002) *Adv. Mater*., 14, 701-707

[6] Elumalai, P., Atkins, P., de Paula, J. Atkins' Physical Chemistry, Oxford University Press: Oxford (2002)

[7] Lakowicz, J. R. KA/PP: New York, (1999)

[8] Evans R. C., Douglas, P., Winscom, C. J. (2006) *Coord. Chem. Rev*., 250, 2093-2126